isec Engenharia

MESTRADO EM ENGENHARIA MECÂNICA

Finite element analysis of femoral components after in-cement revision

Autor

Maria Helena Moure de Magalhães Barbosa

Orientador

Doutor Luis Manuel Ferreira Roseiro

Coimbra, janeiro de 2022

INSTITUTO POLITÉCNICO DE COIMBRA

INSTITUTO SUPERIOR

DEPARTAMENTO DE ENGENHARIA MECÂNICA

Finite element analysis of femoral components after in-cement revision

Dissertação para a obtenção do grau de Mestre em Engenharia Mecânica

Autor

Maria Helena Moure de Magalhães Barbosa

Orientador

Doutor Luis Manuel Ferreira Roseiro

Coimbra, janeiro de 2022

INSTITUTO POLITÉCNICO DE COIMBRA

INSTITUTO SUPERIOR

RESUMO

A técnica de cimento-em-cimento é um procedimento de revisão da artroplastia total da anca em que uma nova prótese é aplicada numa manta de “cimento velho” bem fixa ao do fémur. Excelentes resultados têm sido reportados em diversos estudos clínicos a respeito da estabilidade dos componentes femorais após alguns anos da cirurgia. Contudo, poucos estudos biomecânicos têm sido apresentados, envolvendo a utilização desta técnica. Assim, este trabalho pretende contribuir para a compreensão da análise mecânica, nomeadamente avaliar a distribuição de tensões e a estabilidade de longo prazo das estruturas deste tipo de implantes, colocados com recurso à técnica de cimento-em-cimento. O estudo numérico implementado recorre ao método dos elementos finitos, num total de seis modelos que simulam várias condições de revisão a partir desta técnica. Dois modelos de artroplastia primária, com próteses do tipo *force-closed* de diferentes dimensões, foram desenvolvidos de modo a servir de base para a criação dos modelos representativos da cirurgia de revisão. O recurso a um método de validação qualitativa permitiu comparar os resultados obtidos com os presentes na literatura. O trabalho centra-se no estudo da influência das variações nas espessuras de cimento, e da prática da substituição da haste femoral por outra de menores dimensões. Assim, apesar de possuírem hastes de mesmo tamanho, todos os modelos da cirurgia de revisão são diferentes entre si, e comparam, simultaneamente, a espessura de cimento novo ao redor da haste e as dimensões do cimento velho. Duas análises estáticas foram executadas para cada modelo, uma considerando a interface entre cimento e haste perfeitamente fixa e outra, modelando o contato com descolamentos de interface, de modo a simular o afundamento da haste. Os resultados obtidos mostraram que a influência da espessura de cimento e da mudança de uma haste por outra de menor tamanho na distribuição de tensões pode ser considerada desprezável. Na avaliação da estabilidade, o estudo evidenciou maior estabilidade no cimento velho.

Palavras-Chave: Artroplastia Total da Anca; Cirurgia de Revisão; Cimento-em-cimento; Elementos Finitos.

ABSTRACT

The in-cement technique is a procedure in which a new stem is cemented into a well-fixed cement mantle inside the femur bone, during revision total hip arthroplasty. Excellent outcomes have been reported in several clinical studies regarding the stability of the femoral components, after revision total hip arthroplasty using the in-cement technique. Aiming to evaluate the stress distributions and the long-term stability in such implants' structures, the finite element method was employed in static simulations on a total of six models that were designed to represent implanted femurs postoperatively. The influence of the variations in the mantle thick-nesses in the revision models, and of the practice of replacing the femoral stem by another with shorter size on the biomechanical results was also considered in the present investigation. Therefore, all revision models were designed to have stems of same size but to differ from each other when comparing, simultaneously, the new mantle thickness around the stem and the dimensions of the well-fixed mantle. Two primary hip replacement models, with force-closed stems of different body sizes, were designed to serve as a basis to create the revision models, where one of them was used verify the validity of the models created in this work, through a qualitative comparison between the results from the static studies with the ones from a previous publication. Also, the bonded and debonded classic interfacial interactions were considered for the cement-stem interface in all models, where the debonded stem resulted in the increase of the tensile and compressive stress levels across the implant components. The differences in the mantle thicknesses and the change of the femoral stem by another with smaller dimensions were found to exert negligible effects on the stress distributions. In the stability analysis, it was concluded that the well-fixed mantles are the stablest.

Keywords: total hip arthroplasty, revision surgery, in-cement technique, finite element method.

Index

LIST OF FIGURES

LIST OF TABLES

SYMBOLOGY, ACRONYMS AND ABBREVIATIONS

Symbology

P_f	Probability of failure
P_s	Probability of survival
σ	Tensile stress level

Acronyms

ASTM	American Society for Testing and Materials
ISO	International Organization for Standardization

Abbreviations

PMMA	Poly (methyl methacrylate)
THA	Total hip arthroplasty
THR	Total hip replacement

1. INTRODUCTION

The total hip replacement (THR) or total hip arthroplasty (THA) is considered to be one of the most successful orthopedic interventions of its generation (Callaghan et al., 2000). For instance, the calculated mean percentage of implant survival within ten years, from 2009 to 2019, published in the 2019 Swedish National Hip Arthroplasty Register was 95% and, in the period 2017-2019, the registered number of primary hip arthroplasties was 18827.

The first recorded attempt of a hip replacement is dated by the end of the 19th century when Glück employed a technique to replace with ivory the femoral head of a patient, facing complications caused by the deterioration of the hip joint due to tuberculosis (Knight et al., 2011). In 1923, Smith-Petersen introduced the mold arthroplasty where an interpositional cup was placed over the femoral head to provide a smoother surface for the movement of the joint (Knight et al., 2011). In 1938, Philipe Wiles developed the concept of total hip replacement (Callaghan et al., 2007). In the early 1960s, Sir John Charnley designed the low friction arthroplasty, a technique which uses implants with essentially the same design philosophy of today's THR prostheses, with a prosthetic set formed by a metallic femoral stem, a polyethylene acetabular component, and acrylic bone cement used in dentistry, to cement the prosthesis into the femur (Knight et al., 2011).

Today, hip replacement prosthetic components can be implanted through cemented or cementless techniques. In the cementless implantation, the definitive implant fixation to the bone is expected to be achieved with the bone growth to the porosities of the components, while the cemented implants use the interposition of PMMA between bone and implant (Galia et al., 2017). The techniques employed for the cement preparation and implant fixation of the cemented femoral components in THR have been under modifications through the years, and the stages of evolution of the cementing techniques can be divided into four generations. In the first generation, no distal femoral cement restrictor was placed during the femoral canal preparation, the bone cements were manually mixed and manually inserted into the femoral canal to be later pressurized with the surgeon's finger (Galia et al., 2017). In the second generation, the cement restrictors were included in the implant construct and the cement insertion started to be done with a pistol to fill the femoral canal (Rice et al., 1998). In the third generation, new cement mixing methods started to be used such as vacuum mixing and centrifugation (Barrack et al., 1992). The fourth generation of cementation techniques is marked by the addition of a proximal centralizer (Vaishya et al., 2013).

Despite the excellent implant survival rates, at times patients undergo revision hip arthroplasty where all or some of the prosthetic components are changed. For instance, in the three-year interval of 2017-2019, the number of registered first-time revisions published in the Swedish National Hip Arthroplasty Register was 4247, while the number of second-time revisions fluctuated between 753 and 919. Among the most common causes for revision surgeries are, periprosthetic fracture (fracture around the stem), infection, aseptic loosening (loosening that is not caused by infection), and dislocation (Galia et al., 2017). In Swedish National Hip Arthroplasty Register, since 1999, in more than half of the revisions, the stem has been changed, where the cemented fixation has dominated among the first-time revisions, while for the multiple revisions this type of fixation was opted in 43,6% of the cases, between 2017 and 2019.

The revision of the cemented femoral components often involves the removal of the stem with the complete extraction of the cement mantle, followed by the insertion of a cemented or uncemented implant. However, sometimes, the in-cement or cement-in-cement technique is employed, where the femoral stem is removed from the well-fixed mantle to posteriorly a new implant be cemented into the older mantle (Cnudde et al., 2017). Lieberman et al. (1993), have advised that, after X-ray image inspection, at least the distal two thirds of the cement bone interface should appear well maintained to safely perform this technique, and indicated it for cases when there is a broken stem with intact distal cement mantle, when femoral component is extracted for revision of the loose cup to improve acetabular exposure and/or increase offset, *for recurrent dislocation resultant of component malposition,* and at the occurrence of debonding of the stem within an intact cement mantle. This procedure reduces the complications related to the removal of the well-fixed cement such as the risks of cortical perforation and femoral fracture and has a reduced operative time (Cnudde et al., 2017). It can be observed a fairly significant proportion of in-cement surgeries, among the cemented revisions that involve the replacement of the femoral stem. In Cnudde et al. (2017) this proportion is reported to be around 15,9% of all the registered cemented revisions from the Swedish National Hip Arthroplasty Register, and to be approximately equal to 33,3% of all the cemented revisions that used the Exeter or Lubinus stem types.

Additionally, the in-cement technique has demonstrated highly satisfactory outcomes regarding femoral stem fixation. Duncan et al. (2009) followed up for a mean of eight years 136 revision surgeries, in patients with a mean age of 70,9 years, using the in-cement technique, where among this group a second revision was required for 25,7% of the hips, being the acetabular loosening the main contributor for re-revision (19,1%), while there was only one case of a second operation motivated by femoral fracture, and another one motivated by stem fracture. More recently, Cnudde et al. (2017) examined the outcomes of 1179 in-cement stem revisions that made use of Exeter and Lubinus stems, where it was determined that the survival of the implant up to six years, until the need for re-revision of the stem, was high for both groups (94% for Exeter, and 95% for Lubinus).

Although there is a fair number of clinical analyses involving the study of the in-cement revision follow-ups of several patients to determine the most common complications and reasons for re-revision, no published biomechanical analysis, regarding the effects of the in vivo loading on the long-term and stabilities of the femoral implants, after the in-cement revision, were found by the author.

Therefore, as an attempt to provide a contribution for the understanding of the biomechanical response of such revised femoral implants, models of the femoral elements from in-cement revision with force-closed stems were created for a series of linear static simulations that employed the finite element method, aiming to provide the data for the evaluation of the stress distributions in their components, and to estimate the long-term stability of those structures. The stability analysis was based on the probability of failure calculations used for the PMMA cement mantles within a certain number of loading cycles, following the method employed in Lennon and Prendergast (2001), and on the observation of the stress contours at the proximal region of the femur, to observe what would be the regions more susceptible to common complications that can compromise the long-term integrity of the implants, which are a result of stress shielding (e.g., bone loss, cortical bone thinning, joint prosthesis failure). As well, an evaluation was carried out of what could be the biomechanical motivation for the practice, reported in Sandiford et al. (2017), of the change of force-closed stems by others with shorter length, and of how much the variation in the thickness of the mantles from the revision models can influence the chances of failure. For this matter a comparative analysis was conducted between two groups of revised femoral implants created for this work, one where the primary stem would have been replaced by the same stem type but with shorter length, and the other in which a stem of the same body size would replace the primary component. Likewise, the models from each revision group were designed with different thickness of the new cement around the stem, to verify how much the variation in this geometric characteristic would affect their stress plots. Each of these two groups had their designs originated from primary hip arthroplasty models. Hence, the evaluations of the contour of stresses and long-term stability were also applied for all of their model configurations.

All the static simulations were done in SolidWorks® using parabolic tetrahedral solid elements to discretize the models, and considered the most critical load condition during gait on an implanted femur of an individual that would have gone through total hip replacement. Moreover, for every one of the THR models two cases of stem fixation were evaluated, one with a debonded cement-stem interface and other where it is totally bonded.

In the chapters 2, 3 and 4 in the present dissertation, are comprised the literature review that had to be conducted for the creation of the THR models, which are about the surgical procedures involved in the femoral stem implantation in total hip arthroplasty, the material properties and biomechanical role of the implant structure formed by prosthetic components and femur bone.

In chapter two, the main anatomical constituents of the hip joint and the prosthetic components of primary hip replacement are presented, the most common materials employed in total hip arthroplasty components are introduced, and the surgical steps of a typical cemented stem implantation is described.

In the third chapter, the anatomy of the femur bone is addressed, where some of the aspects about the femoral structure, regarding its skeletal anatomy, material properties of the bony tissues, and points of muscular attachments are introduced.

Chapter four is initiated with a brief history of the use of the PMMA in total hip arthroplasty, followed by a succinct explanation of its chemical constituents and curing process. Still in this chapter, the static properties, measured according to ISO 5833:2002, are presented along with the discussions about the biomechanical role of this material in the implant construct. Then, in chapter five, it is introduced a discussion about the main characteristics of shaped-closed and force-closed stems regarding their design philosophies for fixation into the cement, and transmission of load.

In chapter six, are detailed the steps of the development of the THR designs used in the finite element analyses, that correspond to the description of the geometries included in the models and of the mesh elements which describe them, the definition of the material properties attributed to each of the components, the selection of the loading profile exerted in the proximal femur with the definition of the points of application of the hip contact and muscular forces, and the description of the types of interfacial contact configurations and of the constraints used for the models' stabilization that were implemented in all static studies.

Before the study of the contour of stresses and the estimations of long term-stability got initiated, a comparative study was employed to ensure the validity of the results obtained from the THR models which is detailed in chapter seven.

Finally, in chapter eight, are presented the stress plots of the femoral components from the primary and revision models, where the influence of a series of design features regarding the geometries of the stem and mantles, as e well as the configuration of cement-stem contact is addressed. This chapter also contains the results used for the evaluation of the stress shielding in the cortical bone. In chapter 9, the polynomial equations used to determine the chances of fatigue failure of the PMMA cement, determined by Murphy and Prendergast (2000), are introduced and, based on these equations, the discussion of the long-term stability of all the THR models is also addressed.

At the end of the present text, are presented the conclusions related to the data obtained from the static studies and the statistical analysis regarding the probabilities of failure calculations of the femoral implants, alongside some suggestions of future works that could be conducted on the biomechanical analysis of the implant structures after the in-cement revision.

Chapter 2 - Generalities on total hip joint replacement surgery

The hip joint is a ball-and-socket type of joint where the femoral head is the ball and the acetabulum is the socket, where both are covered with articular cartilage that facilitates the relative movement at their interfaces (Foran and Fischer, 2020). The hip joint is enclosed in a fibrous capsule, and is internally lined by a synovial membrane, which produces a lubricant fluid for the articular cartilage, and reduces the friction when the joint moves (Ocran and Salvador, 2021). Figure 2.1 displays the articulation between the femoral head and the acetabulum surrounded by the joint's fibrous capsule. Being the most stable joint of the human body, this structure is responsible for the transmission of the upper body's weight to the lower limbs, and also allows movements in the three rotational degrees of freedom (Foran and Fischer, 2020). Among the possible movements are flexion, extension, abduction, adduction, external and internal rotation, which are schematically represented in figure 2.2.

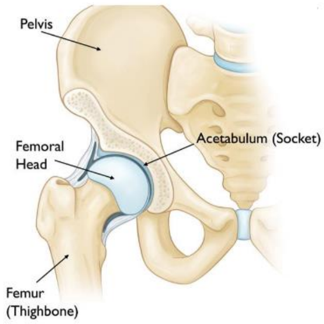

Figure 2.1– Schematic representation of the hip joint

(Foran and Fisher, 2020)

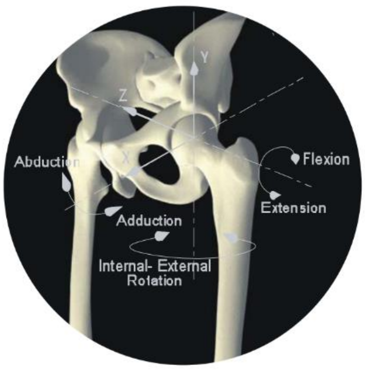

Figure 2.2 – Rotational degrees of freedom of the hip joint

(Buechel and Pappas, 2015)

At times, physiological complications of the hip joint, which can limit one person's capacity to perform everyday life activities, can only be clinically treated by means of the surgical procedure for the replacement of the damaged anatomical parts of the joint with prosthetic implants, the total hip replacement (Foran and Fischer, 2020). In this chapter, are going to be introduced the general aspects of how one patient's first hip replacement surgery can be conducted, with emphasis on the femoral component implantation, as well as the information about the most common materials used in the prosthetic components.

2.1-Surgical Procedure

When severe hip pain caused by complications or diseases (such as osteoarthritis, rheumatoid arthritis, post-traumatic arthritis, osteonecrosis, and childhood hip disease) can't be relieved by the use of anti-inflammatory drugs and physical therapy, primary hip replacement surgery becomes the best alternative to improve the patient's quality of life. Normally, this procedure consists of replacing the articular cartilage of the joint with a metal socket (the acetabular component) and replacing the femoral head with a ball prosthetic component, which is normally attached to the neck of a cemented or cementless femoral stem that is implanted into the femur bone. Almost all modern hip stems have modular heads, which means that they are connected to the femoral stems by a mechanical junction (Keppler McTighe, 2012). The socket is normally attached to the acetabulum with screws or cement and, between the socket and the prosthesis head, a spacer is introduced to provide a low friction gliding surface (Foran and Fischer, 2020). Figure 2.3, is an illustration of generic femoral and acetabular total hip replacement components, which also displays a hip joint structure after the surgical procedure. It is beyond the scope of this work to discuss details about the implantation of cementless stems because their fixation is done directly into the femur bone and dismisses bone cement.

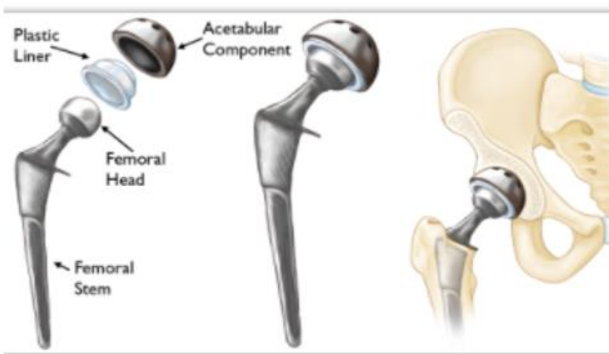

Figure 2.3 - Representation of generic acetabular and femoral implants of total hip replacement surgeries

(Foran and Fisher, 2020)

The surgical procedures for the implantation of cemented femoral stems generally comprise preoperative planning, femoral osteotomy, femoral canal preparation, and the process of stem fixation. In the preoperative planning, surgeons carry out analyses of X-ray images of the whole pelvis to decide what should be the most appropriate stem size and its optimal position in the medullary canal, as well as the correct position and sizes of the acetabular and other femoral components, such as the **distal centralizer and medullary plug**, to ensure the maintenance of equal leg lengths. Also in this phase, the determination of the most appropriate proximal and distal cement mantle thickness is done, based on the morphology of the femur bone. Figure 2.4 shows an example of a template used for the determination of the size and position of the femoral stem extracted from Sulzer Orthopedics (n.d), where the base green line is tangent of the both ischia, the upper line is drawn over the acetabula and the midline is defined between the lesser trochanters. The difference in the distance measured between the connecting line of the lesser trochanters and the baseline corresponds to the correction needed to obtain equal leg lengths.

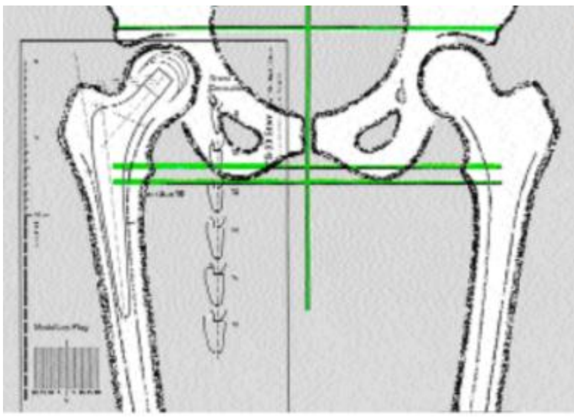

Figure 2.4 - Example of the preoperative planning template

(Sulzer Orthopedics, n.d)

The femoral osteotomy is the starting point of this surgical procedure. It is a process that involves the neck resection and subsequent femoral head removal, where the level of the cut is defined after the definition of the stem size in the preoperative planning, and the level of the lesser trochanter is used as a landmark. Figure 2.5 is an illustrative example of the use of an osteotomy guide for the neck cut, taken from a Smith and Nephew (n.d), which is used to determine the location above the level of the lesser trochanter (the scale represented on this device helps to address the position) where the neck cut should be done.

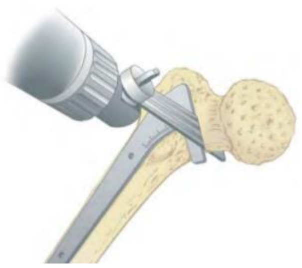

Figure 2.5 - The use of an osteotomy guide in the femoral neck cut

(Smith and Nephew, n.d)

After the removal of the femoral head, a series of steps are followed to ensure the femoral canal preparation for implantation. Figure 2.6 is an example of a sequence of operations executed for the opening of the femoral canal which shows, from the left to the right, the use of a box chisel, a blunt medullary reamer, and a trochanteric reamer, which are tools used to open the medullary canal in progressive steps, and of a stem shaped broach that is inserted after the initial opening steps are completed. The broach is designed to prepare the bone cavity and ensure an adequate cement thickness around the implanted stem.

Figure 2.6 - Sequence of femoral canal openning operations

(Smith and Nephew, n.d)

The following procedures involve the operation of stem fixation which is related to the bone surface preparation, the cement mixing technique, and the cement introduction followed by prosthetic implantation (McCaskie *et al*., 2000). The logic of the surface preparation is to remove materials that would remain at the cement-bone interface such as blood, marrow, and cancellous bone debris produced after reaming, using techniques like pressurized or pulsed lavage, and manual or power brushing. A clean and dry trabecular bone surface favors the cement penetration into the trabecular network to form a sound fixation, known as microinterlock (McCaskie *et al*., 2000). In Figure 2.7 are shown two steps of surface preparation: the hand brushing step used for the removal of blood clots, marrow fats, and weak cancellous debris (normally done after a lavage technique has had been deployed); and the insertion of the canal suction absorber, which is kept in the femoral canal while the cement is being mixed.

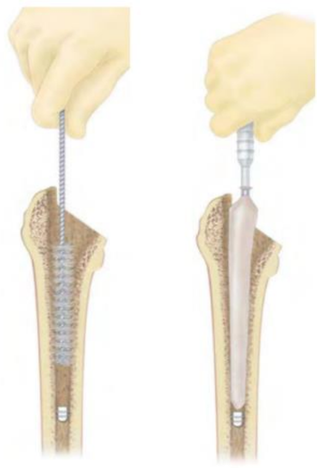

Figure 2.7 - Sequence of surface preparation steps

(Smith and Nephew, n.d)

Figure 2.8 is an illustration of the steps of a third generation cementing technique, which comprises the phases of cement mixing with a vacuum mixer, the cement insertion with a cement gun, followed by the use of a canal pressurizer to allow appropriate microinterlock between cement and cancellous bone, and the final step of stem insertion. A distal centralizer attached to the stem's tip and a cement restrictor placed below the cement mantle can also be observed in figure 2.8.

Figure 2.8 - Schematic representation of a third-generation cementing technique

(Smith and Nephew, n.d)

2.2- Employed Materials

Regarding the common materials currently used in the THR components, the femoral heads can be manufactured in both metal and ceramic (Merola et al.,2019). Different combinations of materials can be used for the bearing surfaces formed by the femoral head and the spacer contacting faces. The main types of bearings applied in THR are metal-on-polyethylene (MoP), metal-on-metal (MoM), ceramic-on-ceramic (CoC), and ceramic-on-polyethylene (CoP), and each type possesses different advantages and disadvantages regarding aspects such as implant cost, age and activity level of the patient, complications during surgery (Merola et al.,2019). Metal-on-Polyethylene surfaces are "safe, predictable and cost-effective" (Sandhu *et al*., 2005 cited by. Knight *et al.,2011*) but, polyethylene debris produced due to wear is a common responsible factor for periprosthetic osteolysis (Bizot *et al*., 2001 cited by. Knight *et al.,2011), and* for the increase in the rate of hip revision due aseptic loosening (Knight *et al*., 2011). Metal-on-metal surfaces have reduced friction and lower wear particles production which potentially increases their life-spans, but these bearings can produce metal ions that might hold carcinogenic risks, be linked to hypersensitivity reactions, and prosthetic loosening (Knight *et al*., 2011). Ceramic-on-ceramic bearing ensures lower friction and the particle debris is from an inert substance, and the high costs and the need for expert insertion are the most adverse aspects of its usage (Knight *et al*., 2011).

The femoral stems are normally metallic and, among the common biocompatible metals used in their manufacturing are titanium (Ti6Al4V), stainless steels and cobalt-chromium-molybdenum (CoCrMo) alloys. CoCrMo has high toughness, good corrosion resistance, high hardness, and wear resistance than the other metals, but low chemical inertness (Merola et al.,2019). Stainless Steels have approximately the same value of elasticity modulus as the CoCrMo alloys although they have lower strengths and ductilities (Merola et al.,2019). Ti-6Al-4V has also good corrosion resistance, but a closer stiffness value to cortical bone and bone cement than the other alloys (its value of the modulus of elasticity is approximately half of the value of the other alloys). Relatively to cemented implants, it has been debated that titanium stems had shown a higher tendency to fail before similar designs using CoCrMo or stainless steels, being one of the possible reasons the titanium lower stiffness which increases the flexibility of these stems in the cement mantle, which facilitates the debonding of the cement-stem interface and/or mantle cracking. But, along with the increased flexibility, there is an increased stress distribution in the proximal femur, which improves the prevention of the negative consequences of the stress shielding in this femoral region. Lower stress shielding, over the proximal femur, and higher incidence of cement damage is observed in implants with stems of lower stiffness (Gross, 2001, cited by, Ait Moussa, 2017). Therefore, it is argued that to prevent cement failure it is important to avoid titanium stem designs with small proximal dimensions.

Chapter 3 - Skeletal and muscular anatomies of the femur bone

Located in the lower limb, the femur bone (or long bone) is the largest bone of the human body and its anatomic constituents can be broadly divided into proximal femoral region, femoral shaft, and distal femur. It is in the proximal femoral region where the femoral head, neck, and apophysis are located. The femoral head forms the articulation with the acetabulum to form the hip joint, while the neck links the head to the femoral shaft. The apophyses are two bone protrusions, the lateral and larger one is called the greater trochanter, while the medial one is called the lesser trochanter. The apophyses are connected by the intertrochanteric line anteriorly, and by the trochanteric crest at the posterior side. At the distal femur, are present the medial and lateral condyles, which articulate with the tibia and patella to form the knee joint, the medial and lateral epicondyles, which are elevations of the non-articular areas of the condyles, and the intercondylar fossa or intercondylar notch. Between the proximal and distal femoral aspects, there is the femoral shaft, where is found the linea aspera, which is described as roughened ridges of bone. At the more proximal regions of the shaft, the lateral border of the linea aspera forms the gluteal tuberosity, while the medial border forms the pectineal line. Distally, the linea aspera forms the lateral and medial supracondylar lines, and between these structures is found the popliteal fossa. Figure 3.1 is a representation of the proximal resection of the right femur, where in the left is the posterior view, and in the right is the anterior view. In Figure 3.2 a schematic representation of the distal constituents of the same bone, where the anterior view is shown on the left, while the posterior view is in the right. Figure 3.3 is the posterior view of the anatomical elements of the femoral shaft.

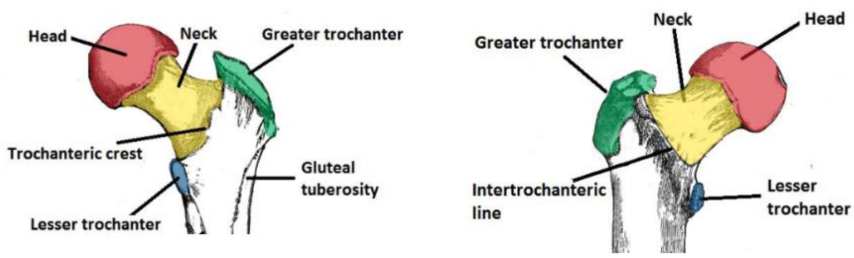

Figure 3.1- Proximal femoral anatomy

(https://teachmeanatomy.info/lower-limb/bones/femur/)

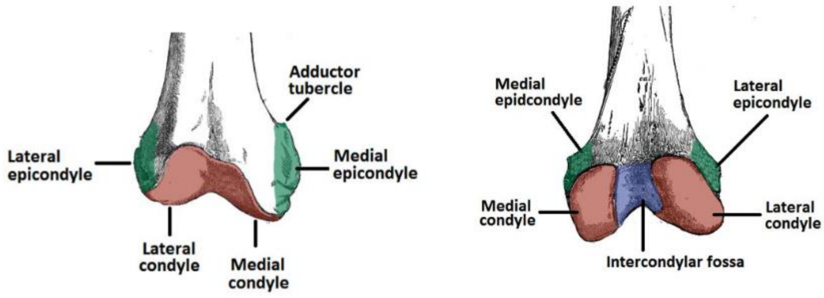

Figure 3.2 - Distal Femoral anatomy

(https://teachmeanatomy.info/lower-limb/bones/femur/)

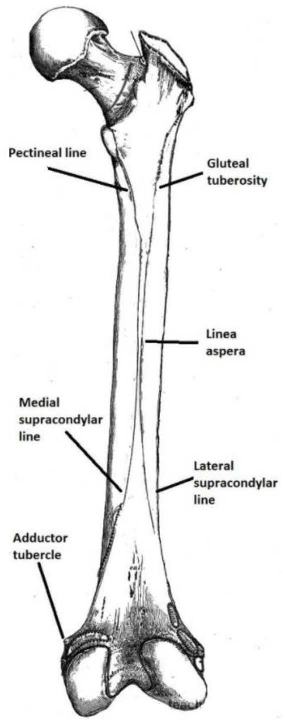

Figure 3.3 - Anatomical elements of the right femoral shaft

(https://teachmeanatomy.info/lower-limb/bones/femur/)

The long bone is formed by two bony tissues, the cortical and trabecular bone, which are arranged in two well-defined regions. The compact, or cortical bone, has a high density and forms a layer of variable thickness at the exterior side of the femur. The spongy or trabecular bone has a porous structure, filled with red marrow, which is more fragile than the cortical bone, and it concentrates at the interior regions of the two femoral extremities, also called epiphysis. Moreover, the femur bone contains yellow marrow in its medullary cavity, a region in the diaphysis (the tubular shaft of the femur). Figure 3.4, is an illustration of a longitudinally oriented section of the long bone where the spongy and compact bone, as well as the medullary cavity and yellow marrow, are represented.

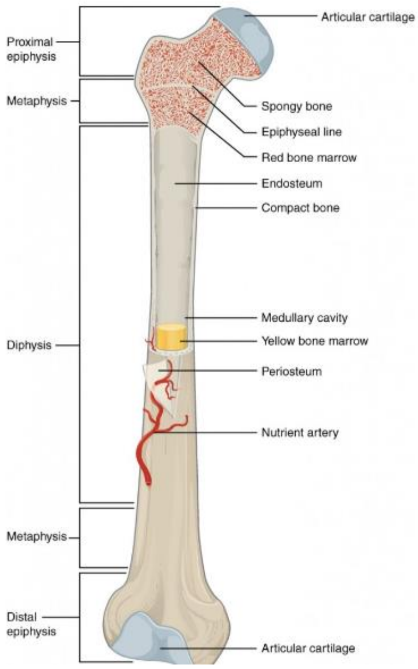

Figure 3.4 - Internal Anatomy of the femur bone

(https://courses.lumenlearning.com/hccs-ap1/chapter/bone-structure/)

The cortical bone is an anisotropic material that presents superior values of the compressive and tensile strengths at the longitudinal direction when compared to the radial and circumferential direction, however, the same strength moduli measured at the circumferential and radial directions do not present significative differences among their values, what allows this bony tissue to be considered transversely isotropic (Morgan et al., 2018). In table 3.1, are presented the compact bone's ultimate compressive and tensile strengths and its Young's Modulus extracted from Mirzaali et al. (2016), as well as the Poisson's ratios obtained in Reilly and Burstein (1975), measured in the longitudinal directions. Table 3.1 also displays the same mechanical properties but measured in the transverse direction, that were collected from Reilly and Burstein (1975). The ultimate strengths and Young's Modulus are given in MPa.

Table 3.1 – Mechanical properties of the cortical bony tissues in the longitudinal and transverse directions

Mechanical Properties	Longitudinal Direction	Transverse Direction
Ultimate Compressive Strength (MPa)[a]	$153,59 \pm 21,63$	$131 \pm 20,7$
Ultimate Tensile Strength (MPa)[a]	$92,95 \pm 10,07$	$53 \pm 10,7$
Young's Modulus (MPa)[a]	18160 ± 1880	10100 ± 2400
Poisson Ratio[b]	$0,62 \pm 0,26$	$0,62 \pm 0,26$

from (a) Mirzaali et al. (2016) and (b) Reilly and Burstein (1975)

As the cortical tissue of the femur, the trabecular bone is an anisotropic material that exhibits higher strengths at compression than in tension, however, the typical variations in the spatial arrangement of trabaculae (trabecular architecture) and in the density of the trabecular bone result in the heterogeneity of the measured elastic and strength properties (Mirzaali et al., 2016). The Young's Modulus of the trabecular bone can vary from 10 to 3000 MPa (Morgan and Keaveny, cited by Mirzaali et al., 2016), while the strengths can range from 0,1 to 30 MPa (Ciarelli et al., cited by Mirzaali et al., 2016).

During the lower limb's locomotion, the muscles that are attached to the femur bone are responsible for the direct application of muscular forces into its structure, and those attachment points can be muscular origins or insertions. Among the muscles with origins in the femur are the vastus lateralis, vastus intermedius, vastus medialis, articularis genu, biceps femoris brevis (short head), plantaris, gastrocnemius, and popliteus. Whilst, the muscles inserted in the femur are the Iliacus and psoas major (ilopsoas), pectineus, obturator externus, obturator internus, superior and inferior gemelli, quadratus femoris, piriformis, gluteus medius, gluteus maximus, gluteus minimus, adductor magnus, adductor brevis, adductor longus. Figure 3.5 is a representation of the muscular attachment regions of the hip and femur, and the muscles with origins and insertions in the femur bone are indicated inside the rectangular shapes, except for the articularis genu and popliteus which are not indicated in the image.

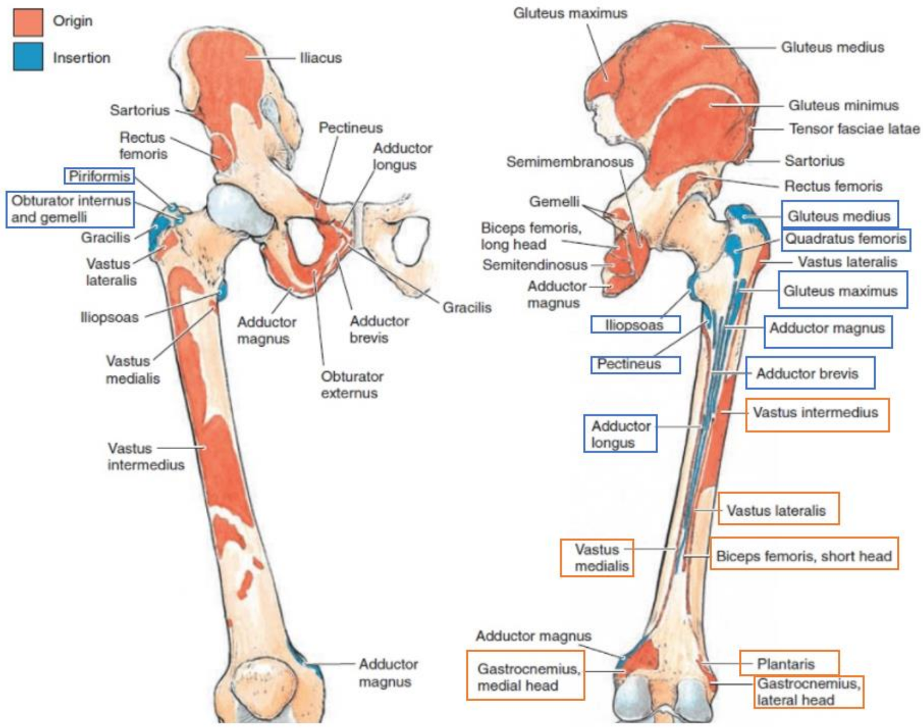

Figure 3.5 - Muscular attachment regions of the hip and femur bones

(https://books.google.com.br/books/about/The_Massage_Connection.html?id=o95f8iLXa9cC&redir_esc=y)

Some of the muscles attached to the femur are responsible for a more expressive contribution to the possible rotational movements of the hip joint, mentioned in chapter 2. For instance, the gluteus maximus provides the extension of the hip, while the iliopsoas is the major contributor to the flexion. Piriformis, quadratus femoris, and gameli act in the external hip rotation. The adductor brevis, longus and magnus help the adduction of the hip. The gluteus medius and gluteus minimus are the main muscles responsible for abduction of the hip joint, while also balancing the pelvis in the swing phase of the gait cycle (the second of the two broad phases that comprise a gait cycle, which is followed by the swing phase). Figure 3.6 is a representation of the anterior muscular groups involved in the hip joint locomotion, while figure 3.7 presents the posterior hip musculature.

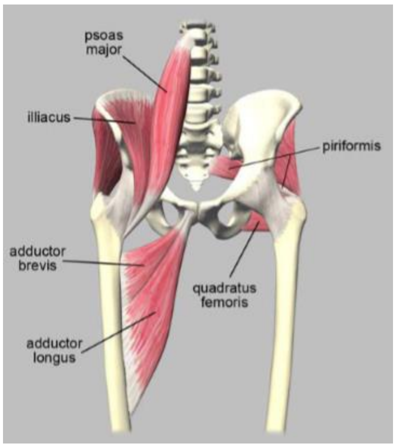

Figure 3.6 - Muscular groups of the anterior hip

(Buechel and Pappas, 2015)

Figure 3.7 Muscular groups of the posterior hip

(Buechel and Pappas, 2015)

Chapter 4 - The use of PMMA in total hip arthroplasty

Hip arthroplasties using cementing techniques were first described in 1981 when Glück used methacrylate bone cement for prosthetic fixation (Knight et al., 2011). In 1958, Charnley had employed acrylic bone cement in hip replacement surgery motivated by the recognition of its ability to fill the medullary canal and adapt to the bone interface (Smith, 2005), to promote the anchorage of the femoral head prosthesis and the femoral shaft component (Charnley, 1960). The evaluation of the outcomes of this joint replacement method has provided the basis for the development of Charnley's *Low Friction Arthroplasty* (Smith, 2005).

The acrylic bone cements used in Charnley's first surgical interventions were polymethylmethacrylate based, also called PMMA bone cements (Smith, 2005), and this material is still vastly used in hip replacement surgeries, and other types of orthopaedic surgery, such as kyphoplasty and percutaneous vertebroplasty (Webb and Spencer, 2007). In this chapter, the chemical composition and the stages of its curing processes will be presented. Then, its mechanical properties and their influence on the hip implant will be discussed. Finally, its structural role in femoral implant will be described as well as some limitations due to this material usage will be addressed.

4.1 Chemical Composition and Curing Process

PMMA is produced by mixing a Methyl methacrylate (MMA) liquid monomer with a Polymethyl methacrylate (PMMA) powder copolymer, in an exothermic reaction of polymerization where the liquid monomer polymerizes around the pre powder particles of the copolymer (Vaishya et al., 2013). An initiator of the chemical reaction (Benzoyl peroxide) is added to the powder and an accelerator (N, N-Dimethyl para-toluidine, or diMethyl para-toluidine) to the liquid monomer to allow the polymerization at room temperature, due to the high sensitivity of the bone cements to temperature variations from the recommended temperature of 23°C (Vaishya et al., 2013). Other chemical components are added to the bone cements, such as stabilizers like the Hydroquinone to prevent early polymerization due to light and heat exposure, radio-opacifiers like barium sulfate or zirconia that can make the cement radiopaque (be visible on X-ray), and antibiotics (e.g., Gentamycin, Tobramycin, Erythromycin) to prevent infection in the periprosthetic tissues, which must be heat resistant and have a long duration.

The cement preparation is also called cold-curing cement, because the polymerization reactions take place at room temperature, and happens in four consecutive stages which are, respectively, the mixing phase (when polymerization occurs), the waiting or sticky phase, the working phase, and the hardening phase (Vaishya et al., 2013). The waiting phase is the time it takes for the cement to no longer have the mechanical properties exhibited after the mixing phase (adhere to surfaces like surgical gloves). The working phase corresponds to the time when the cement can be manipulated and implanted, while, in the hardening phase the hardened bone cement is formed. The overall period of the cement curing is called setting time.

4.2 Short and long-term mechanical properties

PMMA bone cements are brittle materials with relatively low compressive and medium shear strengths when compared with their compressive strengths (McCaskie, 2000). Up today the ISO 5833:2002 is the international standard used to measure the working and static strengths of bone cement through tests in laboratory conditions (Webb and Spencer, 2007). The data in table 4.1 was extracted from Webb and Spencer (2007), and it represents the summary of the static properties of the then leading cement brands. However, those standardized tests disregard the long-term properties that are of fundamental importance for the THR stability, such as the fatigue behavior and the creep and stress relaxation properties.

Table 4.1 – Mechanical properties of leading cement brands

(From Webb and Spencer (2007))

Static Properties	Range (MPa)
Ultimate tensile strength	36-47
Ultimate compressive strength	80-94
Bending strength (4 point configuration)	67-72
Shear strength (ASTM D732)	50-69
Mean fracture toughness (K_{IC})	1,52-2,02 $MPa\sqrt{m}$

4.3 Structural Role in the implanted femur

When used in femoral stem fixation, the PMMA works as a grout, by filling the space between the prosthetic components and bone and holding the implant in place. The mechanical bond in the cement-bone interface is not adhesive, instead, it is a result of the microinterlock mechanism, as mentioned in chapter 2 (Vaishya et al., 2013). It is also through the cement mantle where the load applied to the prosthesis is transmitted to the bone (McCaskie, 2000), and in a larger interfacial area than in the cementless implants (Webb and Spencer, 2007). Having Young's modulus about 2400 MPa, PMMA cement mantles work as a less stiff layer between the femoral stem and the cortical bone, with a good capacity to absorb shock (Lee, 2000). However, because of its reduced mechanical strength, when compared to the stem and cortical bone, in some cases, the PMMA cement mantle and their interfaces have the adverse characteristic of acting as structural weak-links (Harrigan et al., 1992, cited by, Webb and Spencer, 2007), being susceptible to damage and interfacial failure.

Among the advantages of the use of the PMMA cement mantle is its role in the minimization of the stress shielding phenomenon. Huiskes (1990) found that cemented stems have higher stresses at the proximal region of the femur when compared with cementless stems and, hence, concluded that the effects of cortical stress shielding are milder in cemented stems. Similar conclusions are presented by Chen et al (2004), in a study comparing stress shielding among different cement fixations. However, the cemented implants' stability can be compromised by factors such as the low cement-bone interfacial strength caused by volumetric shrinkage of the PMMA after the curing, aseptic loosening associated with bone damage caused by PMMA constitutive monomer, and aseptic osteolysis initiated by wear cement particles. Also, during the polymerization reaction, 1,4 to 1,7 x 10^8 J/m³ of heat is liberated, and the high temperatures induced in the bone can lead to thermal necrosis (Webb and Spencer, 2007).

Chapter 5- Types of THR cemented femoral stem designs

The THR femoral stems have been classified into three groups accordingly with their design philosophy for fixation of the stem and transmission of load (Lee, 2000). For this classification system, the stem types are divided into two broader groups of cemented stems, the composite beams and the loaded-tapered, and in one group comprising the cementless stems. In this section, it will be introduced the general characteristics of the types of fixations of the shape-closed and force-closed stems, and their influence on the short and long-term stability of the femoral implants.

5.1 Shape-Closed

Shape-closed or composite-beam stems are commonly designed with a satin matt surface finish, or a collar, or an altered geometry, or a combination of these features, to ensure the initial stability of the implant, the stem subsidence prevention, and the direct load transmission to the cement mantle (Hutt et al., 2014). With perfectly bonded cement-stem and cement-bone interfaces, the biomechanical structure formed by this type of stem, the cement mantle, and bone tend to deform as a composite-beam when under loading (Lee, 2000). Typically, the stresses developed in cement interfaces are high shear stresses, low compressive and tensile stresses.

If the implant's cemented interfaces don't fail, this philosophy of fixation can offer advantages, such as the reduction of the micromotion in the cement-stem interfaces (the small relative motion between the faces of cement and stem), which consequently reduces the production of debris particles that are responsible for implant loosening due to mechanical wear, minimizes the variation on internal pressure and the tensile stresses within the cement that might lead it to crack (Hutt et al., 2014). But, if for some reason the cement isn't well fixed into the bone, the entire structure is likely to fail, therefore, the bone-cement interface to be considered fundamental for the long-term survival of THR. For instance, if micromovement occurs, long-term clinical problems can appear in the implant construct, like the fretting wear, which is also responsible for stem loosening induced by the production of cement particles and metal microparticles throughout this interface (Kwong K. S., 1990). Moreover, the production of wear particles due to fretting wear can get aggravated in stems with rough surfaces (Hutt et al., 2014). An alternative to prevent the bone-cement interface failure would be to increase the mechanical strength in the interface between bone and cement but, unfortunately, even if the surgeons make attempts to make the bone-cement bond stronger, through lavage and cement pressurization, for example, the final strength of this interface is always limited to the strength of the bone in the most ideal cases (Lee, 2000).

Furthermore, there is also debate about the usefulness of the collar in the shape-closed stems. This feature has the potential to promote the direct load transfer from the stem to the medial cement mantle and medial femoral neck, which can allow the reduction of the stresses in the interfaces at the proximal cement, and the minimization of bone loss due to stress shielding in the proximal femur (Hutt et al., 2014). Ideally, if the axial loading is transferred to the medial femoral neck as in the natural femur, the bone loss in this region due to stress shielding is minimized (Kwong K. S., 1990). However, the collar does not prevent micromotion or calcar resorption (bone loss due to underloading). Markolf, Amstutz, and Hirschowitz (1980) reported that even when there is collar-to-calcar contact, the stem experiences a little subsidence. The load transmitted by the collar to the calcar bone was measured by Crowninshield, it is 50% inferior to the ideal value to prevent calcar resorption. Also, there is evidence of disuse atrophy at the calcar region under a well-fitting collar might suggest that for well-fixed stems the collar is redundant, even if a close contact is ensured between collar and bone (Hutt et al., 2014).

5.2 Loaded-Tapered

Loaded-Tapered or force-closed stems are designed to migrate towards a stable position during the initial phases after surgery (Hutt et al., 2014). They are always collarless, have tapered shapes, and a polished surface finish, characteristics that make use of the long-term properties of creep and stress relaxation of cement (Lee, 2000). The polished surfaces result in lower coefficients of friction in the stem-cement interface, therefore, the maximum shear stresses that can be developed, without micromovement at this region, are reduced to lower levels than the ones experienced for the interface construct of stems with a rougher finish (Lee, 2000). The lower friction of the force-closed stem within the cement, when compared to matt surface stems, allows smoother subsidence, with decreased production of debris (metal and cement particles) due to stem movement within the cement (Hutt et al., 2014). Moreover, the debonding rate in the cement-stem interface of satin matter stems is proven to be higher when compared with stems with polished faces, the surface finishing used in force-closed designs (Mohler, 1995). Also, aseptic loosening is more likely to occur in stems with a rough surface finishing than in polished stems (Della Valle et al., 2005).

While still subsiding within the cement, the force-closed stems explore the creep and stress relaxation properties of the PMMA. In normal patients, the stems undergo daily loading cycles that are divided into loaded periods, when the patients execute their daily activities, and unloaded periods when the patients take more prolonged rest (Lee, 2000). The hip joint loads are transmitted to the stem during the patient's daily activities, and the strain energy and creep deformation of the cement absorbs the stem displacement in the mantle, while its movement transmits tensile hoop stresses and radial compressive stresses to the cement (Lee, 2000). During unloaded periods, the stem gets engaged into the cement and does not return to its initial position, therefore, to decrease the strain energy the deformed cement undergoes a stress relaxation process where the tensile stresses are expressively reduced, but the compressive stress levels remain the same (Lee, 2000). The result of these loading cycles associated with the viscoelastic properties of the bone cement is to protect the cement from fatigue failure due to the tensile stresses and to improve the long-term stability of the THR due to the increase in the compressive stresses acting on the cement interfaces and within it (Lee, 2000). For force-closed designs, the stem subsidence normally occurs in the first two years post-operatively, after this period of time it can get reduced or can completely stop (Kiss et al., 1996, cited by Cassar-Gheiti et al., 2020), and if there is *continued subsidence* or a stem displacement of more than 5 mm after this time the stem displacement must be considered as permanent loosening (Harris et al., 1982, cited by Cassar-Gheiti et al., 2020). With the third generation cementing techniques, the use of the distal centralizer has started to be practiced, this component not only helps with the stem centralization in the medullary cavity but also allows more controlled subsidence.

Chapter 6 – Development of the THR Models

Models of cemented femoral implants with force-closed stems, from primary and revision hip replacement surgeries, were created aiming to employ the finite element method to simulate the static load transmission across the implant components during walking. A total of two models of primary THR were created, each with different stem sizes, as well as two groups of revision surgery models. Each revision group was created using one of the primary models as a reference and has a total of three revision THR models, therefore, a total of six revision models have been developed.

All models are formed by the ***femur bone*** and ***prosthetic components*** which were modeled after a careful study on the operative techniques deployed in the hip replacement surgical procedures. In the following sections, details about the model preparation regarding geometrical design, mechanical properties of the models' constitutive materials, acting load profiles transmitted to the cement mantles, and the configuration of the mesh elements used for the calculations will be presented.

6.1- Model Design, Mesh Elements Configuration, and Model Fixation

Aiming to simplify the system of partial differential equations in the finite element calculations, only the most relevant elements for the simulation of the biomechanical loading on the THR models were kept, namely, the femur bone (with cortical and trabecular tissues), the cement mantles, and the femoral stem without its modular head. Therefore, the bone marrow and some of the prosthetic components which are typically present in those implants were left out, such as the cement restrictor, and distal centralizer. Figure 6.1 is a representation of the complete and simplified implant constructs, where the cortical bone is displayed in low opacity to allow the observation of the interior components. It is possible to observe the absence of the yellow marrow at the most distal part of the implants, in both model types. There are more details about the excluded prosthetic accessories in Appendix A.

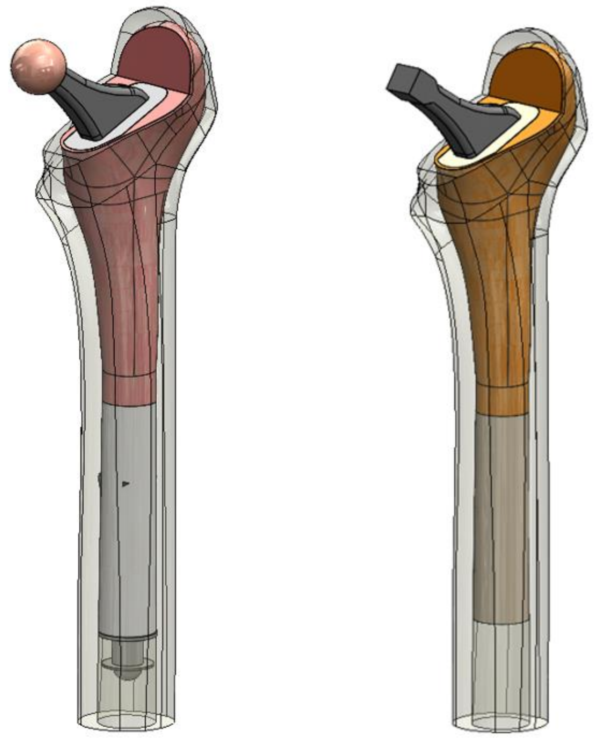

(a) (b)

Figure 6.1 Example of a (a) complete and a (b) simplified THR model

The ***femur bone*** was modeled with the trabecular and cortical tissues. The cortical bone present in the study was derived from a 3D model obtained in a catalog of femur bone models from SawBones®. The model of the trabecular bone is an entirely new design and, in order to simplify its geometry, the trabecular network was not modeled; instead, this bony structure was designed as a solid without porosities. Both of these femur bone structures underwent modifications to replicate the femoral osteotomy and the femoral canal perforation. The femoral stem was placed into the femur and aligned into the medullary canal, before the modeling of the femoral operations got executed. The osteotomy level was placed 19 mm, at a normal distance, above the level of the lesser trochanter with an inclination of approximately 19 degrees with respect to the transverse plane. All bone geometries above this reference plane were removed, except for a considerable portion of the greater trochanter. Furthermore, following the recommendation found in Stryker® (2018), the canal perforation was modeled keeping the minimum thickness of the trabecular bone around the cemented stem between 2 and 3 mm.

With regards to the **prosthetic components**, a set formed by PMMA cement layers and force-closed stems was created. The femoral stems were designed without a collar, and have slim geometries, polished surfaces, and tapered shapes. The stems' base dimensions considered were the same as the ones described in detail in different manufacturer's manuals of collarless metallic prostheses: the stem length, the antero-posterior width, medio-lateral width, the neck height, and the neck offset. During these components design special care was taken to ensure an appropriate alignment within the femur model, with a good correlation between the anatomic axis of the femur (the femoral neck axis, and the proximal part of the femoral anatomical axis) and the axes of the stem, where a perfect alignment was ensured between the neck axis of the stem and the femoral neck axis. Two stems were designed, one with a smaller stem length that received the size designation of 0H, the other with a longer stem length that was identified as a 1H size, following the Smith and Nephew designation system. In Appendix A, are given more details about the stem's dimensions and the designation system.

The cement mantles in the two primary surgery models were created by filling the space between the femoral stems and the perforated trabecular bone with a new solid, where the mantle thicknesses around the stems are between 2 and 5 millimeters, as recommended for this clinical usage (Ebramzadeh et al., 1994). **For the design of the cement mantles in the revision surgery models**, two solids were created to represent the well-fixed and the new cement mantles. The well-fixed cement was prepared considering the loss of the volumes of cement around the stem which is a result of the prosthesis extraction, and the removal of the well-fixed cement above the level of the lesser trochanter that is practiced in the in-cement revision surgery (Duncan et al., 2009). The mantle made of new cement was designed to fill the spaces between the placed stem and the remaining well-fixed cement layer. As well as for the trabecular bone models, all cement mantles were designed without porosities.

All revision THR models have 0H sized stems, where three of them were designed using the primary THR model with the stem with 0H size as a design start point, and in this work are referred to as 0H/0H models. The other three models are designs based on the primary THR models with the 1H size stems, being called 1H/0H models. The models that are related to each of these two designations were designed with different new cement mantle thicknesses around the stem, where the employed values were constant around the stem axis in the radial direction, and equal to 0,8 mm, 1,2 mm, and 1,6 mm. Finally, aiming to simplify the finite element calculations, a resection cut was made in all the models transversely to the mid diaphysis. The cross-sections generated after this cut were used as surfaces of fixation for all models, therefore, this cut had to be located in a region where the resultant loads acting around the femoral stem wouldn't be influenced by the boundary effect, at a distance from the stem tip equal to two times the diameter of the diaphysis, accordingly with the St. Venant´s Principle (Duda *et al.*, 1998). Figure 6.2 is a representation of the two types of design transitions, from primary to revision models, that were examined in this work (0H/0H and 1H/0H), where the primary and revision THR models are represented by longitudinal section views.

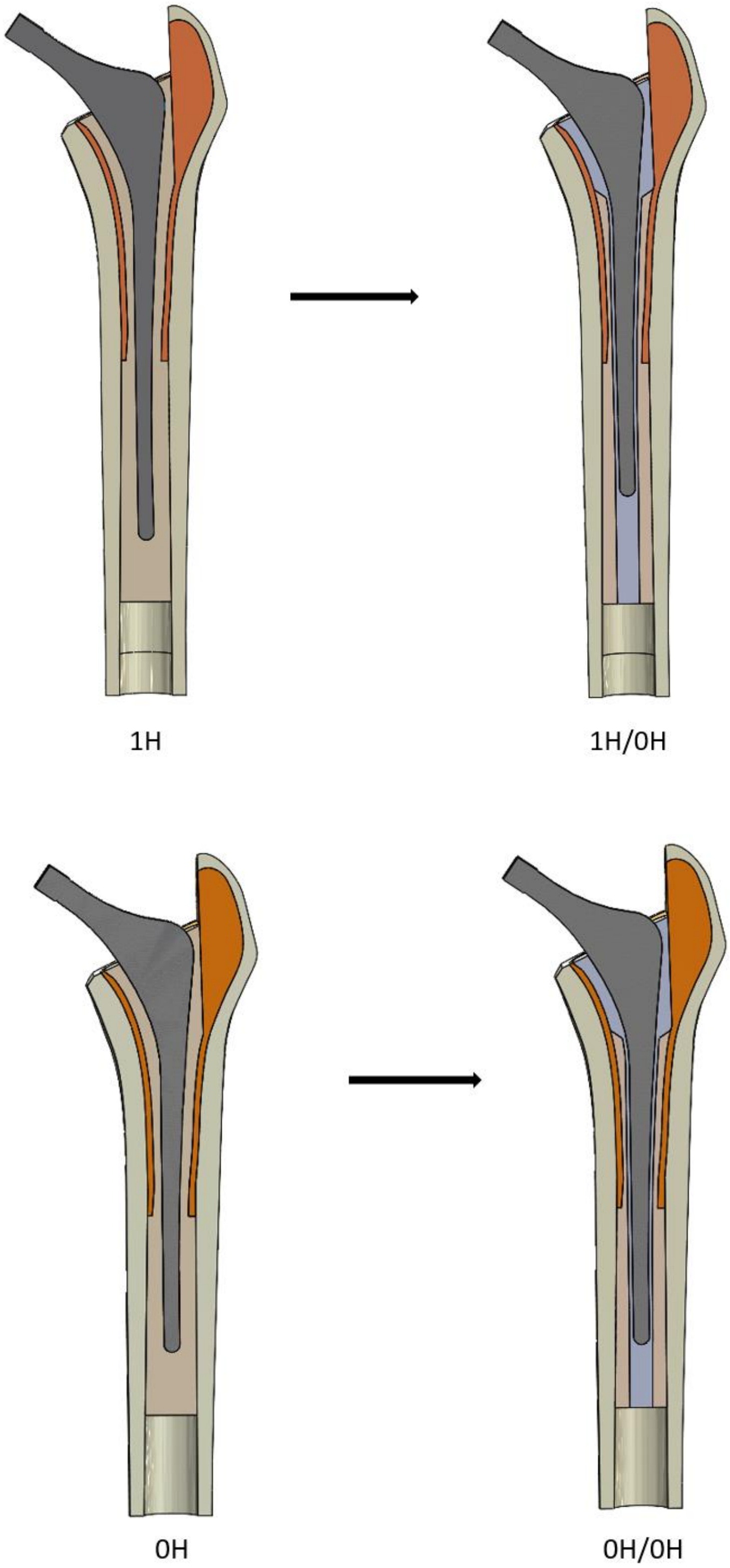

Figure 6.2 Design transitions of the implanted femur structure from the primary 1H and 0H THR models to the 1H/0H and 0H/0H revision models

Meshes with solid elements were generated to conduct the static studies on the representations of the implanted femur using SolidWorks, where the element type used in the discretization of each model has a curvature-based shape (parabolic tetrahedral solid elements). This mesh element configuration was employed aiming to represent the complex curved geometries in the models more accurately and to make possible better mathematical approximations. Moreover, it is important to address that each model component has gotten meshed independently, therefore, the mesh continuity at different bodies interfaces is of the type incompatible (with no node-to-node correspondence). In Appendix B, there is information about the number of elements and their size in the meshes configured for each THR model in order to obtain the results discussed in the present work. In Figure 6.3, there is a representation of the meshed components of the 0H primary THR model, while figure 6.4 shows the models of the well-fixed and new cement mantle from the 0H/0H revision THR model, for a cement mantle with 1,2 mm thickness around the stem.

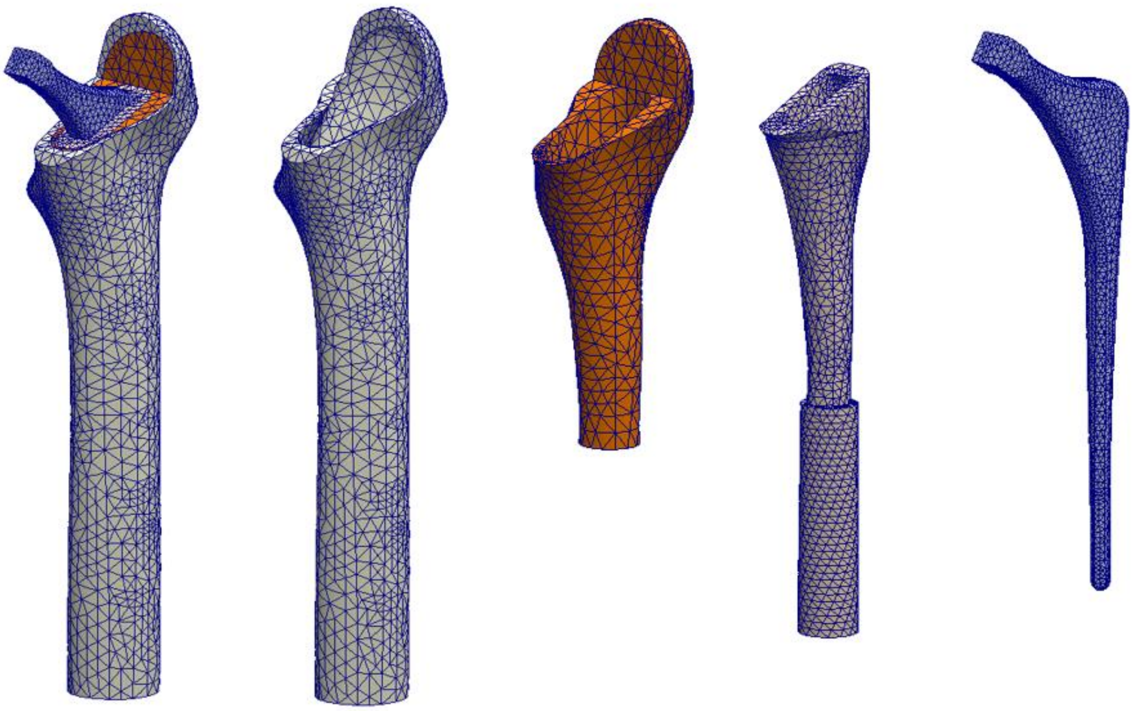

(a) (b) (c) (d) (e)

Figure 6.3 Representation of the: (a) final mesh of the assembly, (b) the cortical bone, (c) trabecular bone, (d) cement layer, and (e) metallic stem of the 0H primary THR model.

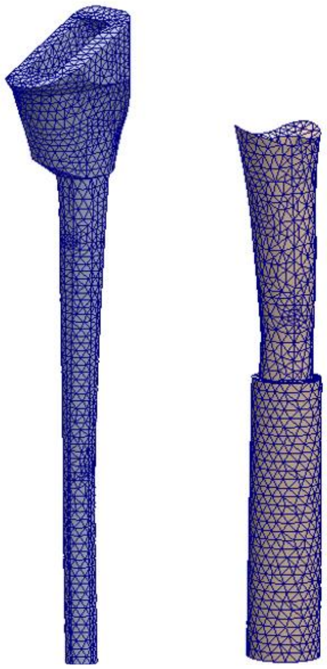

Figure 6.4 – Final mesh of the (a) new cement and (b) well-fixed mantle from the 0H/0H revision THR model

6.2- Materials characterization

The femoral stem has had to be designed to have a slim shape to be more adequately fit into the femoral canal and to allow the cement mantle to have the appropriate thickness, therefore, the attributed material for this prosthetic component had to be stiff enough to ensure good stability within the cement. The stainless steel for surgical implants ASTM F1586 (316L) is a commonly used material to manufacture the femoral stems and, due to its high modulus of elasticity of 200 GPa, its mechanical properties were applied in the material characterization of the femoral stem. The mechanical properties of the trabecular and cortical bones, and of the PMMA bone cement types were defined following the material's characterization found in previously published works. Because a deeper study about the transverse and longitudinal stress distributions in the bone models was not one of this work's objectives, to simplify the finite element analysis, the materials' anisotropy of the cortical and trabecular bones was not attributed to the models. Therefore, the bones' physical properties were defined after the data of the mechanical properties of a real femur bone which are presented in Lennon and Prendergast (2001), where the cortical and cancellous bones are considered to be isotropic materials. Regarding the old and new PMMA bone cement, their material characteristics were defined after the data extracted from Simões et al. (2010). Table 6.1 summarizes all the mechanical and physical properties defined for those materials that were relevant for the finite element simulations in the present work.

Table 6.1 – Young's modulus and Poisson's ratios attributed to the 3D model components

	Young's Modulus (GPa)	Poisson's Ratio
Old Cement [a]	2,08	-
New Cement [a]	2,12	-
Metallic Prosthesis [b]	200	0,30
Cortical Bone [c]	17	0,33
Trabecular Bone [c]	1,5	0,33

From (a) Simões et al. (2010), (b) Sandvik®, (c) Lennon and Prendergast (2001)

6.3- Gait Loading Modeling

The loads applied into the model are representative of the forces acting on the proximal femur due to the muscular action and the hip-joint contact forces, at an instant during walking. This set of forces was determined using as a basis the simplified musculoskeletal model presented in Heller *et Al.* (2005) which is a derived load profile developed for pre-clinical testing of femoral shaft components, that considers a moment of maximum in vivo hip contact forces in a full gait cycle. Their model included the hip joint contact forces and the action of a simplified hip muscles group that was capable of providing physiological-like loading conditions at the regions where the implanted stem is located: the proximal femur. Their derived loading profile defined for walking is composed of: a simplified abductor muscle which executes the approximate function as the gluteus minimus, medius, and maximus; vastus lateralis, and the proximal and distal parts of the tensor fasciae latae. During the profile's definition, the muscles with no attachment sites at the proximal femur and that, consequently, do not exert direct forces in the bone were removed. Also, the muscles that are responsible for small force contributions during gait were removed without compromising the physiological-like results. The tensor fascia latae was only included because, despite not being directly attached to the femur, after its removal, it was observed a substantial increase in the hip joint contact forces and the forces in the remaining muscles.

Both hip-contact and muscular forces were given in terms of the same bodyweight percentages determined in Heller *et Al.* (2005) for a "typical patient" weighing 836N, however, the body weight employed in this work was 735N, which is slightly superior to the one used in the finite element model studied in Lennon and Prendergast (2001). Those force components, as well as points of application, were addressed in a cartesian coordinate system defined accordingly (Bergmann et al., 1993). Its z axis was defined to have the same orientation of the line that connects the point of intersection between the **curved femoral midline** and **neck axis** with the point where the cortical bone of the **intercondylar notch** intersects with the **femoral midline**. The x and y axis were defined as two pertaining axes to the frontal plane, with the x axis pointing medially and the *y* axis pointing anteriorly. The femoral **frontal plane** is the plane that contains the z axis and is parallel to the knee axis, while the knee axis is collinear to the line that connects the centers of the circles that can describe the femoral condyles in the lateral views. In figure 6.5, are indicated P1 and P2, which are the attachment or wrapping points of the muscles from the loading profile, and P0 which is the point of action of the hip joint reaction forces, as well as the origin of the coordinate system. Table 6.2 contains the coordinates of the points P0, P1 and, P2; while in table 6.3 are indicated the force components of each muscle.

Although the same method to define the coordinate system was implemented in both works, in the present study, the femur bone model is not the same as the one used in Heller et al (2005), therefore, points of muscular action had to be addressed at the most approximate locations on the femoral surface of the model, resulting in slightly different coordinates from the ones defined in Heller et al (2005).

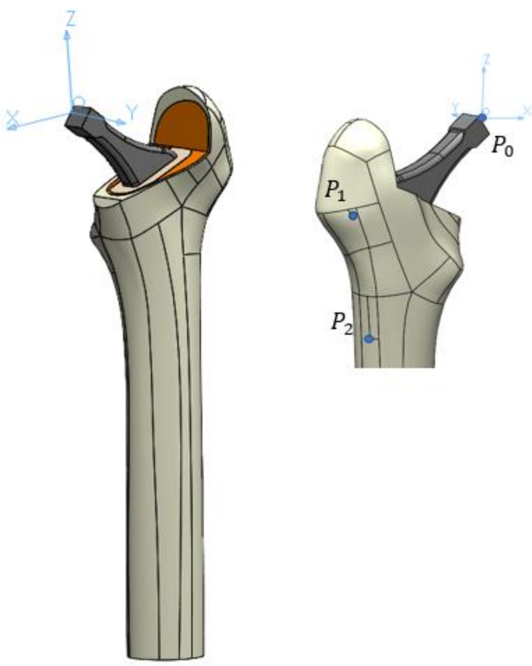

Figure 6.5 Representation of the reference frame and of the points of muscular action and hip contact

Table 6.2 – Coordinates of the points of muscular force applications

	Coordinates (mm)		
	x	y	z
$\boldsymbol{P_0}$	0	0	0
$\boldsymbol{P_1}$	$-62{,}54$	$-7{,}72$	$-34{,}90$
$\boldsymbol{P_2}$	$-49{,}94$	$-5{,}37$	$-79{,}80$

Table 6.3 – Components of the hip contact and muscular forces, exerted in the proximal femur, for a 735N body weight

Walking (%BW)	$\boldsymbol{BW = 735\ N}$		
	F_X	F_y	F_z
Hip contact $(\boldsymbol{N})$	$-396{,}90$	$-241{,}08$	$-1684{,}62$
Abductor $(\boldsymbol{N})$	$426{,}30$	$31{,}60$	$635{,}77$
Tensor fascia lata, proximal part $(\boldsymbol{N})$	$52{,}92$	$85{,}26$	$97{,}02$
Tensor fascia lata, distal part $(\boldsymbol{N})$	$-3{,}67$	$-5{,}14$	$-139{,}65$
Vastus lateralis $(\boldsymbol{N})$	$-6{,}61$	$-135{,}97$	$-682{,}81$

6.4 - Interfacial Contacts Configuration

Ensuring an adequate configuration of the contacts in the models' interfaces is fundamental to obtain results from the static simulations that translate the influence of those mechanical contacts in the stress distributions of the whole implant construct, more approximately to what would be observed in vivo. Ideally, a realistic model of an implanted femur would have to include the representation of the microinterlock between the trabecular bone and the bone cement, unfortunately, to model the cement fixation in a trabecular network would require the inclusion of microscopic geometries that could very difficultly be discretized using finite elements. As well, it is known that the presence of some interfacial contaminants, such as the debris particles and blood, can influence the quality of the interface fixations, but to evaluate the effects of the presence of these materials was not among the objectives of this work.

In all models, the interface between trabecular and cortical bone, and the cement-bone interface were configured to be perfectly bonded. In the models with two layers of cement, the contact between the mantles' faces was also defined as perfectly bonded. Regarding the stem-cement interface, two conditions of contact were modeled, one where the interface got a debonded configuration, in which the stem would still subside within the cement, and the other with a completely bonded interface, where subsidence does not take place. To model the cement-stem debonded interface, a node-to-surface contact was defined with a coefficient of friction of 0,35, therefore, only the slipping component of micromovement was taken into account. The coefficient of friction was determined based on a study developed by Nuño Groppetti and Senin (2006) which addresses that a coefficient of friction of 0,3 to 0,4, between stainless steel and PMMA used in cemented hip and knee implants, can be appropriately used in finite element models.

Chapter 7 - Model Validation

The evaluation of the stresses acting in the elements pertaining to the THR models relied exclusively on numerical results of the finite element analyses. Therefore, the validity of those results was attested through a comparative study based on the outcomes of a published work that have examined a similar model. The elected study was the analysis of the stress distributions acting in the cemented implant from a primary THR model conducted in Lennon and Prendergast (2001), in which a good correlation was found between the strains predicted in their final element model with the ones found in experimental tests. This selection was motivated because the present study's primary THR models basically consist of the same elements as the ones created in their work (such as a femur bone and a collarless cemented stem). Also, their work was, in the same manner, a static analysis that considered a loading profile that only represented a moment in gait where the forces acting on the femur reached their highest values, which included as well: similar geometrical simplifications, models' constraints, interfacial contact configurations, and material properties characterizations. It is important to address that the comparison of the current simulations' results with the ones from the primary THR model studied in Lennon and Prendergast (2001) was carried out because no published study was found, where a finite element analysis had been conducted for the evaluation of the stresses in the components of a hip replacement revision surgery, using the in-cement technique.

Furthermore, despite the similarities between the model's setup, it wasn't possible to establish a quantitative correlation between results due to the existence of specific differences between the models. The geometries of the composite femur bone, cement layer, and prosthetic stem present considerable differences between each model, as well as some material's mechanical properties. Moreover, the load profile configured in Lennon and Prendergast (2001) was derived from the data from Bergman et al. (1993) and Duda et al. (1998). These differences between loading profiles and geometries wouldn't allow, for example, a direct comparison of the calculated peak stress values, or the percentage of cement volumes subjected to a certain stress value threshold. Therefore, the comparison of results from both analyses was made qualitatively, and in terms of the observation of two results evaluated in Lennon and Prendergast (2001): the Contours of Cement Stress (maximum principal tensile stresses), and the Direction of Stress in Cement Mantle (hoop and longitudinal tensile stresses relatively to the stem axis). The location of peak stresses was not used as a determinant parameter for the qualitative comparison due to its strong sensibility to the geometrical characteristics of the model's components, which can result in maximum stresses acting in different locations that may contain stress concentration regions.

Because of this method's qualitative nature, only the results, obtained from the 0H primary model, were used to implement the comparisons.

In Lennon and Prendergast (2001), the stress distributions were evaluated for three biomechanical scenarios. In one of them, a debonded case of cement-stem fixation with frictional contact was analyzed, in a mantle that had its most distal section removed. In the other two, the PMMA cement mantle was intact, where, in one, the cement-stem interfacial contact was configured as totally bonded, and, in the other, this interaction was configured as debonded with friction. Because in the present work, the employed cement-stem contact configurations were also the perfectly bonded and debonded with friction, and none of the THR models were analyzed considering the extraction of volumes of distal cement, the qualitative comparisons were conducted considering the results obtained for the intact mantle evaluated in Lennon and Prendergast (2001).

The contour of cement stresses, which were examined in Lennon and Prendergast (2001) were obtained from the stress plots of the first or maximum principal tensile stresses exerted in the cement mantle, and the central aspects considered for their examination were the distribution of the highest stresses and the location where they have reached peak values. The definition of high tensile stress used in this work was dependent on the stress value determined with the probability of failure calculations, presented in chapter 9, above which a chance of failure exists for a given number of loading cycles. Accordingly with these calculations, the highest stresses were considered to be superior to 3MPa.

A considerable number of similarities were found in the contour of maximum principal stresses in both works. Firstly, as in the results found in the previous work, for the bonded cement-stem configuration in the THR model, the peak stress was exerted at the upper side of the proximal section and the high stresses regions are found at the proximal and distal sections of the mantle, however, the high stresses are not found in the whole extension of the medial and lateral sides, as what was observed in Lennon and Prendergast (2001). Secondly, for the debonded case of fixation, there was also an increase of the regions under higher tensile stresses at the proximal medial side and around the distal tip, although in the present study the high-stress regions have also significatively increased at the proximal lateral side; but the maximum stress was found to be located at the upper side at the proximal section, not around the distal tip as in Lennon and Prendergast (2001). More detailed discussions about the contour of stresses of the models developed for this work are presented in chapter 8. Figure 7.1 is the representation of the maximum principal stress plots in the cement mantle of the 0H primary THR model for the bonded and debonded cases of stem fixation, with the indication of the points of maximum and minimum stresses, while figure 7.2 shows the distribution of those stresses above 3MPa.

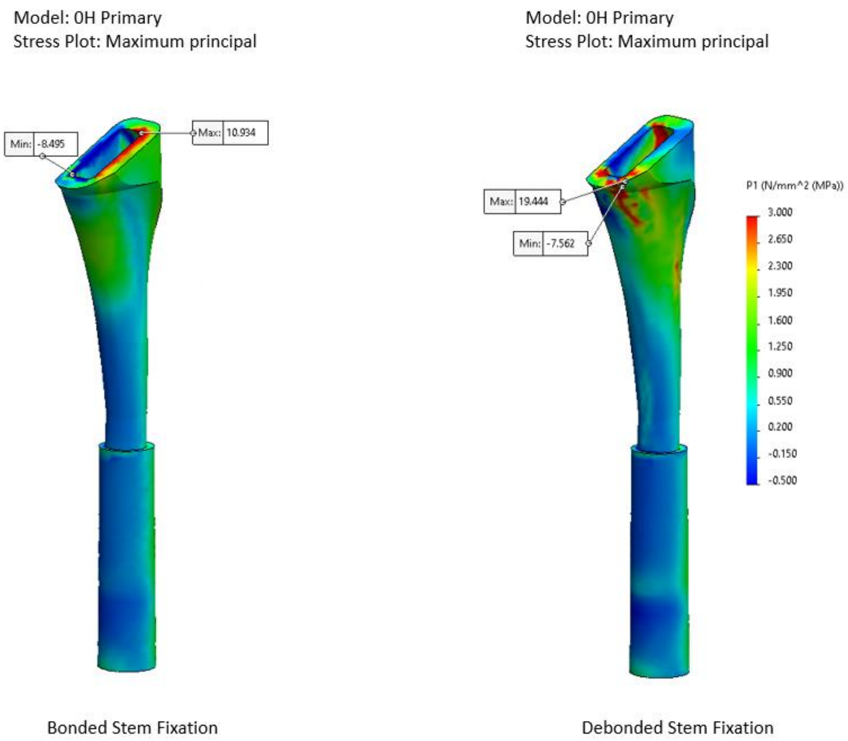

Figure 7.1 – Principal stress distributions in the cement mantle from the 0H primary THR model

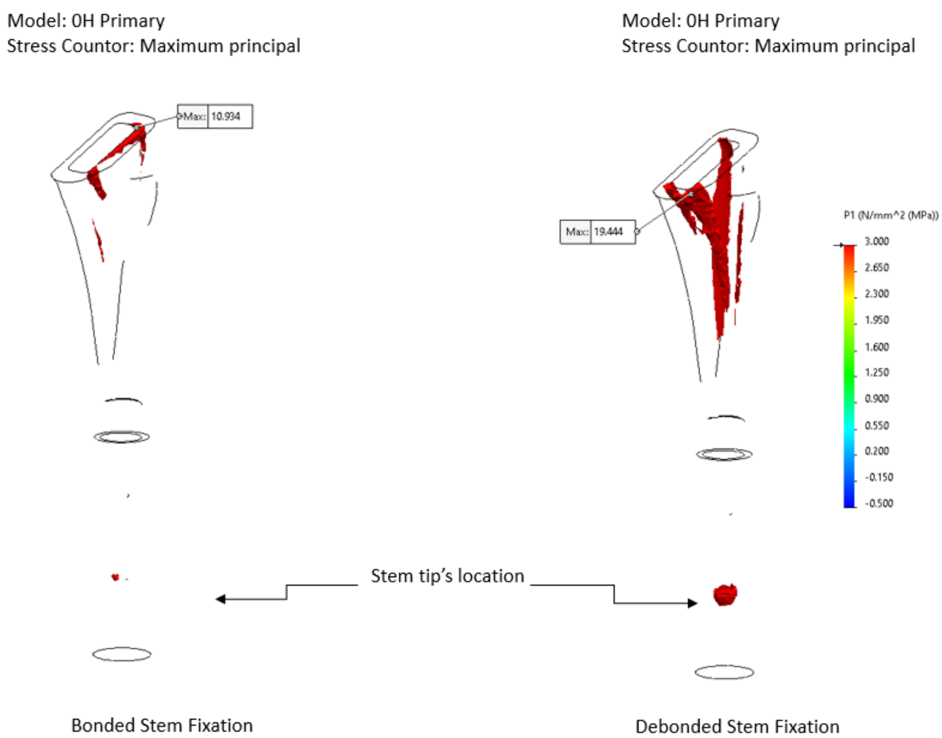

Figure 7.2 – Principal stress distributions above 3MPa acting in the mantle from the 0H primary THR model

The other parameter used to establish the comparisons between the outcomes from the two works was the direction of stresses in the mantle. Lennon and Prendergast (2001) have analyzed the orientation (longitudinal or hoop) of the tensile maximum principal stress vectors measured relatively to a longitudinal reference in the mantle of cement, aiming to predict the load behavior acting in the cement. In the 0H primary models, the longitudinal and hoop components of the normal stress acting in the mantle were plotted with respect to the stem's axis and used as a basis of comparison. The longitudinal components were found to be exerted thoroughly on the lateral side, when the bonded case of stem fixation was examined and, for the debonded configuration of the cement-stem contact, it was observed an increase in the longitudinal stresses in the cement surrounding the distal tip. Regarding the tensile hoop component plots, in this work, they were found to be irregularly distributed through the cement mantle for the bonded stem configuration, while for the debonded case of fixation it was observed an expressive increase in the regions experiencing the hoop stresses.

The hoop stress distributions deviate from what is described in Lennon and Prendergast (2001), where for the bonded configuration the hoop components were only found at the lateral side of the proximal section and at the posterior side of the middle section. However, those regions also increased in size with the debonded case of fixation. Therefore, in both works, there was an increase in the hoop stress components exerted in the cement mantle with the debonding behavior. Figure 7.3 displays the longitudinal tensile stress plots, and figure 7.4 contains the hoop tensile stress components.

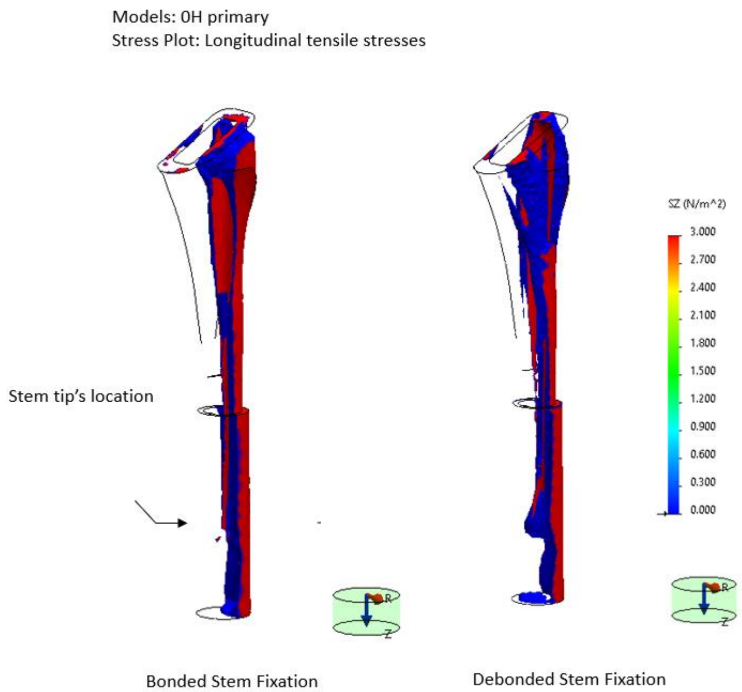

Figure 7.3 - Longitudinal tensile stresses

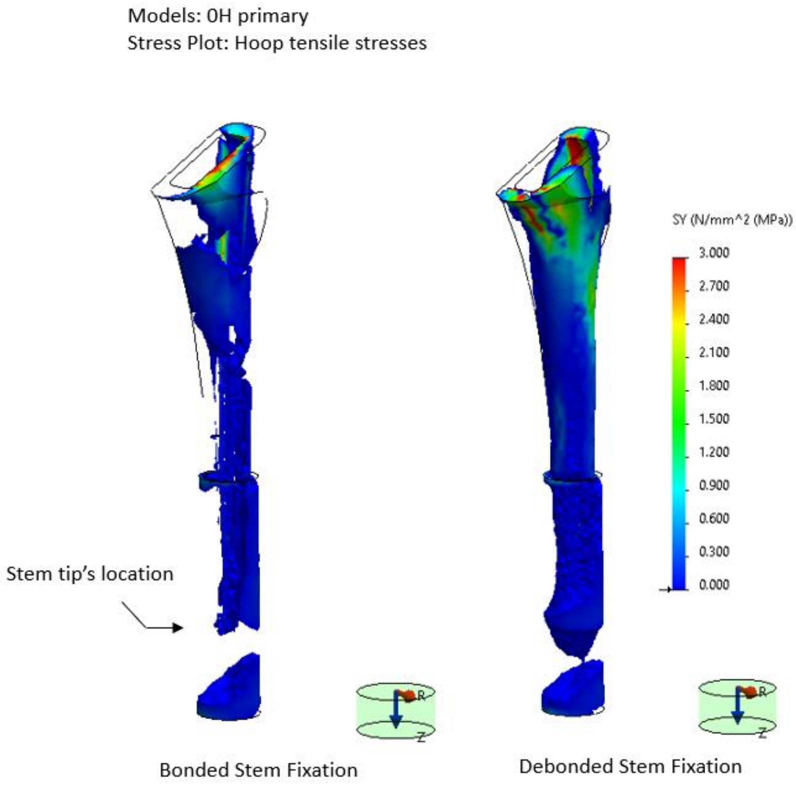

Figure 7.4 - Hoop tensile stresses

All the differences found between the two works' outcomes, regarding the maximum stress locations and some aspects of the stress distributions, could not surpass the similarities found in the contour of maximum principal stresses or the distributions of the hoop and longitudinal stresses, mainly because in both works all variations in the results that are related with the cement-stem contact configuration, were found to be the same. Moreover, the geometrical particularities of the cement mantle designed for this work might have influenced the location of peak stresses due to their strong dependency on the existence of regions that act as stress concentrators, or to the presence of mesh singularities. Likewise, the unique geometric features of the cement mantle designed for this work can be responsible for the way the stress distributions have presented some differences from what is observed in the stress plots in Lennon and Prendergast (2001). Therefore, it was possible to conclude that the THR models created for the present analysis are capable of providing physiologic-like results that would be able to translate the stress distributions in a moment of critical loading during walking.

Chapter 8 - The Stress Distributions in the Revision THR Models

The stress distributions in the THR models were obtained aiming at the comprehension of how the compressive and tensile stresses are distributed at a moment when the loading conditions at the proximal femur are critical in the primary and revision models. In this section, the effects of the type of cement-stem contact in the stress plots in the cement mantles, metallic stem, and cortical bone, from the primary and revision models will be presented. Regarding the revision models, the influence of the new mantle thickness in the stress distributions is going to be discussed, in this chapter. Moreover, it will be presented what were the observed differences between the stress plots when the models have the same design configuration except for the type of revision group they belong to.

8.1 Cement Mantles

PMMA bone-cements are brittle materials, therefore, when statically loaded, they tend to experience mechanical failure, when the compressive or tensile stresses exerted on them are superior to their compressive or tensile strengths. Hence, only normal stresses were considered for the analysis of the stress distributions in the cement mantles, where the observed stress plots were the principal stresses exerted on each of the mesh elements that describe those implant components. Aiming to evaluate how critical the loading profile employed in this work would be for the bone cement, a comparison was made between the PMMA compressive and tensile strengths values, presented in chapter 4, with the highest stress moduli in the plots. The tensile stresses were studied using the plots of the maximum principal stresses, because they are equivalent to the highest values of the principal stresses' components, while the compressive stresses were evaluated through the minimum principal stresses, the lowest values of the principal stresses' components.

To describe the stress contours in this section, the regions of all the mantles are referred accordingly the same classification system used in Lennon and Prendergast (2001), where the mantles are divided into proximal, middle, and distal sections which are separated from each other by transverse planes to the femoral stem axis. Moreover, each of the mantle's cross-sections got divided into medial, lateral, posterior, and anterior regions.

8.1.1 – 1H and 0H primary THR models

Regarding the maximum principal stress plots, it was found that the contours of tensile stresses have been found to not significantly change between the mantles of the 1H and 0H primary THR models. With the bonded cement-stem interface, the most considerable volume concentrations of cement under high tensile stresses, in both primary models, were found to be located next to the interior faces of the mantle at the anterior side in the upper part of the proximal sections, at the lateral-posterior and medial-posterior sides in the proximal section, and medially and posteriorly around the stem tip (see figure 8.1). For the debonded configurations, as shown in figure 8.2, the interior faces of the mantle and their neighbor regions have exhibited more expressive concentrations of cement volumes under the highest tensile stresses, being predominantly localized at the medial side of the upper part of the proximal mantles section, at the lateral-posterior and medial-anterior sides at the proximal section, at the lateral side at the proximal and distal sections, and in the distal section around the stem's distal tip. The increase in the size of the regions under the highest tensile stresses at the cement-stem interface was an expected consequence of the existing friction between the stem and the mantle.

Relatively to the compressive stresses acting in those mantles, the influence of the differences in design characteristics on the stress contours was also observed to be mainly negligible. In the models with the debonded cement-stem configuration, the regions under the compressive stresses with the highest moduli (lowest values) were found to be larger, when compared with the models with the bonded stem. For the debonded configurations, see figure 8.3, the lowest compressive stresses were found to be located at the medial side at the upper part of the proximal section, around and below the stem tip at the distal section, and in the lateral-anterior lateral-posterior sides of the interior faces of the mantle at the proximal and middle sections. The models with perfectly bonded stems, as presented in figure 8.4, have shown the lowest compressive stresses distributed at the medial side of the proximal section in a similar size as what is observed in the debonded stem models, and in reduced size regions around and below the stem tip. From figure 8.1 to 8.4, the anterior and posterior sides of the mantles are displayed through a sectional view with respect to the medial-lateral plane.

In conclusion, for both compressive and tensile stress plots, the regions under higher stress moduli are bigger in the primary THR models with debonded stems. Moreover, it was in the 0H model with the debonded stem where the peak tensile stress has reached the highest value, while in the 1H model with the debonded stem the compressive stresses have reached the highest value, however, both were found to be inferior to the lowest ultimate strengths' values (32 MPa for the tensile strengths and equal to 80 MPa for the compressive strengths) indicated in Weeb and Spencer (2007). As shown in figure 8.1, the highest peak tensile stress was found in the mantle of the 0H primary THR model for the case of debonded cement-stem fixation, with a modulus of 19,44 MPa. While the highest peak compressive stress has a 58,16 MPa modulus its region of application is shown in the model with a debonded stem in the 1H primary THR model (see figure 8.3). Therefore, none of the peak stresses in the mantles indicate that brittle fracture might occur, at an instant of critical loading during walking.

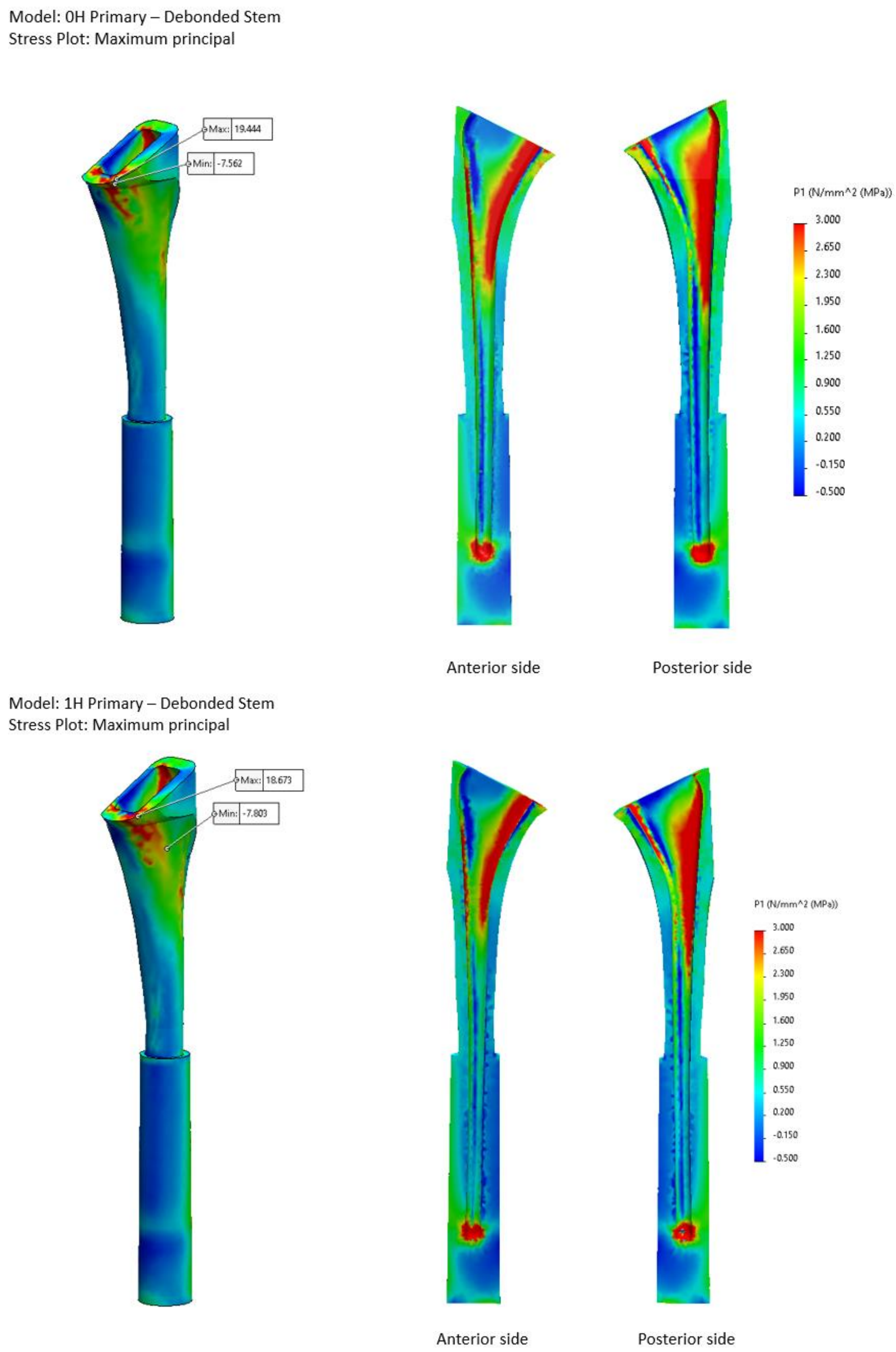

Figure 8.1- Maximum principal stresses in MPa exerted in the mantles of the primary THR models for the debonded case of stem fixation

Model: 0H Primary – Bonded Stem
Stress Plot: Maximum principal

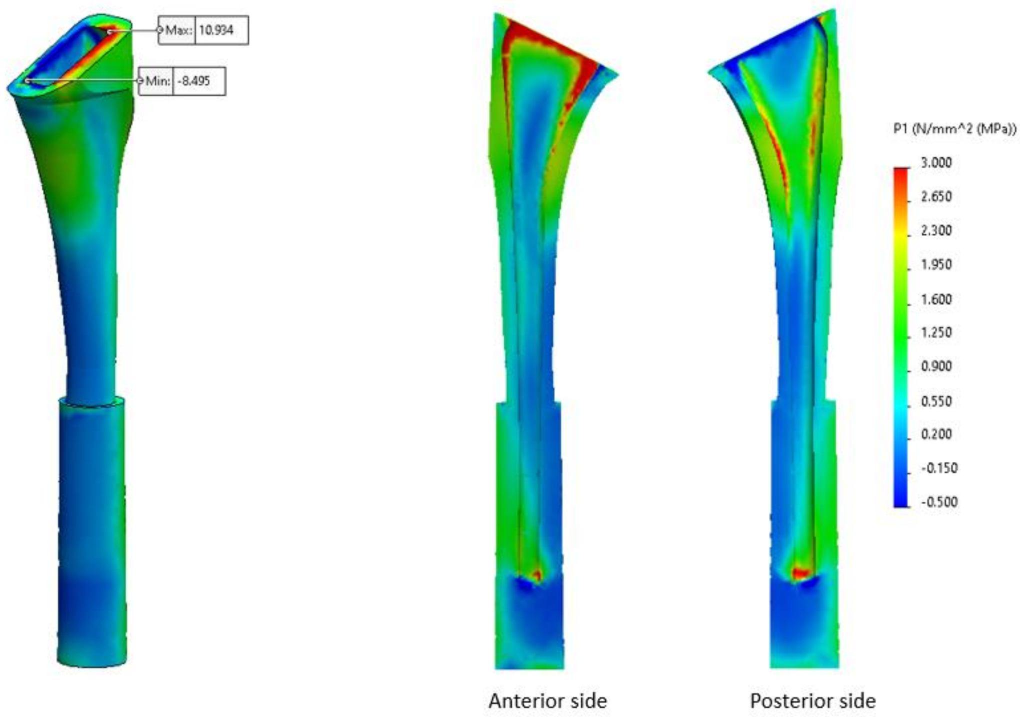

Model: 1H Primary – Bonded Stem
Stress Plot: Maximum principal

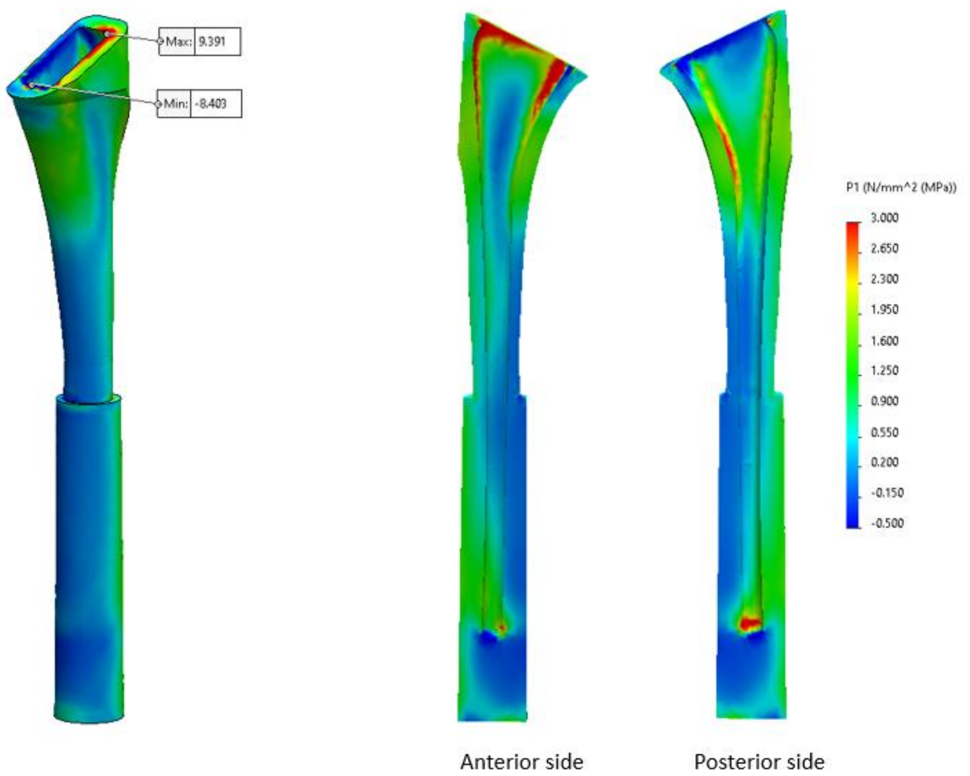

Figure 8.2 - Maximum principal stresses in MPa exerted in the mantles of the primary THR models for the bonded case of stem fixation

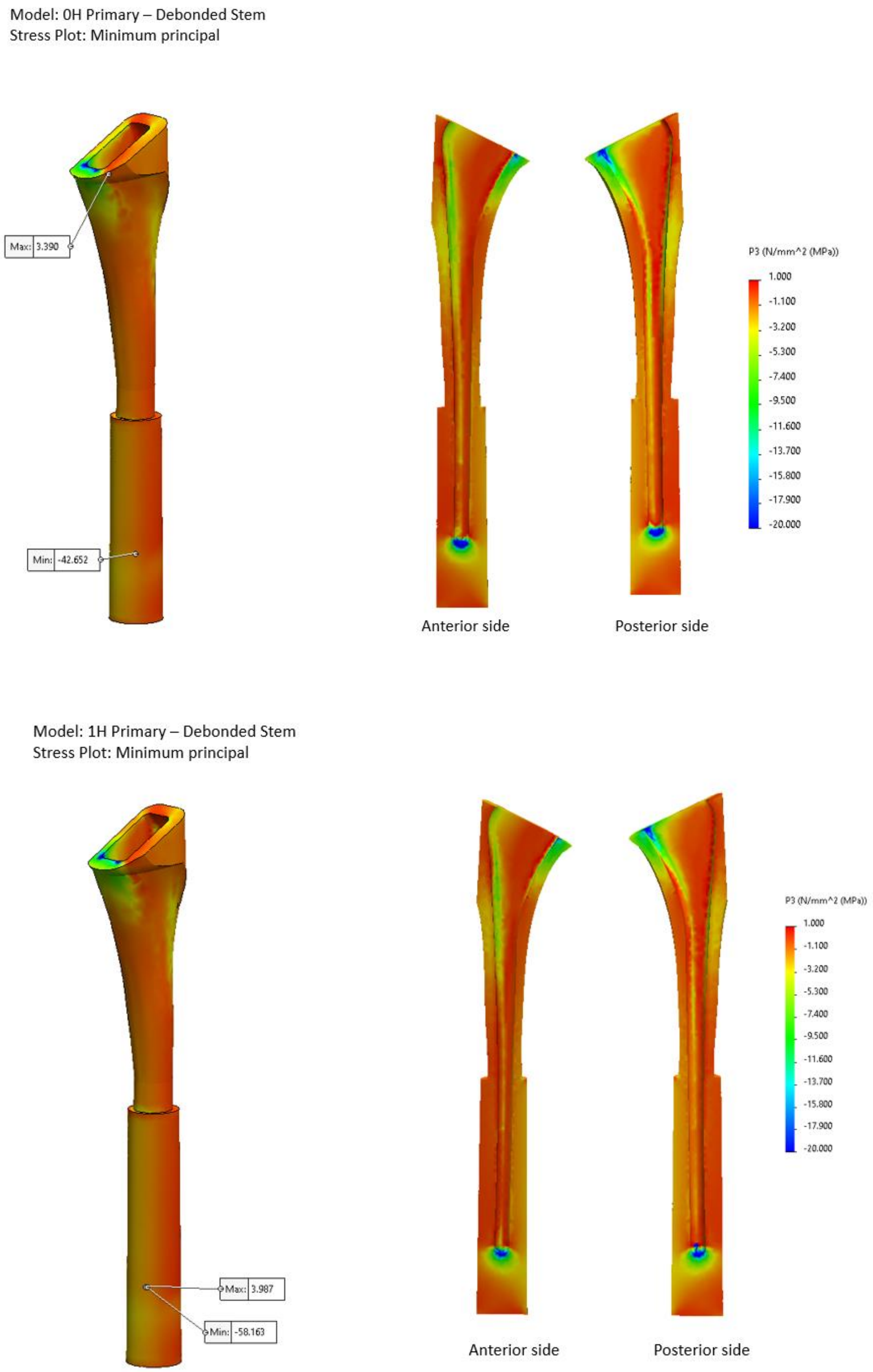

Figure 8.3 – Minimum principal stresses in MPa exerted in the mantles of the primary THR models for the debonded case of stem fixation

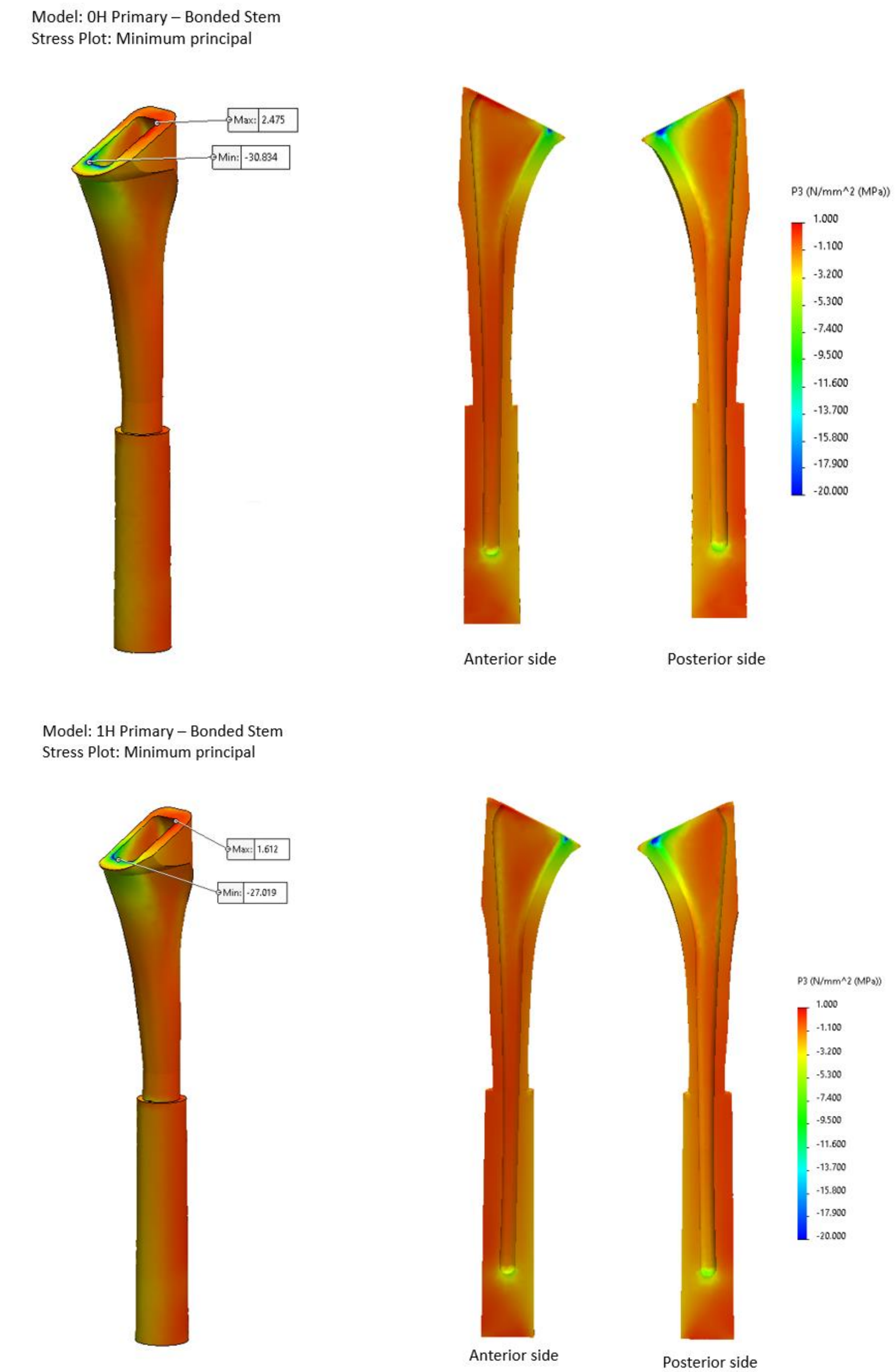

Figure 8.4 - Minimum principal stresses in MPa exerted in the mantles of the primary THR models for the bonded case of stem fixation

8.1.2 – Revision THR Models

As for the primary models, the tensile and compressive stresses acting in the new and well-fixed mantles from the revision THR models were studied considering the maximum principal and minimum principal stress plots, respectively. Moreover, it was also for the debonded configurations of the stem fixation where the regions with the highest stress moduli were found to be bigger, and where the peak stresses reached the highest values (20,12 MPa for the tensile, and 42,46 MPa for the compressive stresses). The determined peak stresses were also inferior to the ultimate strengths of the PMMA and indicate that the brittle failure wouldn't occur due to the critical loading profile that was considered in this work. Furthermore, all the examinations of the stress distributions in the mantles from the revision models were conducted separately for the new and well-fixed mantles and, to describe their stress contours, the regions in the well-fixed and new mantles were also defined accordingly the same classification system used in Lennon and Prendergast (2001)

It was observed that for the bonded and debonded cement-stem interfacial configurations, the stress distributions did not expressively change with the variations in new mantles' thicknesses within each of the revision THR groups. In figures 8.5 and 8.6 are shown, respectively, the plots of the maximum and minimum principal stresses acting in the new and well-fixed mantles in all the models from the 1H/0H and 0H/0H revision groups, for the debonded cement-stem contact, where below each model, the value of the new cement mantle thickness around the stem is indicated. Therefore, the stress plots obtained in the simulations of the models with new mantles with 1,2 mm thicknesses of cement around the stem were chosen to illustrate all the following o**bservations about the main characteristics of the contour of stresses in all the mantles, and the comparisons between the stress plots from the 0H/0H and 1H/0H designs**.

Models: 0H/0H Revision – Debonded Stem
Stress Plot: Maximum principal

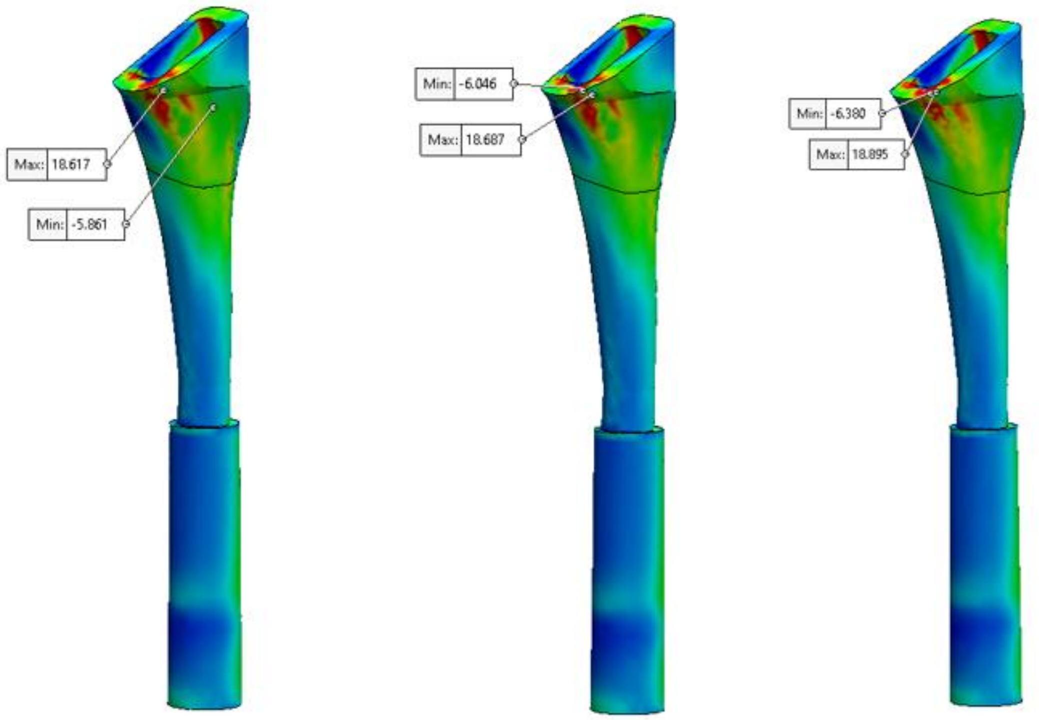

0,8 mm　　1,2 mm　　1,6 mm

Models: 1H/0H Revision – Debonded Stem
Stress Plot: Maximum principal

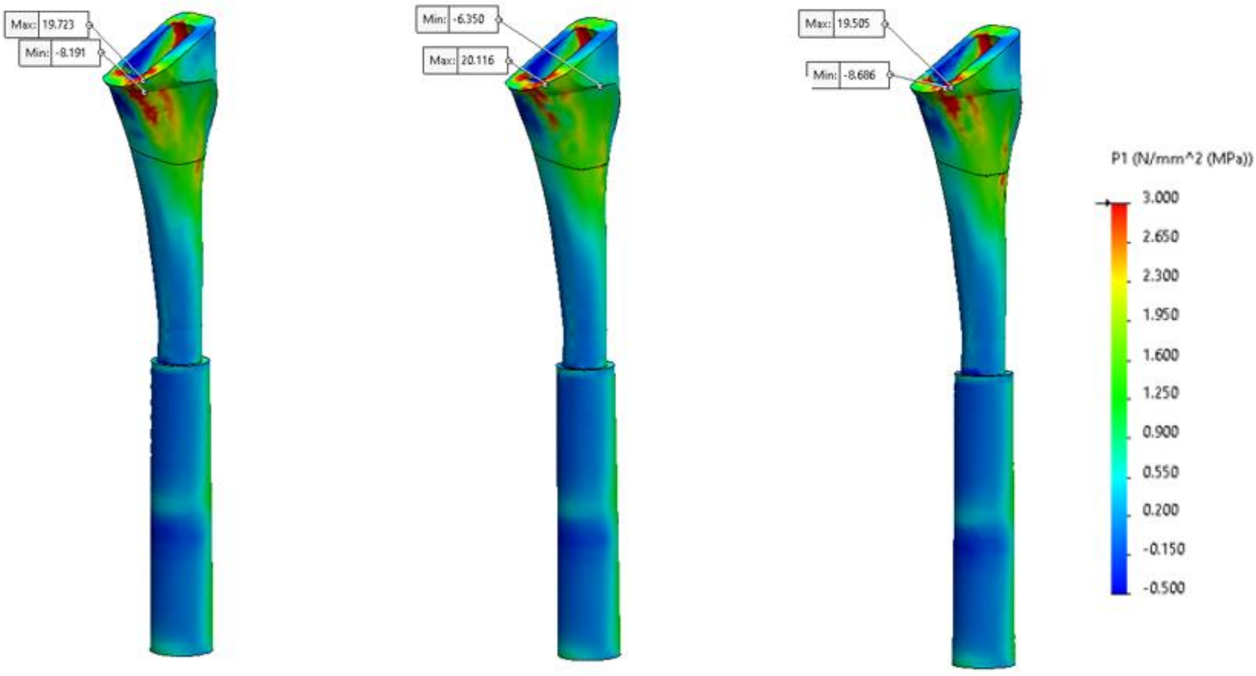

0,8 mm　　1,2 mm　　1,6 mm

Figure 8.5 - Maximum principal stresses in MPa acting in the well-fixed and new mantles from the 0H/0H and 1H/0H revision THR groups for the debonded cement-stem contact

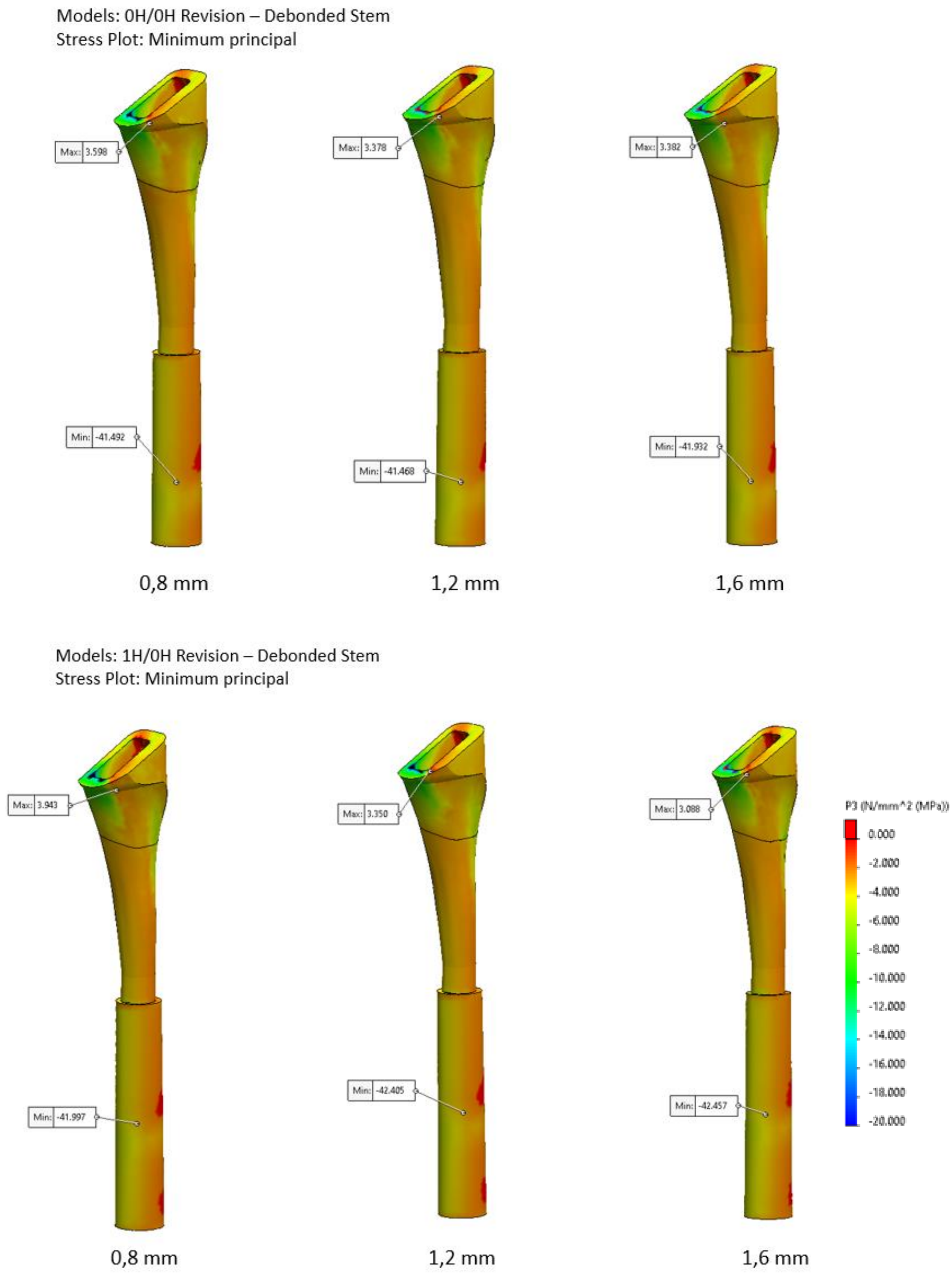

Figure 8.6 - Minimum principal stresses in MPa acting in the well-fixed and new mantles from the 0H/0H and 1H/0H revision THR groups for the debonded cement-stem contact

The highest tensile stresses in the new mantles are mainly located at the external surfaces contacting the well-fixed mantle, and at the interior surfaces contacting the stem, as well as their adjacent regions. For the debonded stem configuration, these stresses are mainly concentrated at the lateral-posterior and medial-anterior sides in the proximal section, around the distal tip, and at the medial side in the upper part of the proximal section; while for the bonded stem configuration, there are reduced regions that experience the highest stresses, which are located at the anterior side in the upper part of the proximal section, at the medial-posterior side in the proximal section, and at the posterior and medial-anterior sides next to the distal tip.

Regarding the tensile stresses in the well-fixed mantles, as well as for the new mantles, it was at their interfaces and in its neighboring regions, where the highest stresses were found to be concentrated. In the old mantles from models with debonded stem configuration, it was observed that the highest stresses are located at the lateral-anterior side in the upper part at the proximal section, and in the lateral sides around the stem's tip; while for the bonded stem configuration, it was found that the highest stress regions are replaced by medium stress regions. Figure 8.7 contains representations of the maximum principal stress plots of the new and well-fixed mantles from the 0H/0H and 1H/0H models with 1,2 mm mantle thicknesses, for the two cases of stem fixation. Figures 8.8 and 8.9 display the contour of stresses in the anterior and posterior sides of the new and old cement mantles, which are displayed in a sectional view with respect to the medial-lateral plane, with the sides of the mantle with a thickness of 1,2 mm in the left and the sides of the well-fixed mantle in the right.

Comparing the maximum principal stress plots of the 1H/0H models with the ones from the 0H/0H models, it was observed that the differences in the contour of tensile stresses are inexpressive. The most significant variation in the stress distributions regarded the highest stress distributions in the well-fixed mantles for the debonded cement-stem interface configuration. As shown in figure 8.8, for the 1H/0H model, the region under the highest stresses is found predominantly in the upper part at the posterior side of the older mantle, while in the 0H/0H model the high stresses can also be seen more expressively distributed around the stem's tip.

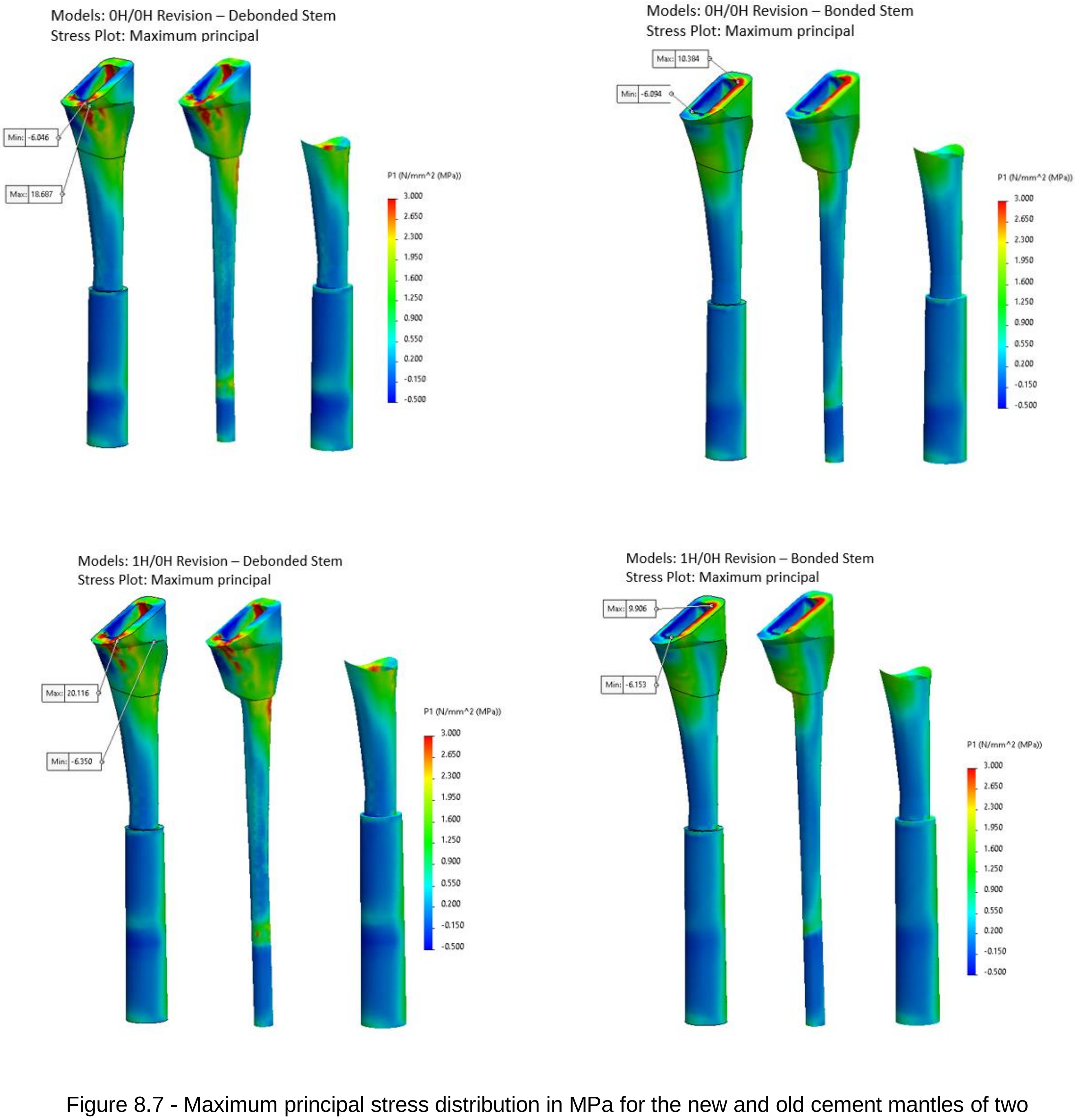

Figure 8.7 - Maximum principal stress distribution in MPa for the new and old cement mantles of two revision THR models for both cases of cement-stem contact

Models: 0H/0H Revision – Debonded Stem
Stress Plot: Maximum principal

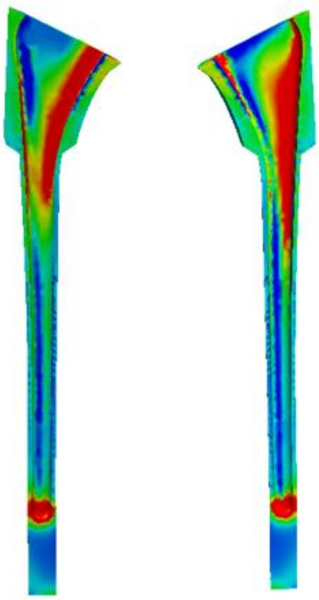

Anterior side Posterior side

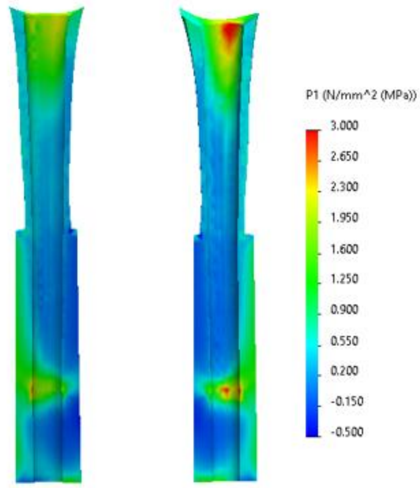

Anterior side Posterior side

Models: 1H/0H Revision – Debonded Stem
Stress Plot: Maximum principal

Anterior side Posterior side

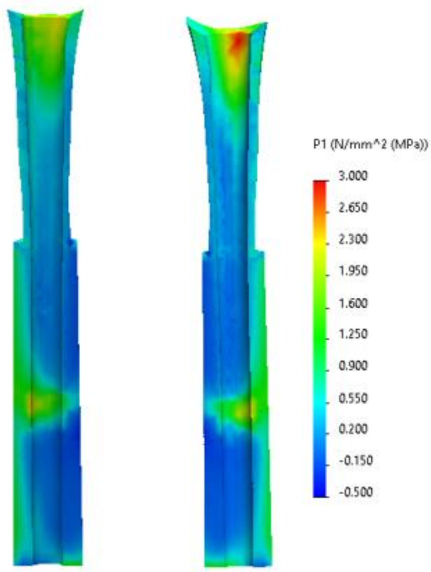

Anterior side Posterior side

Figure 8.8 - Maximum principal stresses in MPa exerted in the mantles of a revision THR model for the debonded case of stem fixation

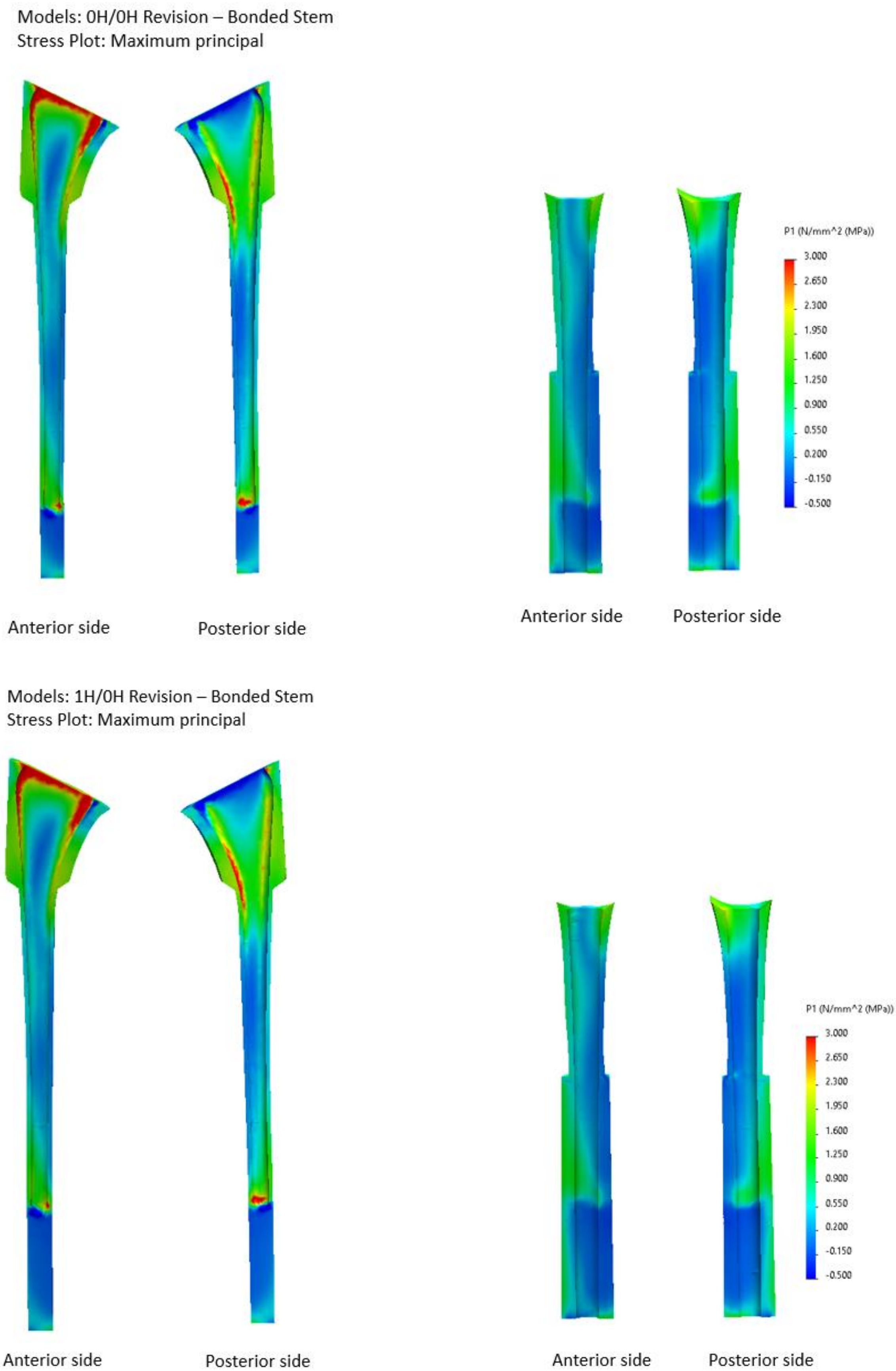

Figure 8.9 - Maximum principal stresses in MPa exerted in the mantles of a revision THR model for the bonded case of stem fixation

The regions under the lowest compressive stresses in the new mantles are also bigger in the models with debonded stem configuration being placed at the medial side in the upper part of the proximal section and at the regions around, at the lateral-anterior and lateral-posterior sides of the mantle at the proximal section, and around and immediately below the stem’s tip, while in the bonded configuration the lowest stresses are located at the medial side in the proximal section, and in reduced size regions around and below the stem tip. Relatively to the old mantles, the compressive stress levels were found to not reach the highest moduli observed in the newer mantles, and the lowest compressive stresses in their plots are around the medium values represented in the stress scale, being located around the stem’s tip and at the lateral side in the proximal region when the cement-stem interface is debonded, and only around the stem’s tip for the bonded cement-stem interface. In Figure 8.10, are represented the minimum principal stress plots of the new and well-fixed mantles from the 0H/0H and 1H/0H models with 1,2 mm mantle thicknesses, for the bonded and debonded cases of stem fixation. While in figures 8.11 and 8.12, those contours of stresses, in the anterior and posterior sides of the new and old mantles, are shown in a sectional view with respect to the medial-lateral plane. On the left are represented the posterior and anterior sides of the new mantle with 1,2 mm of thickness, and on the right are represented the same sides of the well-fixed mantle.

It was also mainly for the well-fixed mantles that the minimum principal stress plots have shown substantial differences between the 0H/0H and 1H/0H revision models, where, for both bonded and debonded cement-stem configurations, more regions were found to be under the lowest compressive stresses, being located below the level of the stem’s tip in the 1H/0H models.

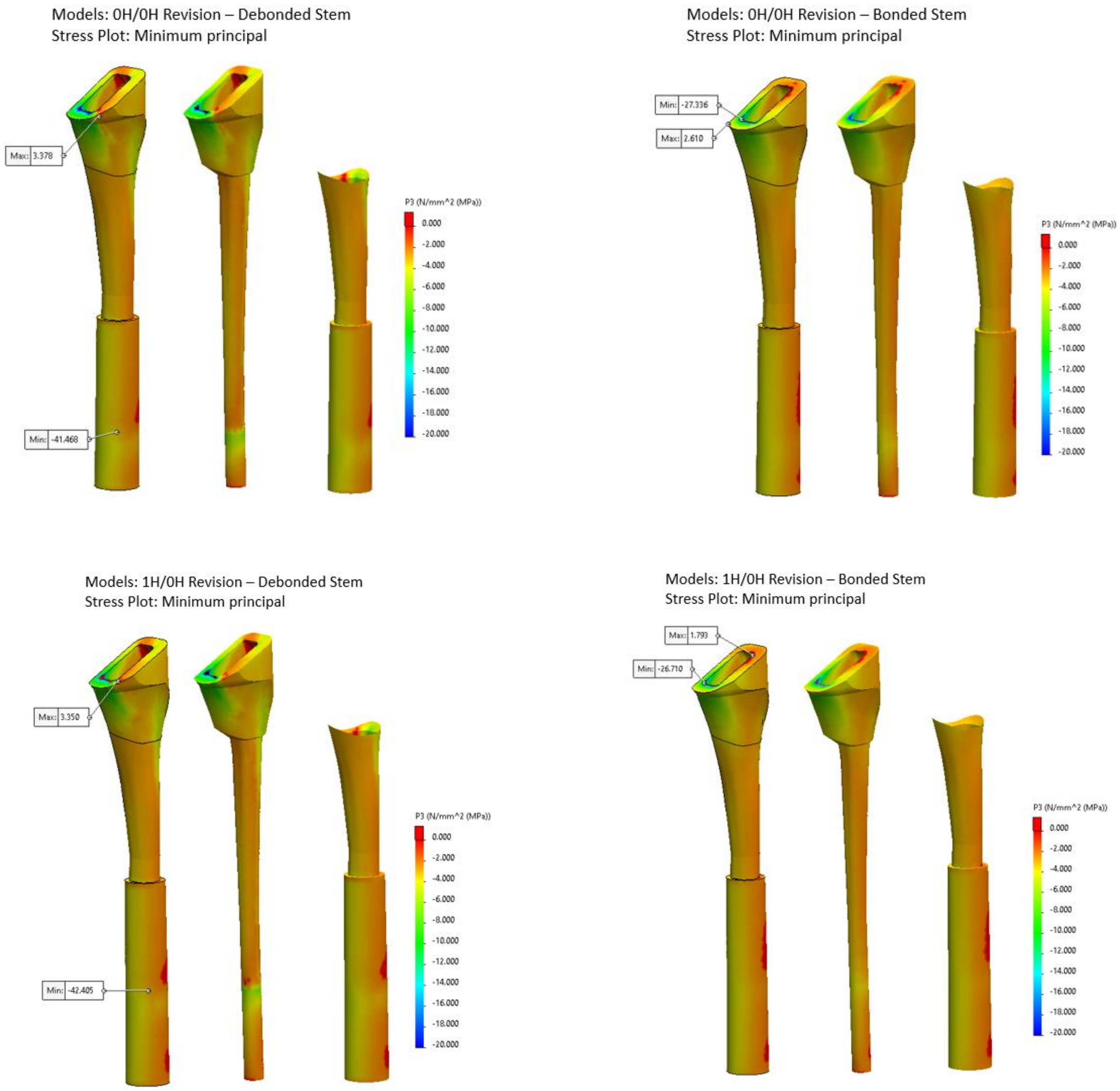

Figure 8.10 - Minimum principal stress in MPa plots for the new and old cement mantles of two revision THR models for both cases of cement-stem contact

Models: 0H/0H Revision – Debonded Stem
Stress Plot: Minimum principal

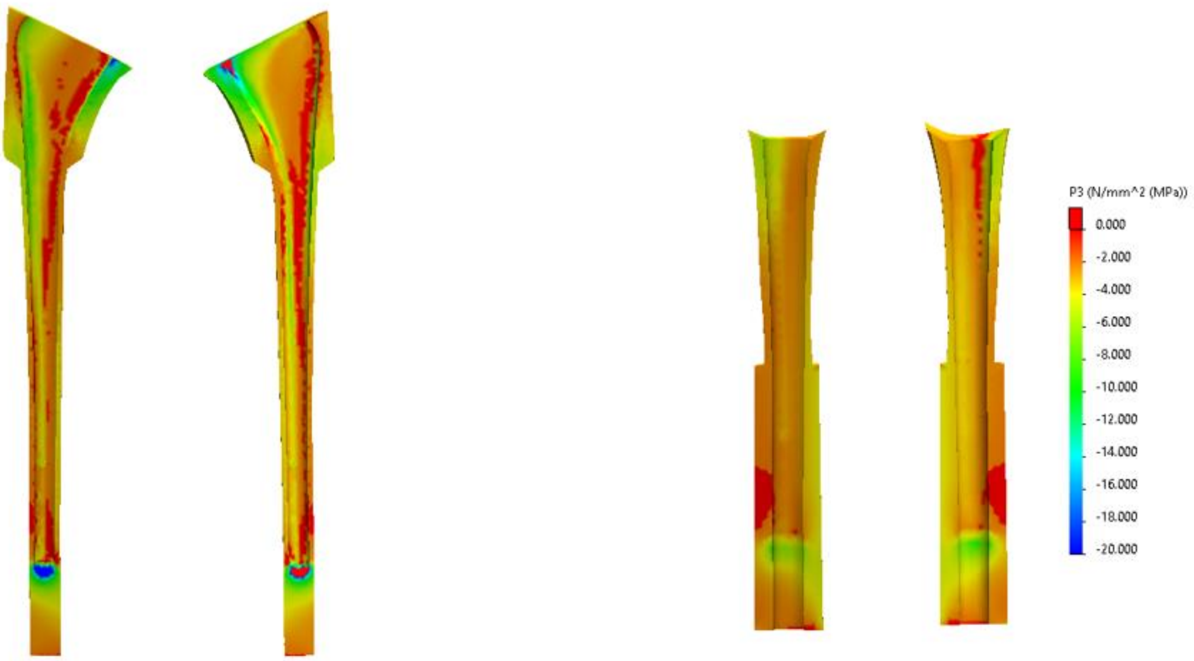

Models: 1H/0H Revision – Debonded Stem
Stress Plot: Minimum principal

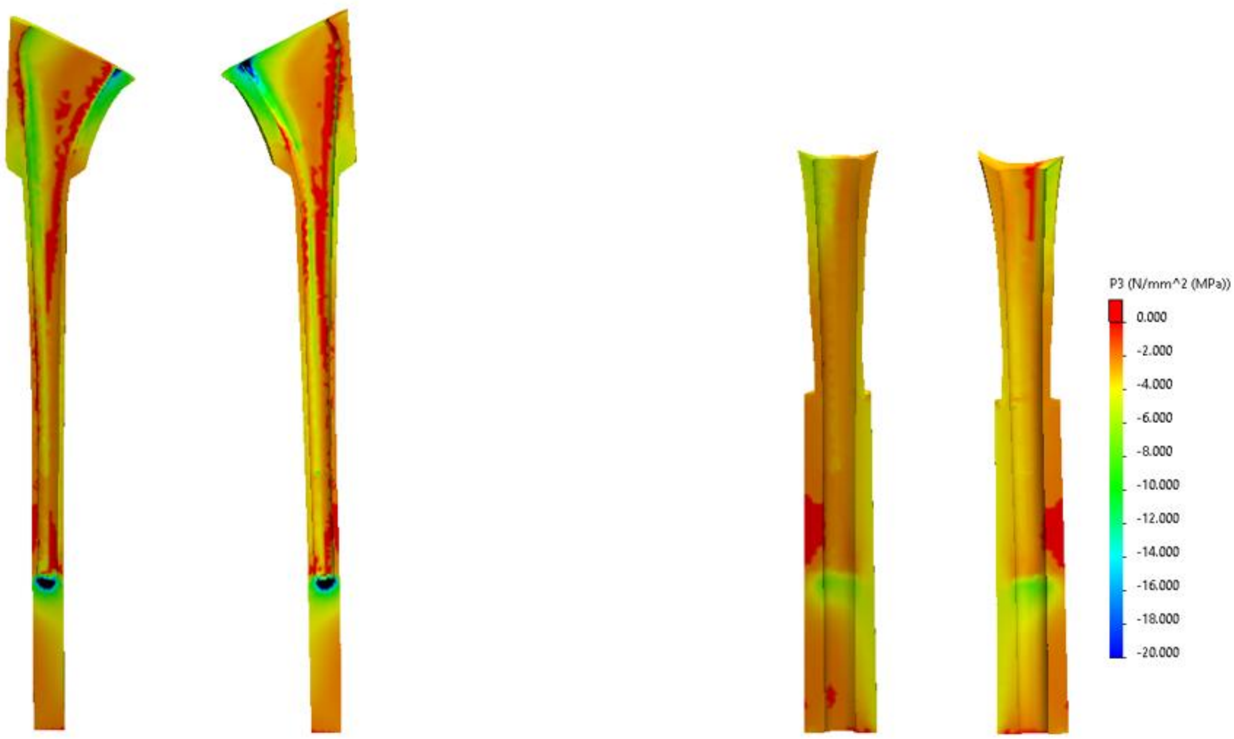

Figure 8.11 - Minimum principal stresses in MPa exerted in the mantles of a revision THR model for the debonded case of stem fixation

Models: 0H/0H Revision – Bonded Stem
Stress Plot: Minimum principal

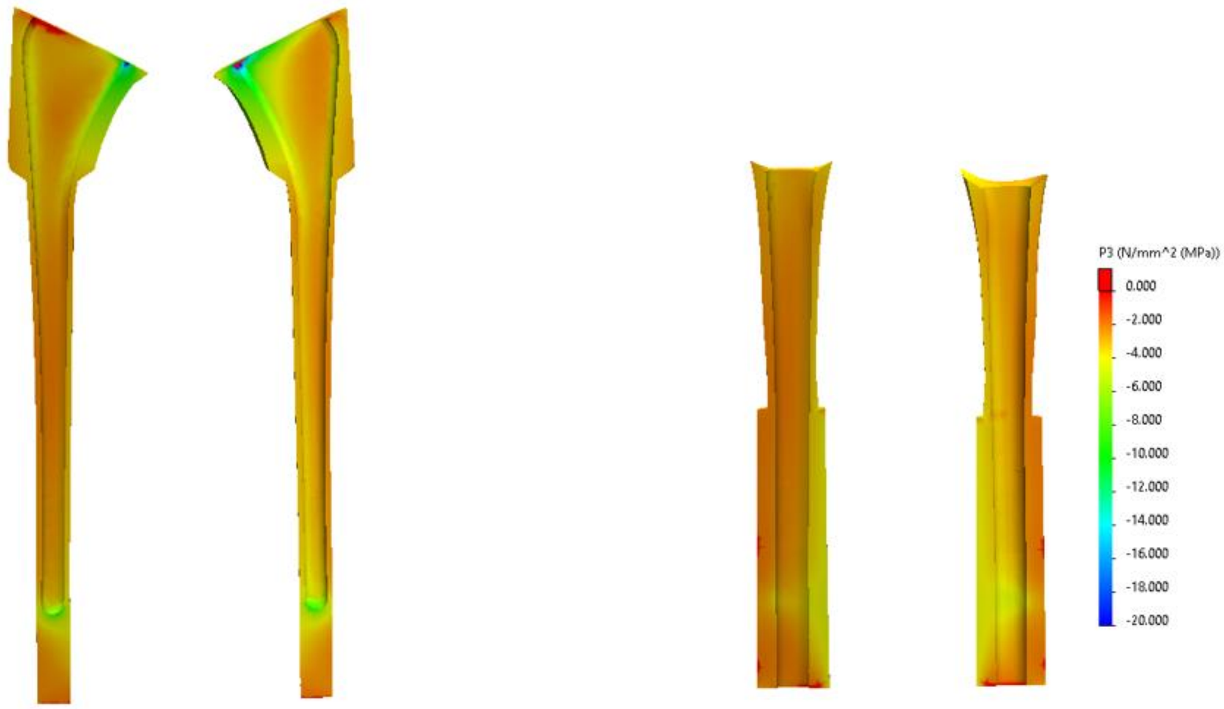

Models: 1H/0H Revision – Bonded Stem
Stress Plot: Minimum principal

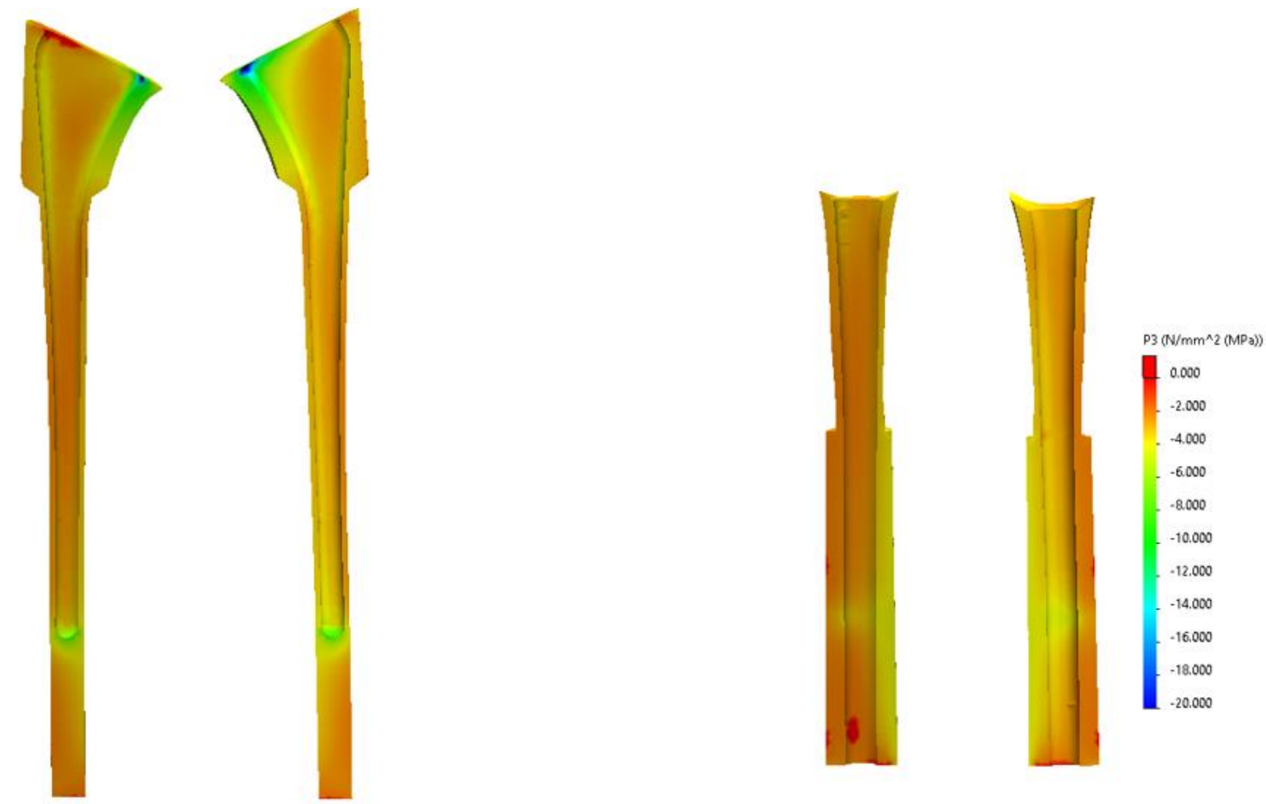

Figure 8.12 - Minimum principal stresses in MPa exerted in the mantles of a revision THR model for the bonded case of stem fixation

8.2 Metallic Prostheses

Von Mises Stress plots were used in the study of the contour of stresses in the stainless-steel prosthesis because of their application in the Von Mises criterion of failure, which is used for such ductile materials. In the plots of all the models, for the bonded and debonded stem configurations, the peak stresses were found to be located at the stem neck and, to be approximately equal to 255 MPa in the 0H models, and equal to 230 MPa in the 1H models. Through the comparison of those stress values with the poof strengths provided in manuals from suppliers of stainless-steel alloys for medical applications, it became clear that the Yield Stress wouldn't be surpassed and, thus, the prosthesis wouldn't experience ductile failure. For instance, the F1586 stainless steels for medical applications with the lowest proof strengths commercialized by Sandvik® are supplied as annealed bars with proof strengths equal to 107 ksi or 738 MPa, therefore, this material's smallest strength is around three times the value of the peak stresses found in the models.

Furthermore, the contour of stresses was found to be similar in all THR models, with the highest stresses being located at the stem's neck for all cement-stem contact configurations, and at the medial-posterior side in the middle sections for the stems from models with debonded cases of fixation. However, it was observed that for the debonded case of fixation there is an increase in the stress levels acting in the stems and that the 1H stem has higher stress levels for both cases of stem fixation. Moreover, the regions under medium stresses were found to be considerably large, being exerted throughout the medial side, at the lateral side in the middle section, and around the stem's neck. It can be observed in figures 8.13 and 8.14 how the regions under high stresses increase at the middle sections, as well as the regions under medium stresses increase in size at the anterior side in the proximal section, and at the lateral side in the middle section, for both 0H and 1H primary models, from the bonded to the debonded cement-stem configuration.

All 0H stems used in the revision models have essentially the same stress contours as in the primary surgery models. As well, the variation of the thickness in the mantle's designs essentially has not affected the way the Von Mises stresses got distributed in the stems. In figure 8.15, is indicated the influence of the new mantle thickness in the stress plots of the stems with debonded fixation from the 0H/0H and 1H/0H models, where the small variations in the contour of stresses are evident.

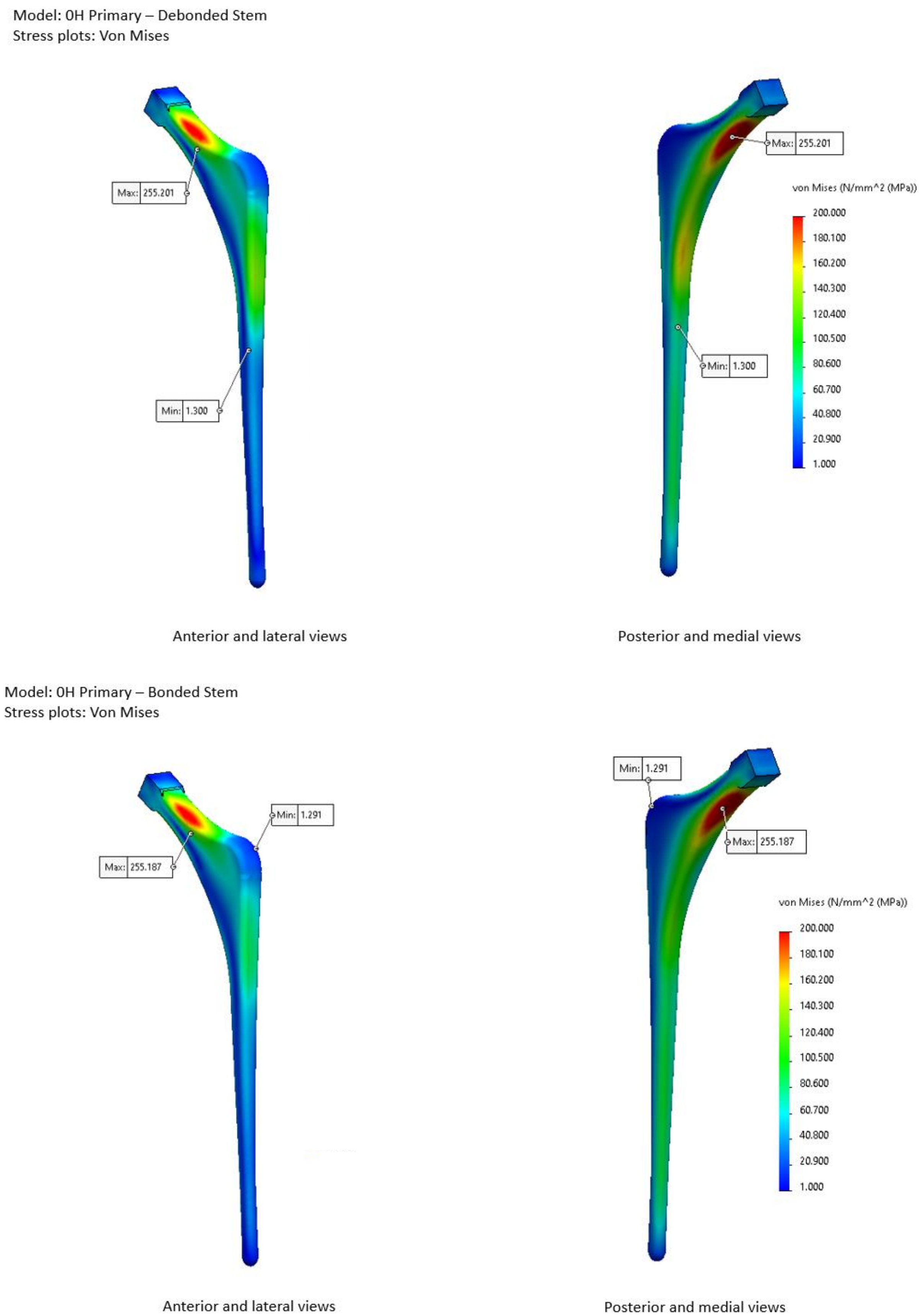

Figure 8.13 – von Mises stresses in MPa exerted in the stem of the primary THR model for the debonded and bonded case of stem fixation

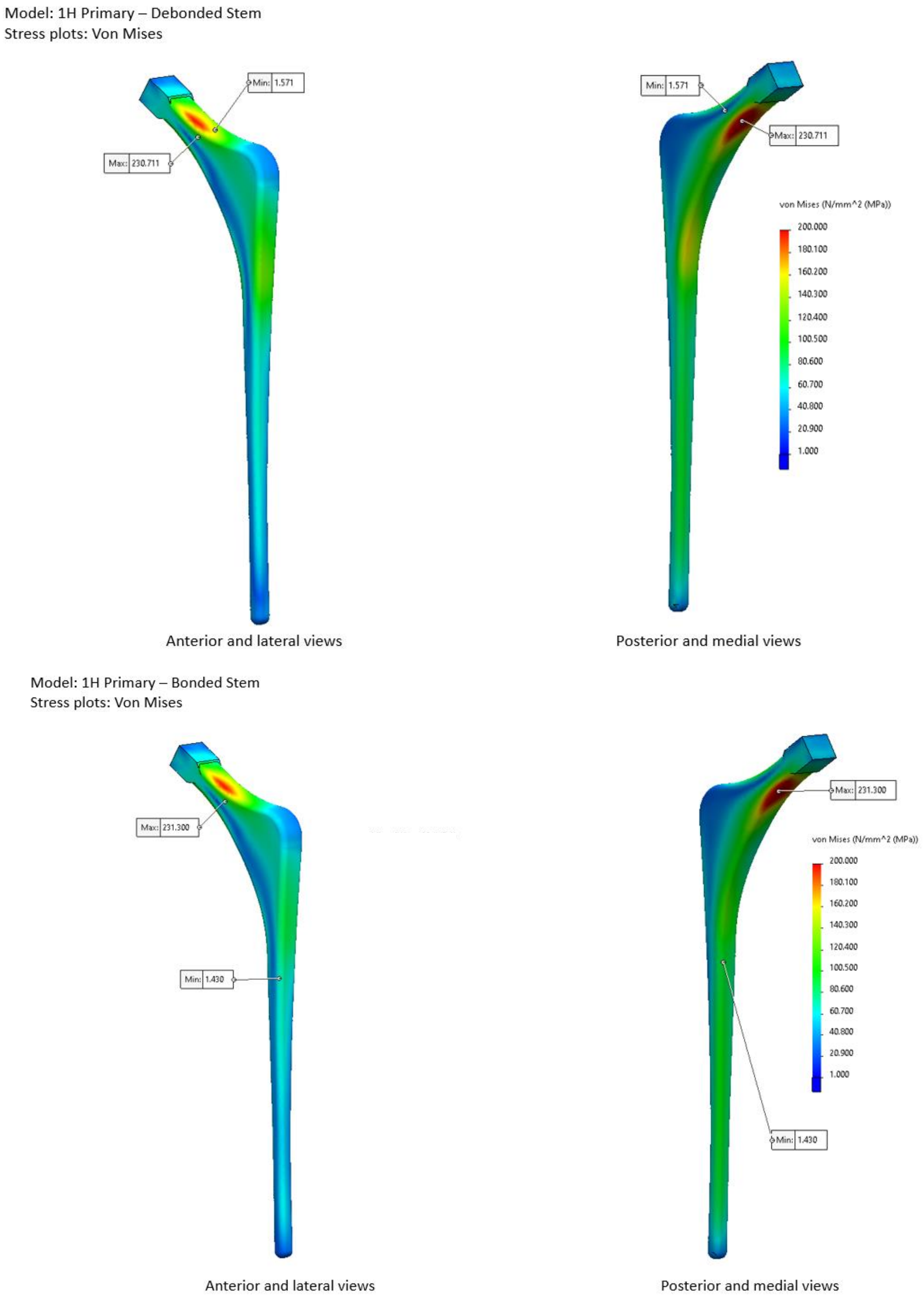

Figure 8.14 - von Mises stresses in MPa exerted in the stem of the primary THR model for the debonded and bonded case of stem fixation

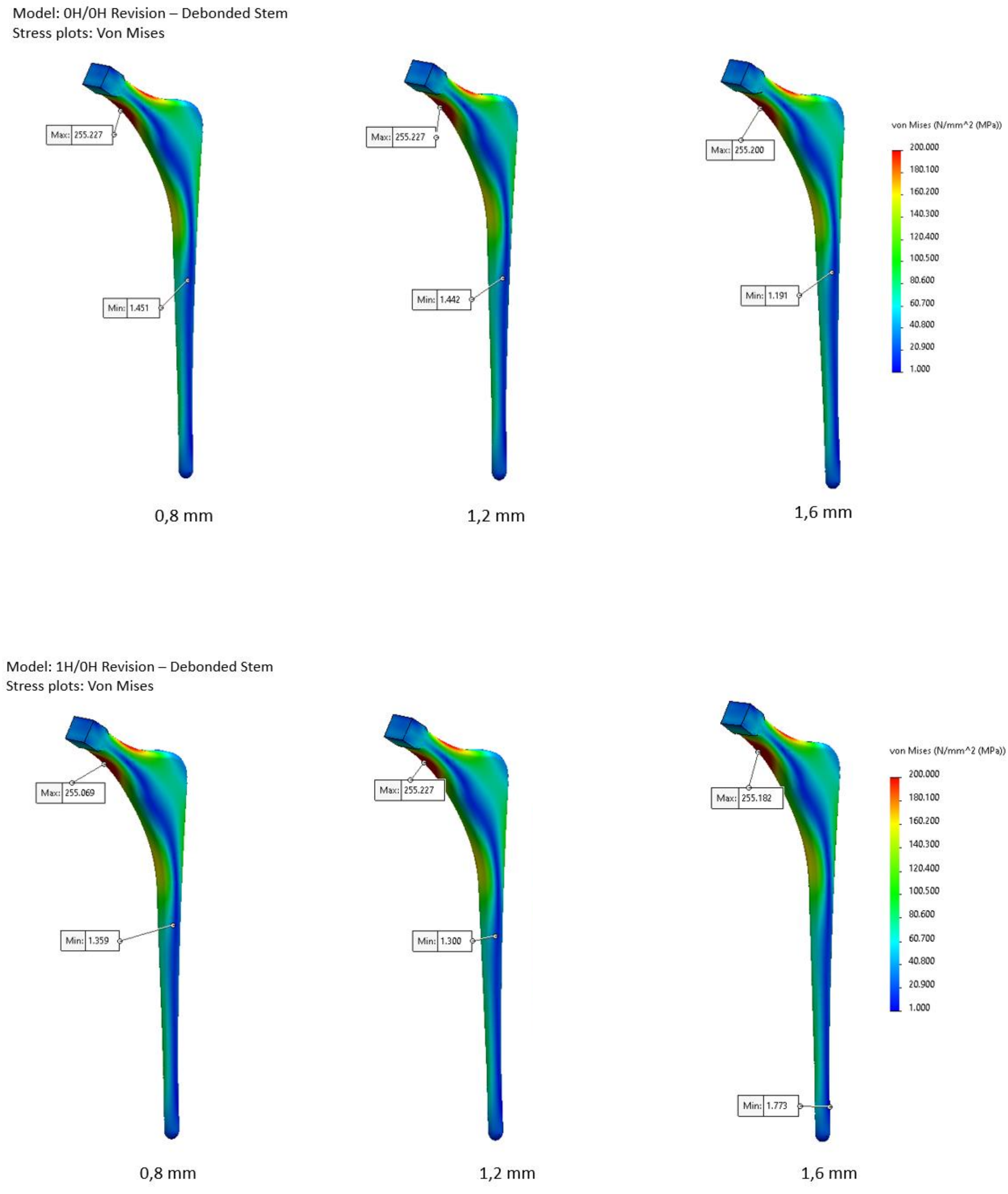

Figure 8.15 - von Mises stresses in MPa exerted in the stem of the revision THR models for the debonded case of stem fixation

8.3 Cortical Bone

A detailed examination of the longitudinal and transverse stresses acting in the bony tissues was not among the main objectives of this work and, hence, aiming to simplify the models' configurations, not only the trabecular but also the cortical bones were considered to have isotropic material properties. Consequently, the stress distributions in the femur bone model would deviate from what would be expected for studies that account for the materials' anisotropy. Therefore, comparisons between the peak principal stresses exerted on the 3D models with the mechanical properties of the femur bone, such as the ultimate compressive and tensile strengths of the cortical femur bone shown in chapter 3, were not included in this work. However, the study of the contour of stresses in the cortical bone was executed to compare the stress distributions in the bones from the THR models with the ones found for a natural femur bone model, when these structures are under the effect of the same critical loading profile, aiming to observe how the different implant configurations could influence in the stress shielding. The stress types used for the analyses were the maximum and minimum principal stresses, following Oshkour et al. (2015), where the maximum principal stresses were used to study the tensile stress components and the minimum principal to study the compressive components.

The contours of stresses have shown essentially the same characteristics in all the simplified cortical bone components from the THR models. The maximum principal tensile stresses reached their highest moduli mainly at the lateral side in the middle and distal sections of the cortical bone, and at the nearest regions around the points of muscular force application (P1 and P2). Medium tensile stresses are distributed in some regions at the medial, at the posterior and anterior sides above the level of the lesser trochanter, and majorly at adjacent regions next to the highest stresses at the anterior and posterior sides. Regarding the compressive stresses, their highest levels were found to be exerted at the medial side below the level of the lesser trochanter, and next to the points P1 and P2, while the medium compressive stresses were found to be predominantly exerted in neighbor regions to the highest compressive stresses, and at the posterior and lateral sides above the level of the lesser trochanter.

The not operated femur model that was prepared to simulate the effects of the same gait loading profile in the contour of the stresses was designed with a resection cut at the same position as in the models from the 0H/0H revision groups. The compressive and tensile stress plots that were obtained for this natural femur model have essentially the same contours below the level of the femoral cut which was modeled for the analyses of the THR models, with only a few observable alterations. A noticeable increase in the medium tensile stresses in the THR models, at the posterior and medial sides at the level of the lesser trochanter, was verified. Medium level maximum principal stresses were also found in the plane surfaces that have resulted from the femoral cuts. Moreover, the highest compressive stresses at the medial side at the level of the lesser trochanter were replaced by medium and low compressive stresses in the THR models, and the low compressive stresses were replaced by medium stresses at the posterior side in the lesser trochanter. Figures 8.16 and 8.17 illustrate these alterations by displaying, respectively, the maximum and the minimum principal stress plots in both the natural femur bone model, and in the 0H primary THR model w

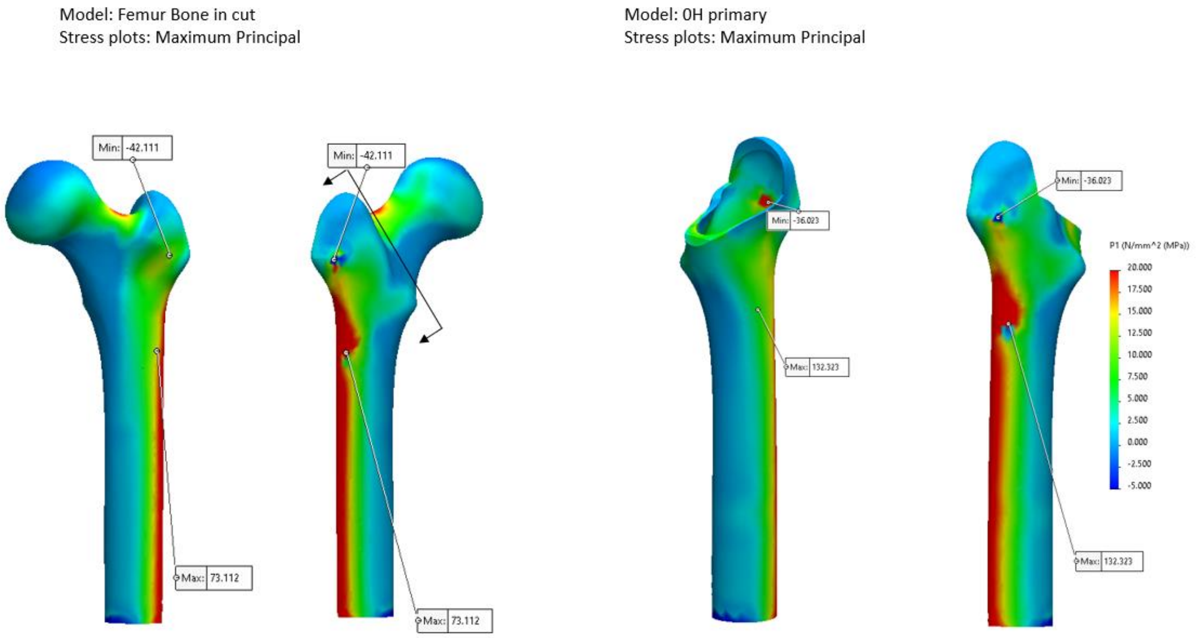

Figure 8.16 - Maximum principal stresses in MPa acting in the natural femur bone model and in the cortical bone models from the 0H primary THR model with a debonded stem

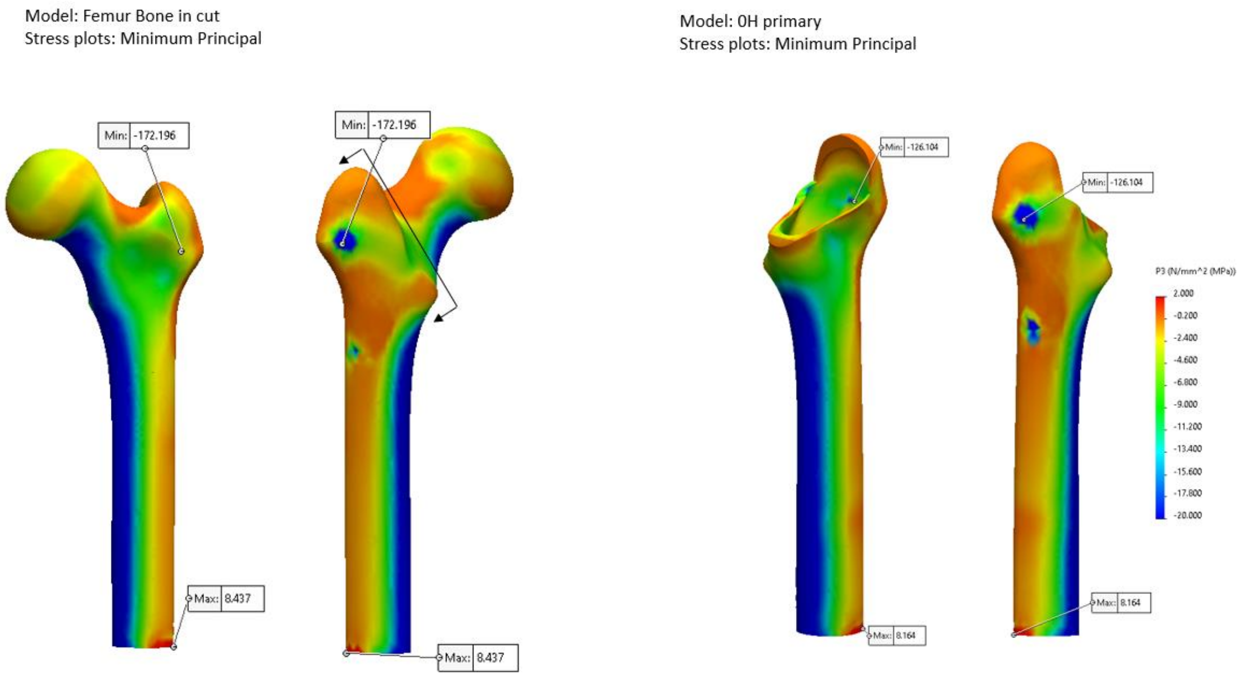

Figure 8.17- Minimum principal stresses in MPa acting in the natural femur bone model and in the cortical bone models from the 0H primary THR model with a debonded stem

Beyond the comparative studies regarding the intact femur and the implanted models, investigations were also conducted aiming to find how the type of contact configuration used in the cement-stem interfaces, the values of the new mantles' thicknesses around the stem in the revision models, and other geometric characteristics of the revision models which were used for their classification into 0H/0H or 1H/0H groups, could influence the stress distributions in the bone. An examination of the differences in the stress distributions in the cortical bone in the primary and revision models was also carried out.

Firstly, it was observed that, in all primary and revision implant models, there were some considerable alterations in the stress distribution depending on the cement-stem contact configuration. In figure 8.18, are presented the distributions of the maximum and minimum principal stresses for both cases of stem fixation of a femur model from a primary THR with a 0H stem. It is possible to observe that, above the level of the lesser trochanter, in the models with a debonded stem fixation, there is an increase in the size of the regions experiencing medium compressive stresses as well as a subtle reduction in the size of others under medium compressive stresses and a more robust increase of the regions experiencing medium tensile stresses, comparatively to what is observed in the bonded case of stem fixation. Secondly, regarding the revision THR designs, the stress distributions have shown that the influence of the variation in the mantles' thicknesses is negligible for all models, and in figure 8.19 are shown the plots of the maximum principal stresses for the debonded case of stem fixation in the 0H/0H revision models. Finally, the unique design characteristics that regard the 3D components' dimensions have been shown to exert no influence in the manner in which the stresses were distributed in the cortical bones of the revision models.

Additionally, the contours of stresses were found to be practically the same in the stress plots of the primary and revision models. In figure 8.20, are displayed the plots of the maximum principal stresses for the debonded case of stem fixation in the cortical bone from the 0H and 1H primary models that were chosen to demonstrate the similarities among stress distributions where only very small alterations, that might be a result of mesh singularities, can be noticed between the stress plots. One of them is the small concentration of compressive stresses (low maximum principal stress in the color scale) found at a small region in the 0H primary next to point P2 of muscular force application, where there is a small concentration of compressive stresses (low maximum principal stress in the color scale) that are not found in the 1H primary model. Such distribution of compressive stresses is only found in the 0H/0H revision model with a debonded cement-stem contact and with 1,6 mm of new cement thickness around the stem.

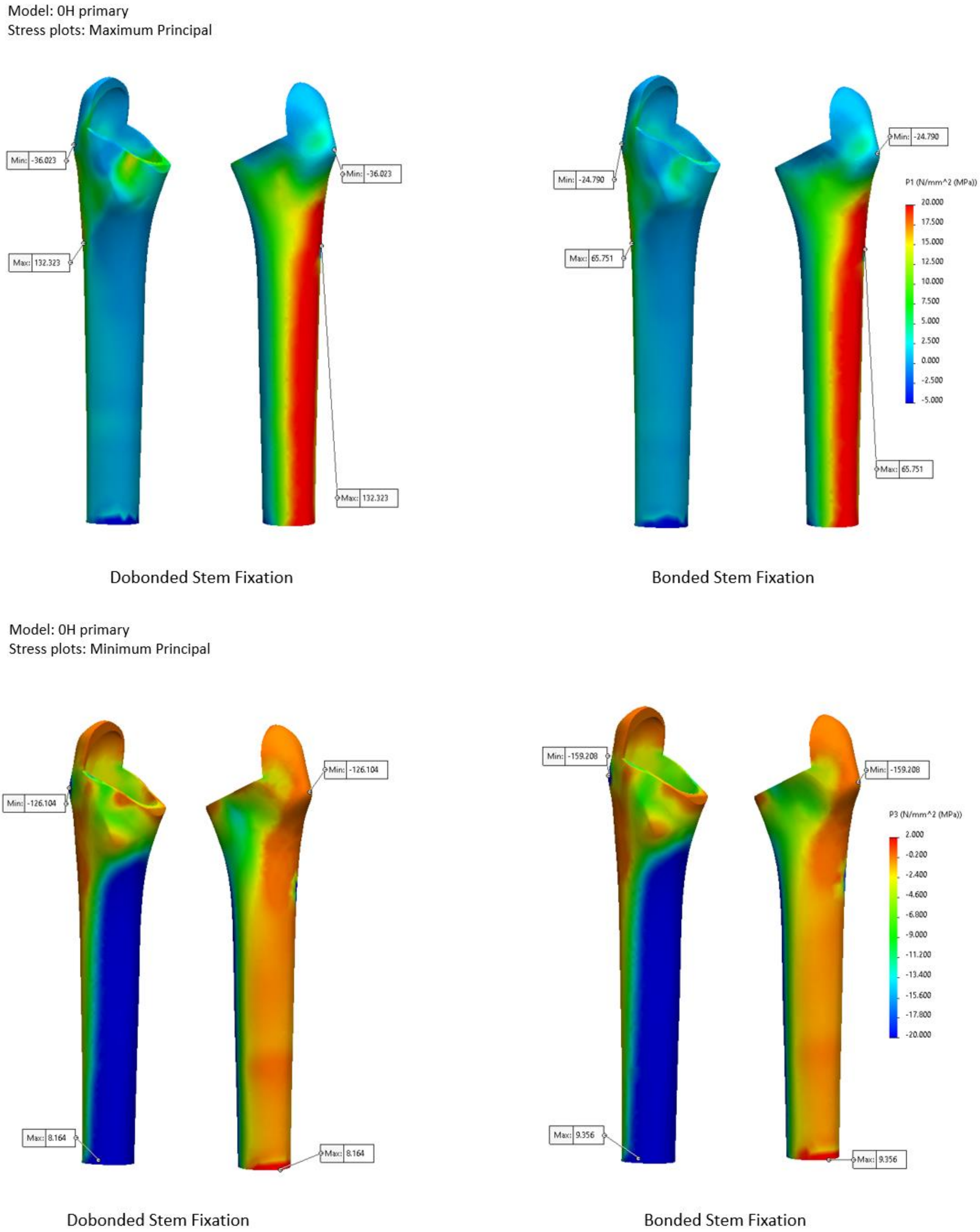

Figure 8.18 – Maximum and minimum principal stresses in MPa acting in the cortical bone from a primary THR with 0H stem for both cases of stem fixation

Model: 0H/0H revision – Debonded Stem Fixation
Stress plots: Maximum Principal

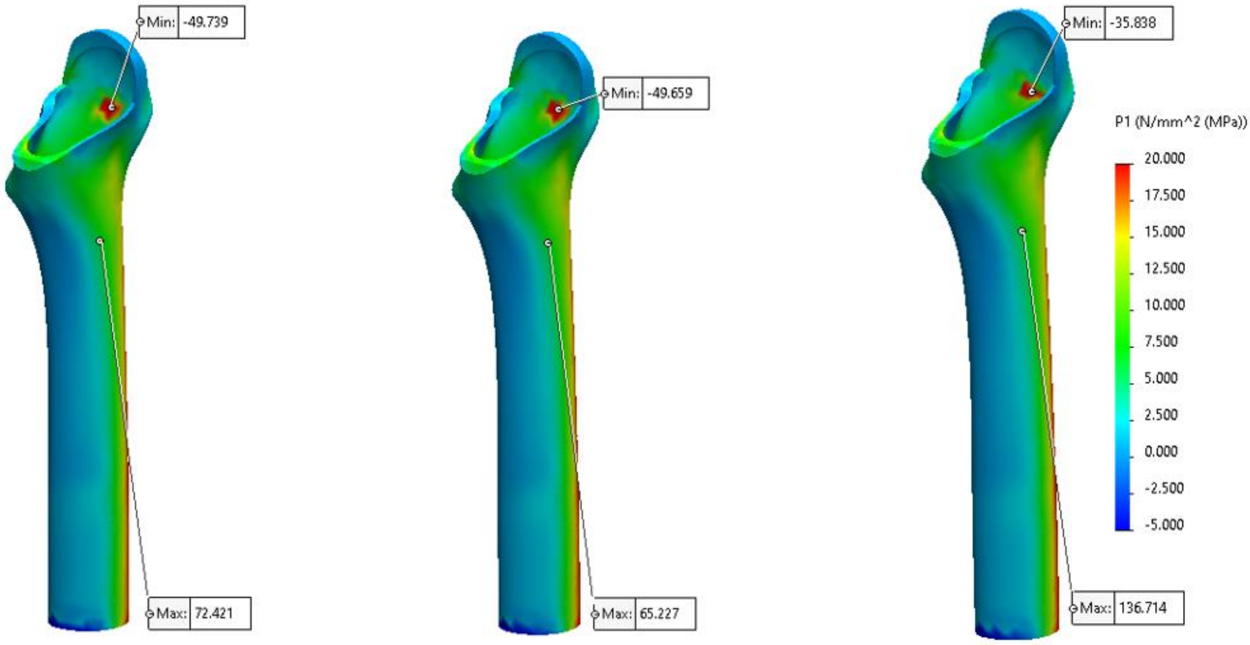

0,8 mm   1,2 mm   1,6 mm

Model: 0H/0H revision – Debonded Stem Fixation
Stress plots: Maximum Principal

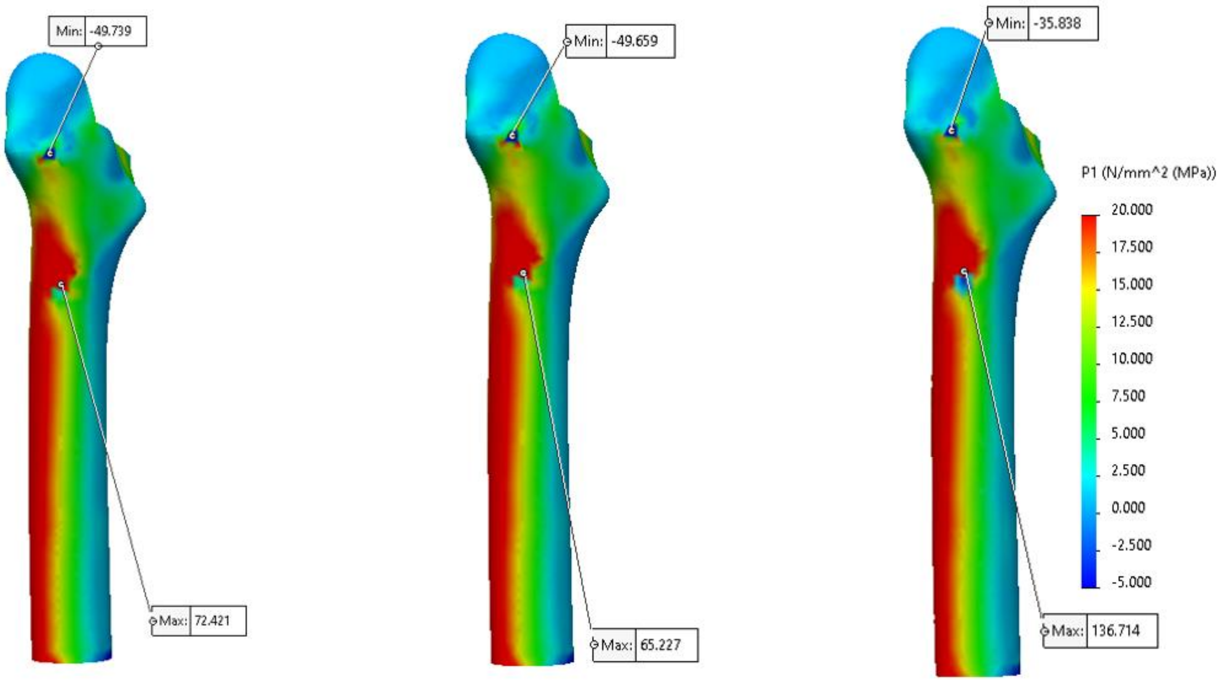

0,8 mm   1,2 mm   1,6 mm

Figure 8.19 - Maximum principal stresses in MPa for the debonded case of stem fixation in the 0H/0H revision models

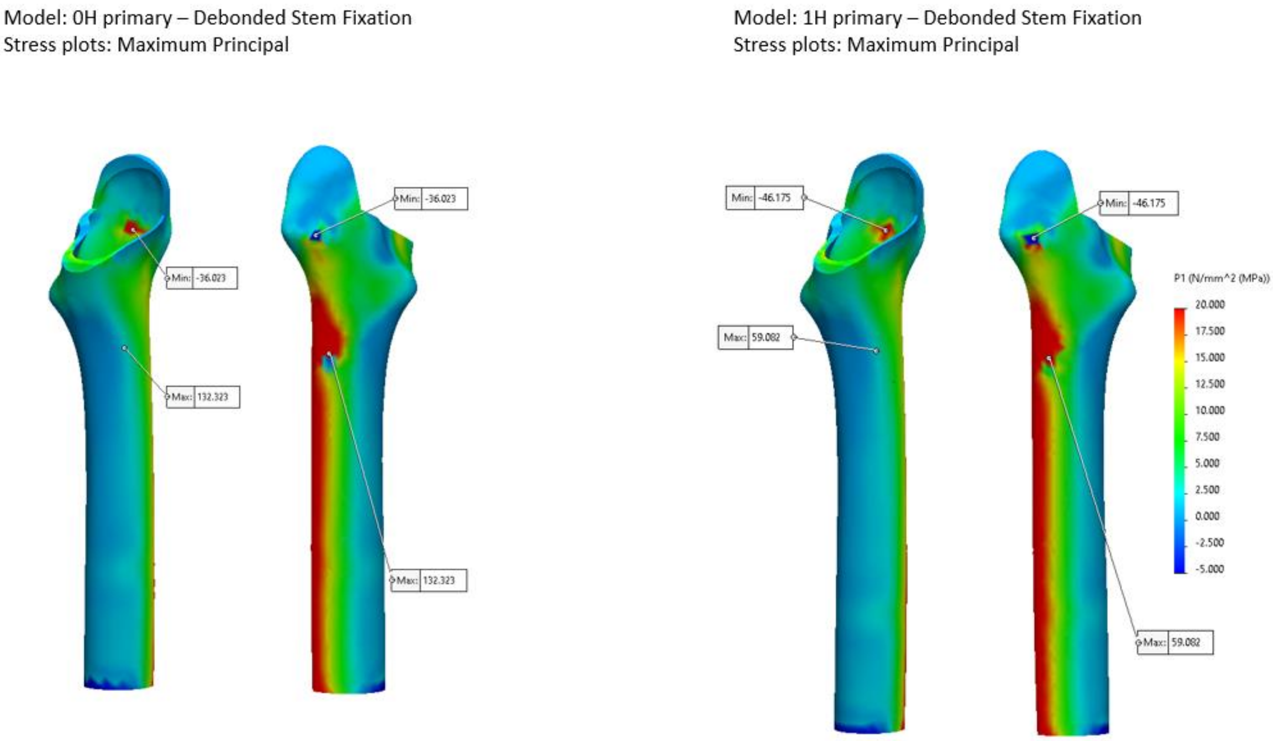

Figure 8.20 - Maximum principal stresses in MPa, for the debonded case of stem fixation, of the cortical bone in a 0H and 1H primary THR models

Chapter 9 - Probability of Failure Calculations

According to Lennon and Prendergast (2001), the finite element method is, mainly in theory, ideal for the determination of the stresses in the bone cement. Firstly, because the peak stresses determined in the simulations might result from singularities in the stress field (Lennon and Prendergast, 2001). Secondly, because localized damage failure associated with damage formation or creep can dissipate the peak stresses in the cement in vivo, which are distributed to avoid a through-mantle crack in the sites that were initially under the highest stresses (McCormack and Prendergast, 1999, cited by Lennon and Prendergast, 2001). Also, it has been proved that high cement stresses exist predominantly in the early part of the life of the replacement (Verdonschot and Huiskes, 1997, cited by Lennon and Prendergast, 2001). Therefore, a method where the study of the peak stresses wasn't a determinant factor for the analysis of the long-term stability of the in-cement THR models was employed in this work.

To examine the integrity of the implants, a statistical evaluation that involved the distribution of volumes of cement according to their probabilities of fatigue failure within a certain number of load cycles was carried out. This analysis followed the method described in Lennon and Prendergast (2001) in which the probabilities of failure (P_f) were calculated after the determination of the probabilities of survival (P_s) of a PMMA bone cement, using a polynomial equation from Murphy and Prendergast (2000) which associates the chances of survival of a fresh hand-mixed cement from Cemex Rx with the tensile stress levels exerted in an element of cement, for a life of 10 million loading cycles (see equations 1. a and 1. b). To apply such statistical analysis in the present work, new polynomial equations would have to be obtained from new fatigue tests for the fresh and old cement, and the division of volume percentages within stress ranges would have to be carried out separately for each mantle, because of the differences in loading history and mechanical properties between the well-fixed and the new cement mantles.

The probabilities of failure of the cement volumes, in the new mantles from the revision models and the mantles from the primary models, were determined by the same equation presented in Murphy and Prendergast (2000) for hand-mixed cement although more precise estimations of one cement element's life would require the execution of new fatigue tests. This formulation was selected due to the similarities, regarding the mixing technique (hand-mixing) and chemical composition, between the Hi-Fatigue cement tested in Simões et al. (2010), from which the mechanical properties were used to define the material properties of the models, with the bone cement tested in Murphy and Prendergast (2000). Both brands are PMMA based bone cements containing antibiotic and BaSo4 radiopaque additives. When applying equation 1. b, it can be verified that is only for stress levels above 3MPa, more precisely 3,062MPa, where fatigue failure of the cement is predicted to occur. Under a 4MPa stress level, the chances of failure of the cement are around 19%, and at 5 MPa this probability increases to 37%.

$$P_s = -0{,}0005\,\sigma^3 + 0{,}0202\sigma^2 - 0{,}3304\,\sigma + 1{,}8365$$

$$P_f = 1 - P_s$$

The volume percentages in the mantles from primary models were divided within principal tensile stress ranges, which are shown in figure 9.1, for the debonded and bonded cement-stem contact, where the highest amount of cement under stress levels above 3MPa are found for the debonded stem: 13,01% of volume in the model with a 0H stem and 10,65% in the one with the 1H sized stem.

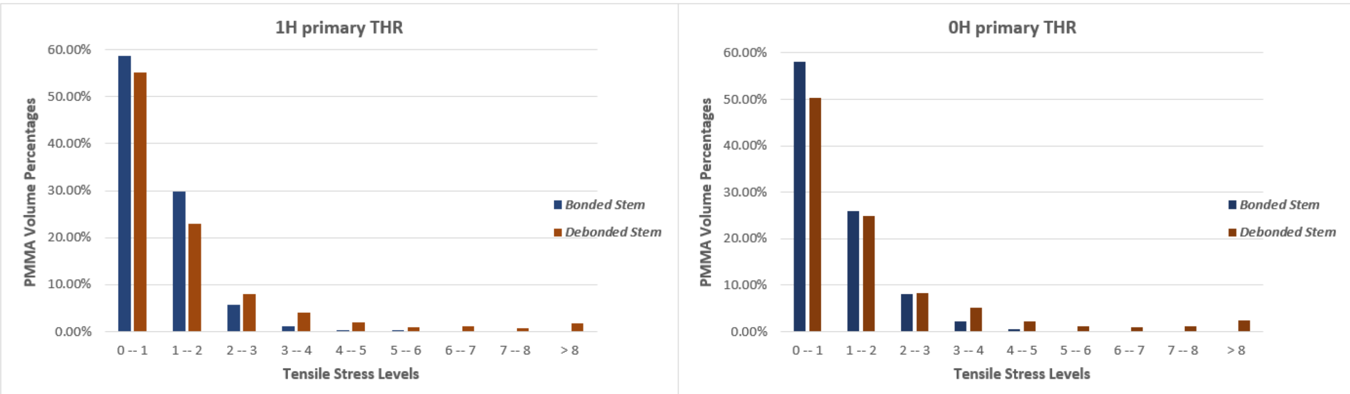

Figure 9.1 - Distribution of PMMA cement volumes of the primary THR models within a tensile stress range

Figure 9.2 displays cement volume proportions distributed within the same stress ranges, that were determined for the new mantles of the 0H/0H and 1H/0H revision models, in both cases of cement-stem fixation. It is evident that the bonded cement-stem configuration, for all revision models, results in smaller volume concentrations under stress levels above 3MPa, when compared with the debonded type of stem fixation; however, up to 3 MPa, the volume percentages were found to be more similarly distributed, except for the amount of cement under stresses between 0 MPa and 1MPa, which was higher than 45% in volume in all the models with bonded configuration, while 42,17% was the highest proportion found among the models with debonded stem, being all the other proportions inferior to 40%.

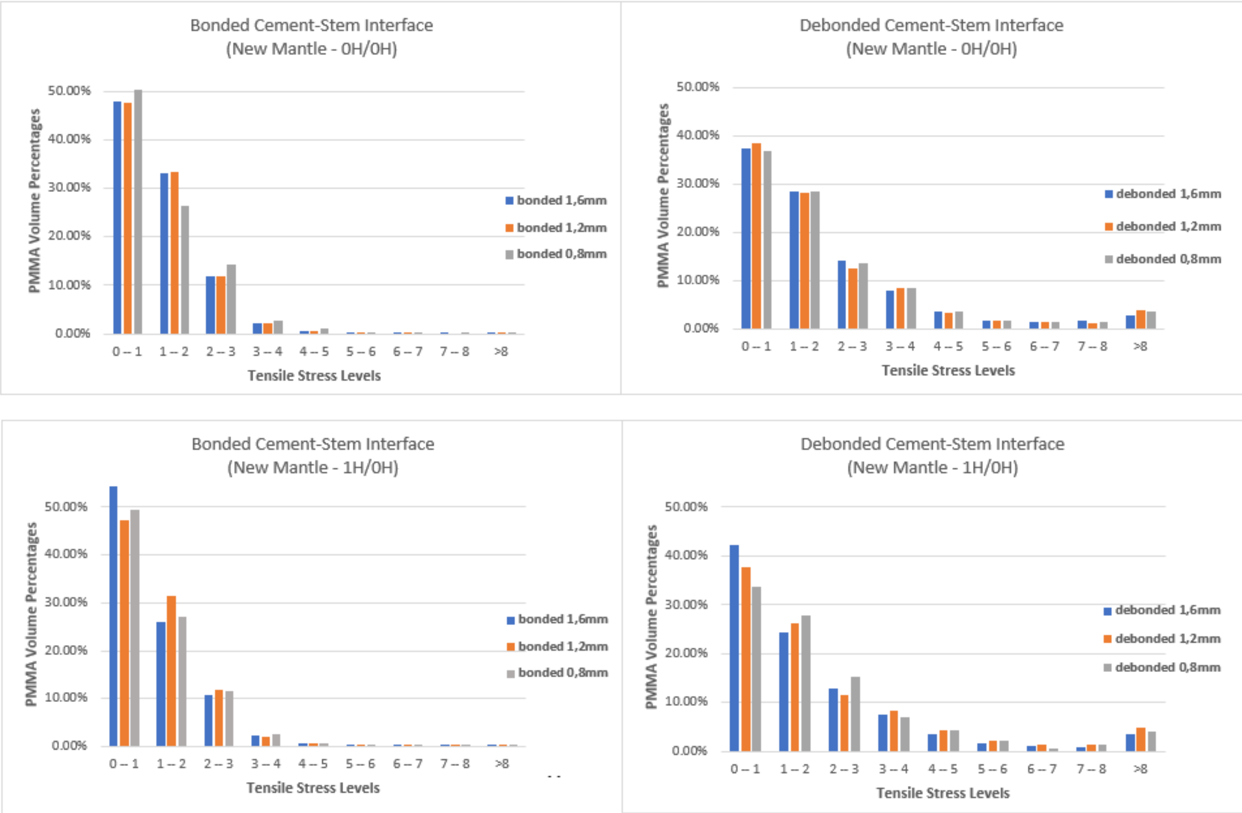

Figure 9.2 - Distribution of PMMA cement volumes of the new mantles from the revision THR models within a tensile stress range

In the 0H/0H revision models, the highest volume percentages above 3 MPa in the new cement mantles are present for the debonded stem configuration, where 19,99% of the volume was found for the model with new mantle thickness around the stem of 0,8 mm, while 22,34% of the cement volume is stressed above 3MPa for the 1H/0H model with debonded cement-stem interface and new mantle thickness of 1,2 mm. Regarding percentages of new cement under stresses above 5 MPa, both of which would have higher chances of fatigue failure, the highest values were also found in models with debonded cement-stem interface configuration, where the 0H/0H model with new mantle thickness of 1,2 mm had a volume percentage of 8,19%, and the 1H/0H model with new mantle thickness of 1,2 mm had a volume percentage of 9,76%.

Because of the small variation in the volumes of the mantles in the models from the 0H/0H and 1H/0H groups, the calculated volume percentage distributions could be used as a parameter of comparison of the results related to the probability of failure distributions within the cement. A direct comparison between the results found for the new mantles and the cement from primary models could not be employed, due to the more expressive differences in their total volumes; the highest calculated volume for a new mantle in a revision model was equal to 11908,68 mm³, while the smallest volume of cement in a primary model is equal to 23741,46 mm³. Within each revision group, the proportions of volume above 3MPa have indicated that the influence of the new mantle thickness values in the total volumes of new cement that might fail under 10 million cycles is not very significant. For the same type of cement-stem configuration and revision model group, the higher deviation in this result has not reached two percentage points, and no linearity was verified in the way results varied the thicknesses values. Moreover, while comparing the percentages between the revision model groups, it wasn’t possible to verify linear alterations in the results considering the same type of stem fixation and mantle thickness. Table 9.1 displays the volume percentages under stresses above 3MPa, for the new mantles in all the model configurations used for the static studies.

Table 9.1 – New mantle cement volume percentages under stress levels above 3MPa (%V > 3MPa)

New Mantles – 0H/0H designs		
Thickness (mm)	(%V > 3MPa)	
	Bonded Case	Debonded Case
1,6	3,47	18,84
1,2	3,45	19,68
0,8	4,7	19,99
New Mantles – 1H/0H designs		
Thickness (mm)	(%V > 3MPa)	
	Bonded Case	Debonded Case
1,6	3,84	18,53
1,2	3,24	19,34
0,8	4,15	19,94

The mechanical properties defined in the 3D models of the well-fixed mantles were configured to reflect the effects of aging and of the loading cycles that acted on the cement until the revision surgery. Therefore, the probability of failure calculations would be more aligned with the biomechanical response of the old mantle, if they were made using regression curves obtained from data of fatigue tests from well-fixed mantle samples. Consequently, the formulation from Murphy and Prendergast (2000) hasn't been directly applied in this work to estimate the long-term life of the older mantle. However, as can be observed in figure 9.3, the old cement volumes under tensile stress levels superior to 3MPa are insignificant in all revision models, even in the studied cases of debonded stem fixation. The highest volume percentage stressed above this value was considerably small for all configurations of the revision models (the highest percentage was 0,97% of volume, for the debonded cement-stem configuration in the 1H/0H revision model with the new cement layer thickness of 0,8 mm). Thus, if new fatigue tests result in a polynomial equation that presents a similar correspondence between the stress levels and the chances of failure as the one found by equation 1. b, mantle cracking would very unlikely be initiated in the well-fixed cement under the loading conditions studied in this work.

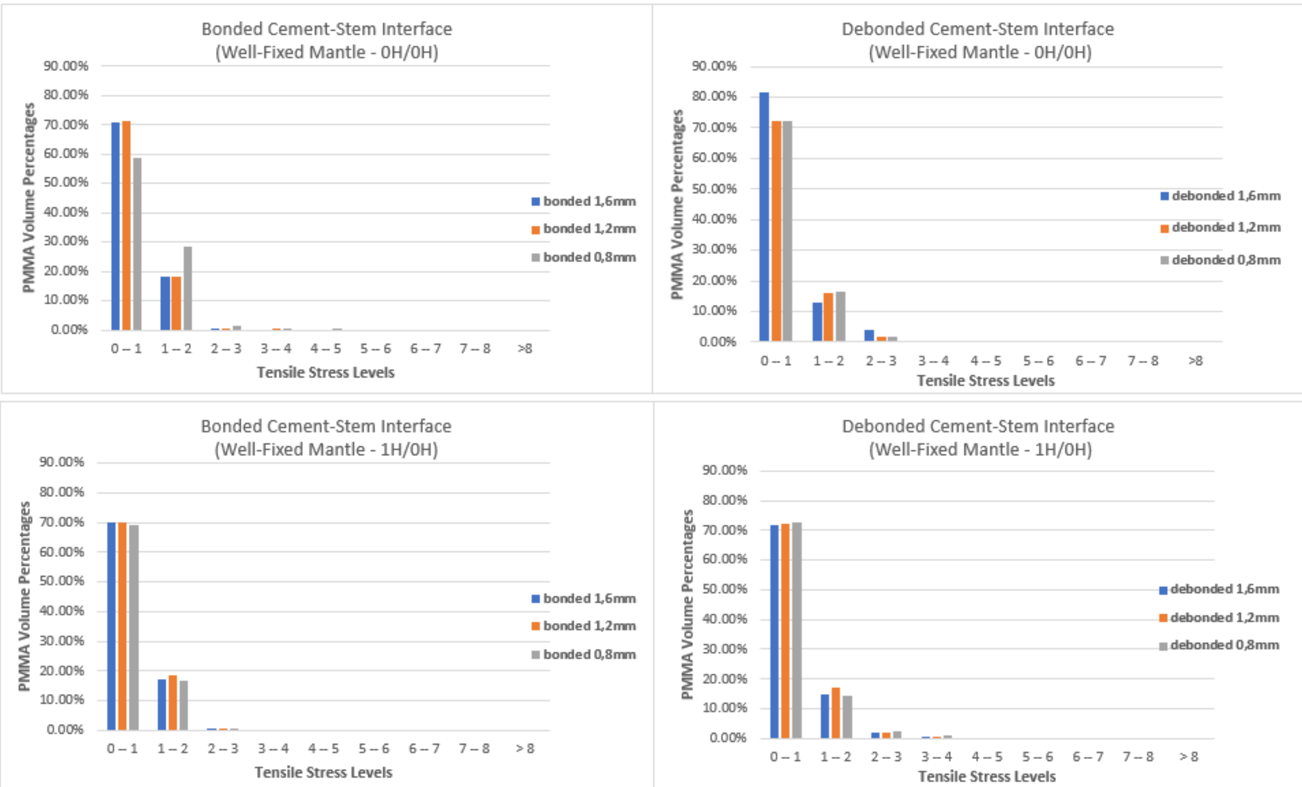

Figure 9.3 - Distribution of PMMA cement volumes of the well-fixed mantles from the revision THR models within a tensile stress range

CONCLUSIONS

Finite element analyses were conducted for the simulation of a static loading condition in models of femoral components of revision total hip replacement surgeries, with the main objective to study the distributions of the principal stresses exerted in the implant elements of the in-cement revision THR models, as well as to use those stress plots as a basis for the estimation of the long-term stability of these structures, by observing the tendency for the occurrence of stress shielding in the proximal femur models, and quantifying of the amounts of cement where fatigue failure would be initiated. Although the present investigation was directed to the study of in-cement revision models, those analyses were extended to the primary THR models created for this work. Moreover, for the revision models, an evaluation of the influence of the new cement thickness and the reduction of the revision of the stem by one with reduced body size was also investigated. A total of eight models were created (two of primary and six of revision surgeries) to simulate the load transmission onto the implant components by the muscular and hip contact action, at a moment when the load transmitted would have reached its maximum value. Each model was configured to recreate a case of stem fixation when micromovement within the cement would occur, and when the stem subsidence would have completely stopped. Furthermore, as described in chapter 6, all models were built with simplifications in the modeling of the type of contacts in the implants' interfaces, in the materials characterization, and in the type of load case, which disregarded any loading conditions other than walking. However, those simplifications did not compromise the purposes of the present work to employ analyses based on comparisons of simulations' outcomes obtained for the revision and primary THR models.

Analyzing the contour of stresses in the PMMA mantles, it was observed that the distributions of the maximum and minimum principal components are more dependent on the type of stem fixation within the cement than on any of the other geometrical characteristics analyzed in the static studies. For all models, primary or revision, the debonded stem resulted in the increase of the tensile and compressive stress levels across the implant components. Among the primary models, the stem type (0H or 1H) and the geometry of the mantle have not contributed to major modifications between the mantles' stress plots. For the revision models, the contour of stresses was found to not get expressively affected when the new mantle thickness around the stem was the only altered parameter. Likewise, the differences in the stress distributions, in the cement mantles from revision THR designs, were found to be minimal between the models with the same characteristics related to stem fixation and mantle thickness, but belonging to different revision model groups (0H/0H and 1H/0H), what indicates that to replace the femoral stem by another with the same dimensions or by one with shorter length does not hold great influence in the load transfer mechanisms between the mantles' interfaces. Regarding the contour of stresses in the metallic prosthetic components, the first major contributor for alterations in those results was the stem's design, followed by the type of stem fixation. The 0H sized stems have exhibited practically the same stress distributions between the primary and revision models with the same cement-stem contact configuration.

The clinical complications which result from stress shielding were one of the considered aspects used to evaluate how much the long-term stability of the femoral implants can be compromised, depending on their designs and type of cement-stem contact. As an attempt to observe how the design configurations could exert influence in this phenomenon, comparisons between the stress plots of the natural femur model with the ones from revision and primary THR models were carried out. The only characteristic found to exert some influence in the stress distributions of the THR models was the type of stem fixation. Comparatively with the natural femur model, there were observed alterations in the stress distributions that can be associated with the causes of stress shielding. In all cortical bones from the surgery models, above the level of the lesser trochanter, the regions under medium tensile stresses have increased, and that the highest compressive stresses have been replaced by stresses of medium moduli. However, among the THR models, when compared with the bonded case of fixation, the debonded stems resulted in fairly bigger regions under the medium tensile stresses and inexpressive reductions in the regions under medium compressive stresses. Therefore, despite the femoral stress distributions having been obtained from static studies that only accounted for a moment during walking, it was possible to conclude that the proximal regions of the cortical bone would experience minimized stress shielding if the force-closed stem still subsides within the cement.

Fatigue failure of the PMMA cement was another parameter used in the estimation of the long-term stability of all the implants. As for the contours of stresses, the found distributions of cement volumes within tensile stress levels have indicated that the variation in the type of stem fixation is the only parameter to exert expressive influence in the distribution of the chances of failure, across the mantles from both primary and revision models, where the debonded cement-stem configuration resulted in much higher proportions of cement with chances of failure within 10 years. Taking into consideration that, in most of the cases, the debonded type of stem contact can only be observed in the first two years after surgery, when the stem still subsides within the cement, the higher risks of failure would only exist in the first 20% of the period considered in the present analysis. The bonded cement-stem interface fixation corresponds to the post-operative period when subsidence does not occur anymore, and the highest proportion of cement under stress levels above 3MPa which was determined for the bonded contact was 4,7% of the new cement from one of the revision models. These numerical outcomes might provide one biomechanical explanation for the high survival rates of femoral components after revision surgeries that employ the in-cement technique, as pointed out in Cnudde et al. (2017).

Regarding the revision models, when only the type of revision group (1H/0H and 0H/0H) or the new mantle thickness were the altered parameters, the variations in the proportions of new cement under the risk of fatigue failure were negligible. These results indicate that the replacement of the femoral stem by a new one with small dimensions or by one with the same size results in no alterations in the long-term stability associated with fatigue failure. Furthermore, it can be assumed that the calculated chances of failure for the PMMA mantles are very unlikely to suffer significant variations if the new mantle thickness is kept between the minimum and maximum values used in this work, 0,8 mm and 1,6 mm respectively. Moreover, based on the very small proportions of old cement under stresses above 3MPa, it can be concluded that the well-fixed mantles are stabler structures than the new mantles. This higher stability might be explained by the bigger area of contact between the new and old cement when compared with the total area of the cement-stem interface.

FUTURE WORKS

The present work's designs of revision THR models can be used in future works that could provide different contributions regarding the analysis of other biomechanical scenarios and/or model configurations that include:

- The evaluation of different load cases that correspond to different daily activities, such as an instance during stair climbing, as the loading profile provided in Heller et al. (2005);
- The effects of the presence of the distal centralizer and cement restrictor in the stress distributions;
- The influence of design and stem fixation in the load-transfer mechanisms which occur in the in-cement implants and was not investigated in this work because it hasn't had a direct correlation with the conducted long-term stability analyses. Tensile hoop and radial compressive stress plots can be obtained from this work's THR models and studied in deeper detail to provide a better comprehension of these transference mechanisms and how they vary within the design characteristics and interface configurations;
- The calculation of the relative micromovement at the implants' interfaces where the debonding and slipping between them would be determined as in prior works such as Ramaniraka et al. (2000);
- The development of a series of analyses where this work's finite element models that could be used in the evaluation of the progression of interface separation, using a fracture mechanics approach, such as the one presented in Hung and Chang (2010), where the interfacial properties are experimentally measured and posteriorly configured in the models.

REFERENCES

Ait Moussa, A., Fischer, J., Yadav, R., & Khandaker, M. (2017). Minimizing Stress Shielding and Cement Damage in Cemented Femoral Component of a Hip Prosthesis through Computational Design Optimization. Advances in orthopedics, 2017, 8437956. https://doi.org/10.1155/2017/8437956

Barrack, R. L., Mulroy, R. D., Jr, & Harris, W. H. (1992). Improved cementing techniques and femoral component loosening in young patients with hip arthroplasty. A 12-year radiographic review. The Journal of bone and joint surgery. British volume, 74(3), 385–389. https://doi.org/10.1302/0301-620X.74B3.1587883

Bergmann, G., Graichen, F., & Rohlmann, A. (1993). Hip joint loading during walking and running, measured in two patients. Journal of biomechanics, 26(8), 969–990. https://doi.org/10.1016/0021-9290(93)90058-m

Bizot, P., Nizard, R., Hamadouche, M., Hannouche, D., & Sedel, L. (2001). Prevention of wear and osteolysis: alumina-on-alumina bearing. Clinical orthopaedics and related research, (393), 85–93. https://doi.org/10.1097/00003086-200112000-00010

Buechel, F. F., & Pappas, M. J. (2015). Principles of Human Joint Replacement. Springer. 10.1007/978-3-319-15311-7

Callaghan, J. J., Albright, J. C., Goetz, D. D., Olejniczak, J. P., & Johnston, R. C. (2000). Charnley total hip arthroplasty with cement. Minimum twenty-five-year follow-up. The Journal of bone and joint surgery. American volume, 82(4), 487–497. https://doi.org/10.2106/00004623-200004000-00004

Cassar-Gheiti, A. J., McColgan, R., Kelly, M., Cassar-Gheiti, T. M., Kenny, P., & Murphy, C. G. (2020). Current concepts and outcomes in cemented femoral stem design and cementation techniques: the argument for a new classification system. EFORT open reviews, 5(4), 241–252. https://doi.org/10.1302/2058-5241.5.190034

Cnudde, P. H., Kärrholm, J., Rolfson, O., Timperley, A. J., & Mohaddes, M. (2017). Cement-in-cement revision of the femoral stem: analysis of 1179 first-time revisions in the Swedish Hip Arthroplasty Register. The bone & joint journal., 99-B(4 Supple B), 27–32. https://doi.org/10.1302/0301-620X.99B4.BJJ-2016-1222.R1

CHARNLEY J. (1960). Anchorage of the femoral head prosthesis to the shaft of the femur. The Journal of bone and joint surgery. British volume, 42-B, 28–30. https://doi.org/10.1302/0301-620X.42B1.28

Crowninshield RD, Brand RA, Johnston RC, Pedersen DR. The Otto Aufranc Award Paper. An analysis of femoral prosthesis design: the effects on proximal femur loading. Hip. 1981:111-22. PMID: 7333883.

Della Valle, A. G., Zoppi, A., Peterson, M. G., & Salvati, E. A. (2005). A rough surface finish adversely affects the survivorship of a cemented femoral stem. Clinical orthopaedics and related research, (436), 158–163. https://doi.org/10.1097/00003086-200507000-00024

Duda, G. N., Heller, M., Albinger, J., Schulz, O., Schneider, E., & Claes, L. (1998). Influence of muscle forces on femoral strain distribution. Journal of biomechanics, 31(9), 841–846. https://doi.org/10.1016/s0021-9290(98)00080-3

Duncan, W. W., Hubble, M. J., Howell, J. R., Whitehouse, S. L., Timperley, A. J., & Gie, G. A. (2009). Revision of the cemented femoral stem using a cement-in-cement technique: a five- to 15-year review. The Journal of bone and joint surgery. British volume, 91(5), 577–582. https://doi.org/10.1302/0301-620X.91B5.21621

Ebramzadeh, E., Sarmiento, A., McKellop, H. A., Llinas, A., & Gogan, W. (1994). The cement mantle in total hip arthroplasty. Analysis of long-term radiographic results. The Journal of bone and joint surgery. American volume, 76(1), 77–87. https://doi.org/10.2106/00004623-199401000-00010

Foran, J. R. H., & Fischer, S. J. (2020, 6 2). Total Hip Replacement. OrthoInfo. https://orthoinfo.aaos.org/en/treatment/total-hip-replacement/

Galia, C. R., Diesel, C. V., Guimarães, M. R., & Ribeiro, T. A. (2017). Total hip arthroplasty: a still evolving technique. Revista brasileira de ortopedia, 52(5), 521–527. https://doi.org/10.1016/j.rboe.2016.09.011

Gross, S., & Abel, E. W. (2001). A finite element analysis of hollow stemmed hip prostheses as a means of reducing stress shielding of the femur. Journal of biomechanics, 34(8), 995–1003. https://doi.org/10.1016/s0021-9290(01)00072-0

Heller, M. O., Bergmann, G., Kassi, J. P., Claes, L., Haas, N. P., & Duda, G. N. (2005). Determination of muscle loading at the hip joint for use in pre-clinical testing. Journal of biomechanics, 38(5), 1155–1163. https://doi.org/10.1016/j.jbiomech.2004.05.022

Hip-Joint and abductor-muscle forces adequately represent in vivo loading of a cemented total hip reconstruction (J. Still, N. Versions hot, 2000)

Huiskes R. (1990). The various stress patterns of press-fit, ingrown, and cemented femoral stems. Clinical orthopaedics and related research, (261), 27–38.

Hung, J., & Chang, F. (2010). Computational modeling of debonding behavior at the bone/cement interface with experimental validation. Materials Science and Engineering: C, 30, 445-453.

Hutt, J., Hazlerigg, A., Aneel, A., Epie, G., Dabis, H., Twyman, R., & Cobb, A. (2014). The effect of a collar and surface finish on cemented femoral stems: a prospective randomised trial of four stem designs. International orthopaedics, 38(6), 1131–1137. https://doi.org/10.1007/s00264-013-2256-z

K., & Wolfram, U. (2016). Mechanical properties of cortical bone and their relationships with age, gender, composition and microindentation properties in the elderly. Bone, 93, 196–211. https://doi.org/10.1016/j.bone.2015.11.018

Keppler, MD, L., & McTighe, Dr. H.S. (hc), T. (2012). The Role of Stem Modularity for THA in a Community Based Practice. Reconstructive Review, 2(1). https://doi.org/10.15438/rr.v2i2.10

Kiss J , Murray DW , Turner-Smith AR , Bithell J , Bulstrode CJ . Migration of cemented femoral components after THR: roentgen stereophotogrammetric analysis. J Bone Joint Surg Br 1996;78:796–801

Knight, S. R., Aujla, R., & Biswas, S. P. (2011). Total Hip Arthroplasty - over 100 years of operative history. Orthopedic reviews, 3(2), e16. https://doi.org/10.4081/or.2011.e16

Kumar, A., Porter, M., Shah, N., Gaba, C., & Siney, P. (2019). Outcomes of Cement in Cement Revision, in Revision Total Hip Arthroplasty. Open access Macedonian journal of medical sciences, 7(23), 4059–4065. https://doi.org/10.3889/oamjms.2019.710

Kwong K. S. (1990). The biomechanical role of the collar of the femoral component of a hip replacement. The Journal of bone and joint surgery. British volume, 72(4), 664–665. https://doi.org/10.1302/0301-620X.72B4.2380224

Lennon, A.B.; Prendergast, P.J. Evaluation of cement stresses in finite element analyses of cemented orthopaedic implants. J. Biomech. Eng. 2001, 123, 623–628.

Lee A.J.C. (2000) The Time-dependent Properties of Polymethylmethacrylate Bone Cement: the Interaction of Shape of Femoral Stems, Surface Finish and Bone Cement. In: Learmonth I.D. (eds) Interfaces in Total Hip Arthroplasty. Springer, London. https://doi.org/10.1007/978-1-4471-0477-3_2

Markolf KL, Amstutz HC, Hirschowitz DL. The effect of calcar contact on femoral component micromovement. A mechanical study. J Bone Joint Surg Am. 1980 Dec;62(8):1315-23. PMID: 7440610.

McCaskie, A. (2000). Mechanical Analysis of the Interface.

McCormack, B. A., & Prendergast, P. J. (1999). Microdamage accumulation in the cement layer of hip replacements under flexural loading. Journal of biomechanics, 32(5), 467–475. https://doi.org/10.1016/s0021-9290(99)00018-4

Merola, M., & Affatato, S. (2019). Materials for Hip Prostheses: A Review of Wear and Loading Considerations. Materials (Basel, Switzerland), 12(3), 495. https://doi.org/10.3390/ma12030495

Mirzaali, M. J., Schwiedrzik, J. J., Thaiwichai, S., Best, J. P., Michler, J., Zysset, P. K., & Wolfram, U. (2016). Mechanical properties of cortical bone and their relationships with age, gender, composition and microindentation properties in the elderly. Bone, 93, 196–211. https://doi.org/10.1016/j.bone.2015.11.018

Mohler, C. G., Callaghan, J. J., Collis, D. K., & Johnston, R. C. (1995). Early loosening of the femoral component at the cement-prosthesis interface after total hip replacement. The Journal of bone and joint surgery. American volume, 77(9), 1315–1322. https://doi.org/10.2106/00004623-199509000-00004

Morgan, E. F., Unnikrisnan, G. U., & Hussein, A. I. (2018). Bone Mechanical Properties in Healthy and Diseased States. Annual review of biomedical engineering, 20, 119–143. https://doi.org/10.1146/annurev-bioeng-062117-121139

Murphy, B., & Prendergast, P.J. (2000). On the magnitude and variability of the fatigue strength of acrylic bone cement. International Journal of Fatigue, 22, 855-864.

Nieuwenhuijse MJ , Valstar ER , Kaptein BL , Nelissen RG . The Exeter femoral stem continues to migrate during its first decade after implantation: 10-12 years of follow-up with radiostereometric analysis (RSA). Acta Orthop 2012;83:129–134.

Nuño N, Groppetti R, Senin N. Static coefficient of friction between stainless steel and PMMA used in cemented hip and knee implants. Clin Biomech (Bristol, Avon). 2006 Nov;21(9):956-62. doi: 10.1016/j.clinbiomech.2006.05.008. Epub 2006 Jul 24. PMID: 16860449.

Ocran, E., & Salvador, F. (2021). Hip joint. kenhub. https://www.kenhub.com/en/library/anatomy/hip-joint

Ataollahi Oshkour, A., Oshkour, A. A., Talebi, H., Shirazi, S. F. S., Bayat, M., Yau, Y. H., … Osman, N. A. A. (2014). Comparison of Various Functionally Graded Femoral Prostheses by Finite Element Analysis. The Scientific World Journal, 2014, 1–17. https://doi.org/10.1155/2014/807621

Quinlan, J. F., O'Shea, K., Doyle, F., & Brady, O. H. (2006). In-cement technique for revision hip arthroplasty. The Journal of bone and joint surgery. British volume, 88(6), 730–733. https://doi.org/10.1302/0301-620X.88B6.17037

Ramaniraka, N. A., Rakotomanana, L. R., & Leyvraz, P. F. (2000). The fixation of the cemented femoral component. Effects of stem stiffness, cement thickness and roughness of the cement-bone surface. The Journal of bone and joint surgery. British volume, 82(2), 297–303.

Reilly, D. T., & Burstein, A. H. (1975). The elastic and ultimate properties of compact bone tissue. Journal of biomechanics, 8(6), 393–405. https://doi.org/10.1016/0021-9290(75)90075-5

Revision Total Hip Replacement Orthoinfo - Academy of Orthopaedic Surgeons

Rice, J., Prenderville, T., Murray, P., McCormack, B., & Quinlan, W. (1998). Femoral cementing techniques in total hip replacement. International orthopaedics, 22(5), 308–311. https://doi.org/10.1007/s002640050266

Sandhu, H. S., & Middleton, R. G. (2005). Controversial topics in orthopaedics: ceramic-on-ceramic. Annals of the Royal College of Surgeons of England, 87(6), 415–416.

Sandiford, N. A., Jameson, S. S., Wilson, M. J., Hubble, M. J., Timperley, A. J., & Howell, J. R. (2017). Cement-in-cement femoral component revision in the multiply revised total hip arthroplasty: results with a minimum follow-up of five years. The bone & joint journal., 99-B(2), 199–203. https://doi.org/10.1302/0301-620X.99B2.BJJ-2016-0076.R1

SAWBONES®. (n.d.). Retrieved 08 15, 2020, from https://www.sawbones.com/

F. Simões, L. Roseiro, and P. Carvalhais, “Total Hip Joint Revision – a Comparision between the Mechanical Properties of Older and Fresh Cement,” ECCM 2010 – IV European Conference on Computational Mechanics, Paris 16, May 21, 2010.

Smith and Nephew. (n.d.). CPCS Surgical Technique. Smith and Nephew. https://www.smith-nephew.com/professional/products/all-products/cpcs/

Smith D. C. (2005). The genesis and evolution of acrylic bone cement. The Orthopedic clinics of North America, 36(1), 1–10. https://doi.org/10.1016/j.ocl.2004.06.012

stryker®. (2018). Exeter V40 Surgical technique - EXETER-SP-6. stryker. https://www.stryker.com/us/en/joint-replacement/products/exeter.html

SULZER MEDICA. (n.d.). MS-30 TM Surgical Technique. RPA - Registo Português de Artroplastias. http://www.rpa.spot.pt/getdoc/da874da5-f640-40b9-8019-ffafce883b0f/MS_30.aspx

Vaishya, R., Chauhan, M., & Vaish, A. (2013). Bone cement. Journal of clinical orthopaedics and trauma, 4(4), 157–163. https://doi.org/10.1016/j.jcot.2013.11.005

Verdonschot, N., & Huiskes, R. (1996). Mechanical effects of stem cement interface characteristics in total hip replacement. Clinical orthopaedics and related research, (329), 326–336. https://doi.org/10.1097/00003086-199608000-00040

von Schewelov T , Carlsson A , Sanzén L , Besjakov J . Continuous distal migration and internal rotation of the C-stem prosthesis without any adverse clinical effects:

an RSA study of 33 primary total hip arthroplasties followed for up to ten years. Bone Joint J 2014;96-B:604–608

Webb, J. C., & Spencer, R. F. (2007). The role of polymethylmethacrylate bone cement in modern orthopaedic surgery. The Journal of bone and joint surgery. British volume, 89(7), 851–857. https://doi.org/10.1302/0301-620X.89B7.19148

Appendices

Appendix A - Prostheses Design

The two metallic prostheses included in this work's finite element models which were designated as 0H and 1H following a designation system found in the the Smith and Nephew®'s manual indicated in this work's references. In this manufacture's manual H is an indication that both prostheses have high neck offsets and, therefore, smaller stem neck angles. The size 0 corresponds to a stem length of 120 mm while the size 1 corresponds to a 135 mm stem length. Along with the increase in the lengths, there is also a proportional augment in the other linear dimensions

For this work, only the stem lengths are the same as those found in the Smith and Nephew®'s manual, all other dimensions are different and were defined to attend to the design requirements of alignment.

In the figure below, are shown the main dimensions in the medio-lateral plane for the 1H stem implanted in a primary THR model and a 0H stem implanted in a 1H/0H revision model.

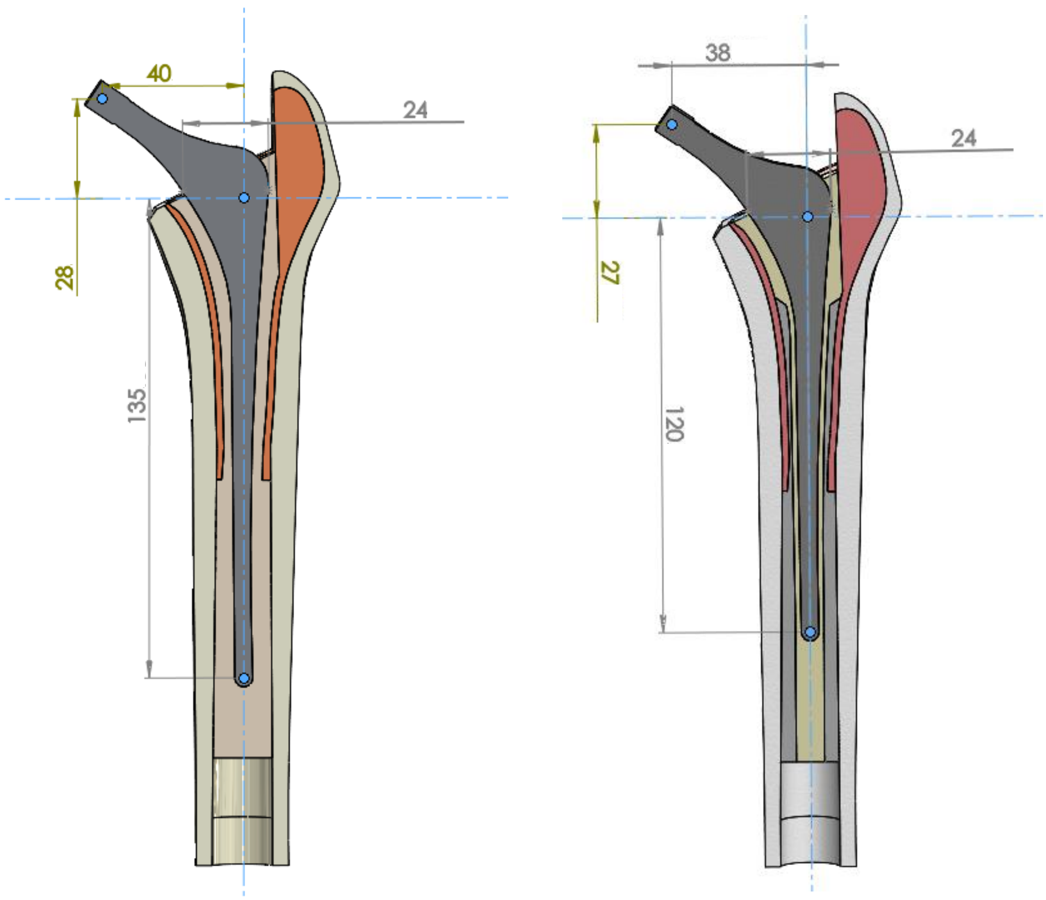

In the following table are indicated the main dimensions of the 0H and 1H stems, in millimeters. As mentioned in chapter 6, those dimensions were: the stem length, the antero-posterior width (A-P width), medio-lateral width (M-L width), the neck height, and the neck offset.

Size	Stem Length	A-P width	M-L width	Neck Height	Neck Offset
0H	125	9	24	27	38
1H	135	10	24	28	40

Appendix B - Mesh Convergence Analysis

The following tables give the final configurations of the meshes from the finite element models evaluated in this work, which were defined after the mesh convergence analyses, where the total number of elements and the minimum and maximum element size are displayed.

Debonded Cement-Stem Configuration			
Models	N° Of Elements	Minimum Element Size (mm)	Maximum Element Size (mm)
0H	62097	1,02	5,1
0H/0H (0,8 mm)	70608	0,92	4,6
0H/0H (1,2 mm)	70448	0,92	4,6
0H/0H (1,6 mm)	70726	1,02	5,1
1H	64339	1,02	5,1
1H/0H (0,8 mm)	71716	0,94	4,7
1H/0H (1,2 mm)	69813	0,92	4,6
1H/0H (1,6 mm)	67579	0,96	4,8

Bonded Cement-Stem Configuration			
Models	N° Of Elements	Minimum Element Size (mm)	Maximum Element Size (mm)
0H	57568	1,2	6
0H/0H (0,8 mm)	71211	0,90	4,5
0H/0H (1,2 mm)	72230	0,86	4,3
0H/0H (1,6 mm)	71454	0,88	4,4
1H	61744	1,2	6
1H/0H (0,8 mm)	72603	0,82	4,1
1H/0H (1,2 mm)	73030	0,86	4,3
1H/0H (1,6 mm)	73867	0,82	4,1